INFORMATION TO USERS

This manuscript has been reproduced from the microfilm master. UMI films the text directly from the original or copy submitted. Thus, some thesis and dissertation copies are in typewriter face, while others may be from any type of computer printer.

The quality of this reproduction is dependent upon the quality of the copy submitted. Broken or indistinct print, colored or poor quality illustrations and photographs, print bleedthrough, substandard margins, and improper alignment can adversely affect reproduction.

In the unlikely event that the author did not send UMI a complete manuscript and there are missing pages, these will be noted. Also, if unauthorized copyright material had to be removed, a note will indicate the deletion.

Oversize materials (e.g., maps, drawings, charts) are reproduced by sectioning the original, beginning at the upper left-hand corner and continuing from left to right in equal sections with small overlaps. Each original is also photographed in one exposure and is included in reduced form at the back of the book.

Photographs included in the original manuscript have been reproduced xerographically in this copy. Higher quality 6" x 9" black and white photographic prints are available for any photographs or illustrations appearing in this copy for an additional charge. Contact UMI directly to order.

UMI

A Bell & Howell Information Company
300 North Zeeb Road, Ann Arbor MI 48106-1346 USA
313/761-4700 800/521-0600

REMOTE SENSING OF LAND SURFACE CONDITIONS IN ARCTIC TUNDRA REGIONS FOR CLIMATOLOGICAL APPLICATIONS USING MICROWAVE RADIOMETRY

by

Edward Jinhyong Kim

A dissertation submitted in partial fulfillment
of the requirements for the degree of
Doctor of Philosophy
(Electrical Engineering and
Atmospheric, Oceanic and Space Sciences)
in The University of Michigan
1999

Doctoral Committee:
Professor Anthony W. England, Chair
Professor John F. Vesecky
Professor Fawwaz T. Ulaby
Professor Henry N. Pollack

To my family.

ACKNOWLEDGEMENTS

I would like to thank my committee for their advice and time, and their encouragement. I especially wish to thank my advisor, Professor England, for his years of guidance and understanding, and for the opportunity to work on such an interesting project (which even included an element of adventure). I greatly benefited from his extraordinary level of commitment to training future scientists, and I will endeavor to follow his example of sincerity, integrity, and intellectual acuity during my own career.

I am no less grateful to the dozens of officemates, professional acquaintances, and friends (sailors and landlubbers alike) for years of encouragement and mutual stress relief activities.

My thesis work included significant efforts related to instrument construction and field campaigns. These would not have been possible without the assistance of many students and the staff of the UM Radiation Laboratory who helped to construct, test, deploy, and retrieve TMRS2, and who otherwise helped to make the REBEX-3 experiment a success. Other divisions of the University which provided expertise and facilities included:

Department of Electrical Engineering and Computer Science
Department of Atmospheric, Oceanic and Space Sciences
Department of Civil and Environmental Engineering
Matthaei Botanical Gardens

I am also deeply indebted to the following organizations for their technical and logistical support, data, and materials:

Alaska Department of Transportation and Public Facilities (ADOT/PF)
especially the crews of the Sagavanirktok River/Slope Mt. Maintenance Facility
Alaska Department of Natural Resources (DNR)
North Slope Borough, Alaska (NSB)
Water Research Center, University of Alaska Fairbanks (UAF)
US Geological Survey, Fairbanks, AK (USGS)
Alascom, Inc., Alaska
Toolik Field Station, Institute for Arctic Biology (IAB), UAF
Polar Ice Coring Office, UAF (PICO/UAF)
Polar Ice Coring Office, University of Nebraska, Lincoln (PICO/UNL)
Arctic Wilderness Lodge (AWL), Alaska
San Diego State University (SDSU)
University of California, Berkeley
Bright Electric, Fairbanks, AK
US Army Cold Regions Research Laboratory (CRREL)
Dowell-Schlumberger, Deadhorse, AK
Haliburton Services, Deadhorse, AK

Marine Biological Laboratory, Woods Hole, MA
Campbell Scientific, Inc., Logan, UT
Radiation Energy Balance Systems, Inc., Seattle, WA
National Snow and Ice Data Center
NASA Marshall Space Flight Center DAAC
National Climatic Data Center
Remote Sensing Systems, Inc.
NASA Goddard Space Flight Center

During my studies, I was supported by funding from NASA, USGS, and NSF, by a Benton Fellowship from the EECS Department, and by a Rackham Dissertation Fellowship.

TABLE OF CONTENTS

LIST OF TABLES

LIST OF FIGURES

CHAPTER 1

Introduction

1.1 Overview

The research presented in this dissertation traces its development from earlier research on frozen-ground radiometry by members of the Microwave Geophysics Group [105, 106, 21, 47] and permafrost remote sensing ideas. The approach which evolved, namely, using a combination of physically-based land surface process modeling and microwave emission modeling, was a natural adaptation of related research developed for non-permafrost regions vegetated with prairie grass [52]. I will begin here by placing this dissertation in the broader context of trying to understand the land component of the earth's climate system and its relationship to climate change, leaving more detailed background material to be presented in each chapter.

1.2 Motivation

1.2.1 Why study land surface processes?

Land surface processes (LSPs) regulate the fluxes of radiant energy, sensible heat, latent heat, moisture, and momentum at the land-atmosphere boundary, determining the response of the land to atmospheric forcing and the feedbacks to the atmosphere [90]. These processes are complex and interrelated. For example, melting snow decreases the albedo of the land surface, allowing more solar radiation to be absorbed. The warmer land leads to higher air temperatures, which can lead to further melting of snow cover in a positive feedback loop.

However, warmer temperatures will also affect evaporation, which may lead to increased cloud cover that can reduce warming through the reflection of incoming solar radiation [59, 12].

The characterization of land surface processes within atmospheric general circulation models (AGCMs) is extremely important to provide realistic land-atmosphere boundary behavior for the atmospheric component of climate models as well as surface state information. Yet, due to computational constraints, operational LSP models cannot afford to implement detailed physical treatments of these processes, relying heavily instead on various parameterizations [90]. The performance of LSP models is a major source of uncertainty in current climate change predictions [39], and the subject of studies such as the Project for Intercomparison of Land-Surface Process Schemes (PILPS) [31], designed to assess the effects of differences among LSP models, especially when fully coupled to AGCMs. Improved LSP models would also be beneficial to numerical weather prediction models (NWPMs) [90]. Note that while a "good" LSP model may generate reasonable boundary conditions for an AGCM or an NWPM, it will not necessarily generate a high-fidelity description of the temperature or moisture state of soils or vegetation.

1.2.2 Why study *arctic* land surface processes?

The arctic is a key component of both the atmospheric and oceanic general circulations, through which arctic processes interact with global processes [2]. Several climate change scenarios have predicted that the largest changes would occur at high latitudes [40]. For example, doubled-CO_2 AGCM simulations predict increases of global mean surface air temperature of 1–4.5° C by the year 2100 [40], with even greater warming expected in certain parts of the arctic [56].

Both short-term and long-term warming trends have already been observed in the arctic [14, 29]. Decadal or longer-term warming is apparent in arctic borehole temperature profiles [73, 51], has resulted in a loss of permafrost [102, 40], and will result in changes in the regional

ecosystems [69, 61]. Warming would promote thawing of the permafrost, which would affect the hydrology of the arctic through a deeper active layer (the upper portion of the tundra and permafrost which thaws during the summer), increased soil moisture storage, warmer soil temperatures, and increased evaporation [32]. The retreat or advance of permafrost areas may serve as a good indicator of long-term regional and global warming or cooling trends because permafrost temperatures reflect the integrated effect of years and decades of surface temperature conditions.

Tundra is the most representative biome of arctic land regions underlain by permafrost, covering approximately 5.4% of the land surface of the earth ($\approx 8 \times 10^6$ km^2) [79]. These regions are an important source and sink of carbon dioxide and methane, globally important greenhouse gases. Studies by Oechel, et al. [69] indicate that during the 1990's, the tundra of the Alaskan North Slope has been on the borderline between being a net carbon source and a net carbon sink. The processes that regulate the uptake and release of carbon by the tundra are affected by changes in soil moisture and temperature, yet many of these processes are not well understood [94]. Furthermore, the unique aspects of arctic climate system components often make them sensitive to change. For example, the thermal and hydraulic properties of the active layer undergo significant changes during the annual freezing and thawing transitions.

Climate warming could result in a net release of carbon in the form of greenhouse gases [70, 74]. This is potentially quite significant since tundra vegetation and soils contain an estimated 7.2% (4×10^9 metric tons) of the world's organic carbon [79], and a recent study [74] suggests that an equivalent additional amount has not been included in such estimates because it lies just below the present-day active layer.

The sensitivity of arctic systems to change may make the arctic an early indicator of global climate change [6]. The already-observed trends and the magnitude of arctic climate change predictions present a strong case for improved monitoring of arctic conditions and validation of arctic climate models. The research described in this dissertation was con-

ducted as part of one such effort, the Land-Atmosphere-Ice Interactions (LAII) component of the NSF Arctic System Science program.

1.2.3 Why use passive microwave remote sensing?

The lack of adequate observational data has been repeatedly recognized as a serious impediment to climate model improvement [39, 40]. This lack is particularly felt in remote areas, where observing stations are widely scattered [96]. Because the vastness and inaccessibility of arctic lands preclude a significant increase in the number of surface observing stations, satellite remote sensing may be the only practical and economical approach to uniform, frequent observations of climatological forcing and response variables at regular intervals and at useful spatial resolutions[1] [81]. Current climate models employ grid cells which are hundreds to thousands of square kilometers in area [82]. It is worth noting that while the spatial resolution of current passive microwave satellite sensors (10's of km) is not as good as that of satellite radar instruments or visible-light sensors (km or sub-km), the resolution *is* comparable to that of current climate models.

Even if a network consisting of one surface measurement site per grid cell were practical and economical (5700 sites worldwide for 300×300 km cells), some climate modelers would argue that point observations are of very limited value in comparison to variables at the resolution of current models [88]. Model variables do not necessarily correspond to measurable quantities. For example, what is the "surface temperature" of a 300×300 km area? And, a network sufficiently dense to produce useful areal averages (if that is what would be required) would likely be uneconomical or impractical or both. Furthermore, climate-related studies, by their long-term and large-scale nature, are especially limited by the consistency (or lack thereof) of the instruments and techniques employed in the measurements [103, 44]. A satellite-based observation system can use the same instrument in the same way every

[1]The linkage between observable quantities such as brightness temperature or backscattering coefficient and climatological variables (for example, latent heat flux) is usually not direct. This discussion presumes satisfactory linkages can be found.

time and every place a measurement is made, which may be for several years over the entire earth.

There are numerous polar-orbiting platforms providing excellent spatial and temporal coverage of high-latitude regions. Microwave remote sensing offers advantages that are especially well suited to the observation of these regions. Microwave sensors (active and passive) are far less susceptible to interference by clouds than are optical or infrared sensors, and they do not depend on solar illumination, permitting observations at night and throughout the long polar winter.

Microwave radiometry is particularly sensitive to temperature and moisture distributions in vegetation canopies and in the underlying soil, while not exhibiting radar's sensitivity to vegetation structure and limitations on vegetation column density [19]. For example, direct sensing of soil moisture is possible through vegetation with column densities up to several kg/m^2 [42] (vs. 0.4 kg/m^2 for radar), with lower frequencies (1–2 GHz) having greater "penetration". While no lower frequency satellite radiometers are currently operational[2], higher frequency radiometers such as the Special Sensor Microwave/Imager (SSM/I) instruments have been operational since 1987 aboard the sun-synchronous polar-orbiting U.S. Defense Meteorological Satellite Program (DMSP) satellites. Each makes typically four passes per day over points on the North Slope of Alaska (68–72 N latitude). And, there are typically two operational satellites in orbit with staggered overflight times [3], making continuous radiobrightness observations at 19, 22, 37, and 85 GHz. The approach taken in this dissertation at these frequencies should apply at lower frequencies whenever such observations become available.

Active microwave sensing techniques should eventually complement the passive techniques, for instance, by quantifying the canopy biomass (and therefore its masking of mi-

[2]The Advanced Microwave Scanning Radiometer (AMSR)– slated to fly in the next 2–3 years will include X-band (10 GHz) and C-band (6 GHz) radiometers. There are also proposals to fly L-band (1.4 GHz) satellite radiometers in the next 3–5 years (Hydrostar and Microwave Imaging Radiometer with Aperture Synthesis-MIRAS).

crowave emission from the underlying soil). However, as a first step, in this dissertation I consider only absorption and emission of microwave radiation, since this was found to be sufficient for model validation purposes in a previous related case [52].

1.3 Approach

Earlier work for grass canopies showed that under all but quite dry conditions, *at the SSM/I frequencies* used in this dissertation, the majority of observed emission comes from the vegetation and not the underlying soil [23, 45]. Thus instantaneous observations alone provide very little information on *soil* temperature and moisture, and direct inversion is not a robust method for estimating these quantities. Even in cases where instantaneous observations can be directly inverted to estimate one quantity (e.g., L-band brightness and near-surface soil moisture), inversion of other quantities (e.g., a moisture profile or latent heat flux) is not practical.

The approach followed instead is to rely on a land surface model to provide the connection between observable "surface" quantities and conditions deeper within the canopy and soil. The LSP model is then linked to a microwave emission model (an 'R module') which predicts radiobrightness based on the temperature and moisture profiles within the system. The combination is referred to as an LSP/R model. Thus radiobrightness observations are a means of remotely assessing model accuracy. But, since radiobrightness is an integrated quantity, it is not unique; different vertical profiles of temperature and moisture can produce the same radiobrightness. However, a specific forcing history and information about the particular soil and vegetation under observation can constrain the problem.

Deviations between predicted and observed radiobrightnesses could then be used to "nudge" or otherwise correct the model state in a regular fashion. Current operational numerical weather prediction models routinely assimilate remotely sensed and in-situ observations through such techniques [80].

By assimilating passive microwave observations made over a period of time to constrain

the model, surface fluxes (e.g., latent and sensible heat), as well as near-surface and subsurface temperature and moisture conditions may be determinable for areas with relatively thin vegetation such as tundra and prairie. Assimilation of satellite observations could permit regular wide-scale estimates to be made with a spatial resolution comparable to the sensor footprint. Again, these estimates would come from the model state, not from a direct inversion of radiobrightness data.

Note that while assimilation of satellite radiobrightness observations is the ultimate goal of this approach, the scope of this dissertation includes only the forward LSP/R modeling—i.e., the comparison of tundra LSP/R model predictions against ground observations—and a separate comparison of ground-based vs. satellite radiobrightness observations.

1.4 Questions Addressed by this Dissertation

Thus, the main questions addressed in this dissertation are:

How well can we predict microwave emission by snow-free tundra underlain by continuous permafrost? Does it require special modeling considerations beyond those found adequate in a previous lower-latitude prairie grass case [52]?

How well might passive microwave satellite observations be used to estimate surface conditions in such tundra/permafrost areas? Specifically, how well do ground-based radiobrightness observations match satellite radiobrightness observations? And, what comparison issues are there (what are the differences due to?) and how might they affect such estimates?

1.5 Dissertation Organization

The Radiobrightness Energy Balance Experiment 3 (Rebex 3) is described in Chapter 2. This field experiment was designed to collect data to support the development and validation of the tundra LSP/R model.

An LSP/R model for snow-free tundra is described in Chapter 3, which also contains a

comparison of model predictions vs. field observations.

The comparison of ground-based and satellite radiobrightness observations is presented in Chapter 4. Included in this chapter is a description of a custom SSM/I EASE-Grid processor developed to provide gridded SSM/I data for the comparison.

Appendix A contains a chart for converting Rebex 3 Julian day number to calendar dates, and annual graphs of patched and interpolated Rebex 3 field data.

CHAPTER 2

REBEX-3 Field Experiment

2.1 Background and Overview

Radiobrightness Energy Balance Experiment 3 was undertaken to collect a unique set of long-term co-located microwave brightness and micro-meteorological observations in order (a) to support development of the tundra land surface process/radiobrightness model, and (b) to make comparisons of contemporaneous ground-based and satellite brightness observations.

The current experimental knowledge of the surface energy balance of arctic tundra has, for the most part, been obtained only within the last five decades. Ohmura [71] has published an extensive historical review on the subject, including research sites throughout the arctic. In Alaska, the first energy balance measurements were made at Barrow by Bryson on two days in June, 1953 [11]. Mather and Thornthwaite made the first thorough and longer-term observations (at Barrow) in 1956–58 before and during the International Geophysical Year [57, 58]. In the 1960's and 1970's, several detailed studies were carried out for the hydrologically important snowmelt period at Fairbanks by Wendler [100], and at Barrow as reported by Weller and Benson [97], Weller *et al* [98], and Weller and Holmgren [99]. Intensive measurements of the tundra thermal regime at Barrow were made in 1970 in cooperation with the Tundra Biome Program as reported by Brown and West [10]. The latter two studies were conducted as part of the International Biological Program. Note that except for the Fairbanks work, the bulk of the tundra observations and studies were

concentrated at Barrow, and therefore reflect characteristics of the arctic coastal plain and coastal tundra. Compared with inland tundra, coastal tundra is flatter, wetter, and has much more standing water. In many areas, thaw ponds and small lakes would cover a significant fraction of a satellite sensor's footprint. Also, Harazono *et al* [30] and Yoshimoto *et al* [104] found the coastal microclimate to be bimodal, depending on whether winds were onshore or offshore.

For passive microwave remote sensing applications, sensor footprints are 10's of kilometers in size. Particularly for comparison with ground-based observations, it is initially desirable to focus on sites which are inland from the coast—i.e., sites for which the satellite footprints could exclude the ocean with its distinctly different signature and adjacent tundra areas. In the 1980's and 1990's, micro-meteorological field data from such areas became available along the north-south transect of the Trans-Alaska Pipeline route (see Fig. 2.2). Examples of these efforts include the projects of Hinzman and Kane [35, 43, 32], the Long Term Ecological Research (LTER) Program [83, 13], and the Land-Atmosphere-Ice Interactions (LAII) Program of the U.S. National Science Foundation (of which this dissertation research was a part) [70, 55].

However, none of these measurements included the microwave and thermal infrared brightnesses critical for the research described in this dissertation. Preceding REBEXs had acquired such data only for grass-covered areas in Michigan (REBEX-0, [46]) and South Dakota (REBEX-1, [27]), so a new REBEX was necessary.

REBEX-0 and REBEX-1 employed the first version of the Tower Mounted Radiometer System (TMRS1), developed by Galantowicz [22], and provided us with over 200 days of experience operating micro-meteorological instruments and microwave radiometers under field conditions at sites up to 1500 km away. For REBEX-3, we would be 6000 km away, and deployed for twice as long. The number of sensors was increased from 18 to 55, and the instrument system (TMRS2) had to be substantially reconfigured and hardened to withstand the rigors of unattended operation in the arctic. Nearly two years and the help

of 8 students were required to complete the upgrade to TMRS2.

Equally challenging and critical to the overall success of REBEX-3 were solutions to the various logistical issues associated with finding a site in, getting to, and operating in arctic Alaska. In this chapter, I will describe the experimental site, the field experiment, and the data collected, including the re-design of the instrument system, calibration, and problems and fixes.

2.2 Site Choice and Description

Many factors had to be weighed in selecting an experimental site, particularly for a long-duration experiment in such a remote area. Purely practical considerations played a large role in determining the final location, what measurements were made, how and when they were made, and the usefulness of the resulting data.

In this section, I will describe the site requirements, both scientific and non-scientific, and the final location which was selected for REBEX-3.

2.2.1 Scientific Considerations

Continuous Permafrost

The site had to be located within a continuous permafrost area—to help with the assessment of upscaling remote sensing observations to satellite pixel-size areas. "Continuous permafrost" refers to a contiguous area completely underlain by permafrost. "Discontinuous permafrost" refers to a transitional belt between continuous permafrost areas and non-permafrost areas; some spots are underlain by permafrost while others are not. In Alaska, only southern coastal areas are permafrost-free, while continuous permafrost covers roughly the area north of the Arctic Circle (Fig. 2.1). "Continuous" and "discontinuous" are not precise technical definitions, but are useful qualitative descriptors here.

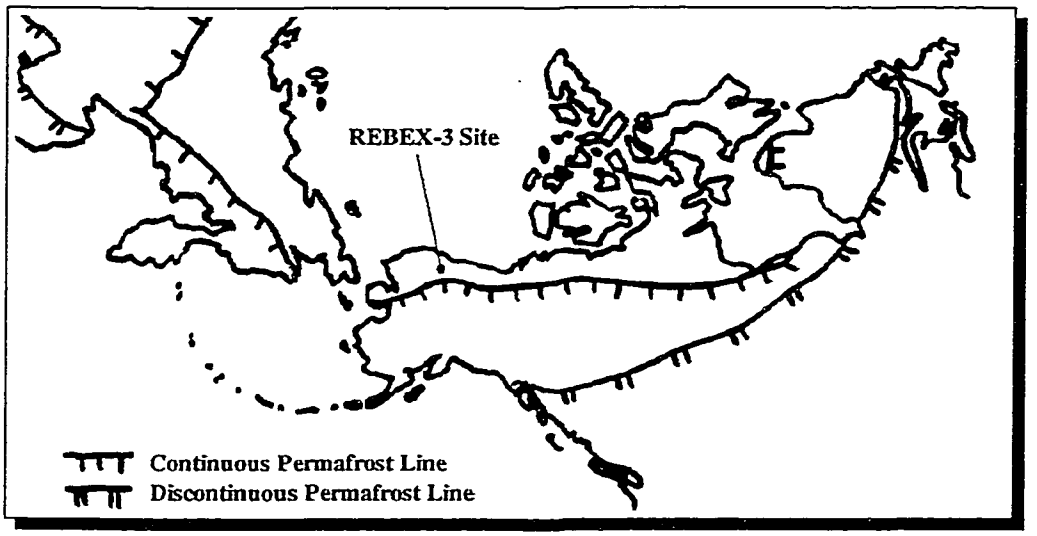

Figure 2.1: Continuous and discontinuous permafrost regions.

Representative Land Cover

The land cover should be representative of the region—the tundra biome in this case. Permafrost also underlies areas of the boreal forest biome, so the tundra-boreal forest ecotone (boundary) does not necessarily match the permafrost/non-permafrost boundary.

Homogeneous at the SSM/I Spatial Resolution

The land cover should be homogeneous and ideally non-mountainous on the spatial resolution of SSM/I (~50 km, after spatial resampling), to simplify the comparison of ground-based and satellite microwave observations.

Season

Field data were needed for the snow-free season, since I was interested in tundra-atmosphere interactions rather than snowpack-atmosphere interactions. The snow-free season on the North Slope begins in May and can extend into September. The snowmelt period and initial snow accumulation period were also of interest.

2.2.2 Logistical Constraints

U.S. Territory

The site had to be within the United States. After consulting the U.S. Customs Service, we found that transporting equipment to and operating at a site in Canada would have been more complicated than transporting equipment *through* Canada to Alaska. The only U.S. territory with large expanses of tundra is the North Slope of Alaska.

Electrical Power Requirements

The field instrument system included several components which required continuous AC power. These were primarily the control computer, the ovenized microwave radiometers, heaters for the tower-mounted equipment, and 3 kW of heaters for the support trailer which housed the computer. Total electrical power needs were under 7 kW during the winter, and 3–4 kW during the summer. These demands were too large for batteries or solar panels (especially at high latitudes), and running a generator without on-site personnel was deemed too complicated. So, we were restricted to sites with existing electrical power and sufficient spare capacity for our needs.

Communications Requirements

The instrument control computer could be slaved to another computer over a standard telephone connection for status checks, remote control, and data transfer. During previous REBEXs, this capability had proven to be extremely useful. Some form of communications would also be a valuable safety aid.

On the North Slope, telephone options were limited to terrestrial radiotelephones and satellite telephones. Both options were expensive, but technically feasible from any location.

Road Access but Undisturbed Tundra

Transporting the field instrument system to the site would be most easily accomplished if the site were connected to the road network for two reasons. First, off-road vehicle traffic

over the North Slope tundra is forbidden until the tundra is frozen sufficiently hard in the winter. This is done to prevent vehicle tracks from scarring the fragile vegetation. Scars take decades, possibly centuries to fade away. Second, transportation by aircraft is extremely expensive.

Ideally, the site would be reachable from Ann Arbor by road with a parking spot for a trailer immediately adjacent to a tundra area which had not been "disturbed" from its natural condition by proximity to roads, facilities, or human activities. At first, this seemed like a mutually exclusive set of requirements. Fortunately, practically all human activity along the pipeline corridor is confined to the road, the pipeline right-of-way, and occasional facilities—a by-product of strict rules, and uncooperative terrain. Typically, the tundra 10–20 meters away from these showed no visual trace of disturbance. Locating our instruments 30 meters away from the nearest disturbed tundra would be sufficiently "undisturbed".

Equipment Security and Personnel Safety

Leaving valuable equipment unattended for long periods of time in a remote area visited by hunters was unappealing. A shiny metal box (containing the radiometers) on the only tall object for miles around would make an attractive target. Law enforcement is scarce in most of the North Slope. Staffing our site was not practical, so proximity to a manned facility was about the only factor which might deter vandalism.

Medical assistance is also scarce on the North Slope. For serious injuries, the nearest "facility" was a first aid station at Prudhoe Bay, up to 160 km to the north. And, the nearest hospital was in Fairbanks, over 600 km to the south. Air evacuation to Fairbanks (weather permitting) was available by contacting the North Slope Borough in Barrow, 600 km to the west. That required a working telephone, which was not always available. Thus, proximity to a manned facility was advantageous for the security and safety of both equipment and personnel throughout the experiment.

latitude	68.76306°
longitude	148.88194°
elevation	500 m
slope, aspect	very flat
soil	Pergelic Cryaquepts ([61])
vegetation	moist acidic tussock tundra: sedges, mosses, lichens
active layer depth	50 cm maximum

Table 2.1: REBEX-3 site details.

2.2.3 The Saganavirktok River ADOT Site

We were very fortunate to obtain permission to set up our instruments and to conduct our experiment at one of only two sites in the area which actually met all of the above requirements: adjacent to the Alaska Department of Transportation Saganavirktok (Sag) River Maintenance Camp (see Fig. 2.3) on the North Slope at mile 306 on the Dalton Highway (the official name for the Pipeline Haul Road). The Sag River DOT camp is 30 km north of ecological research sites in the Toolik Lake/Imnaviat Creek area and 50 km south of sites at Happy Valley (Fig. 2.2) in a region along the Haul Road transect where few other energy balance measurements suitable for model input were made. These distances are such that at scales of both the 20 km resolution of the mesoscale Arctic System Model (ARCSyM, [54]) and the 25 km Equal Area Scalable Earth-Grid (EASE-Grid, [9]) satellite data grid, a grid cell containing the REBEX-3 site would be between cells containing the Toolik/Imnaviat vicinity and the Happy Valley vicinity (see Fig. 4.12 for an EASE-Grid map).

2.2.4 Related Nearby Sites and Shared Logistics

By making observations on the North Slope we could also benefit from the experience, shared logistics, and data of other research projects in the area, most of which were part of the NSF Arctic System Science (ARCSS) Land-Atmosphere-Ice Interactions (LAII) program. These included a wide variety of hydrological, ecological, and geophysical investigations. Figure 2.4 shows the locations of nearby snow, soil, and meteorological data

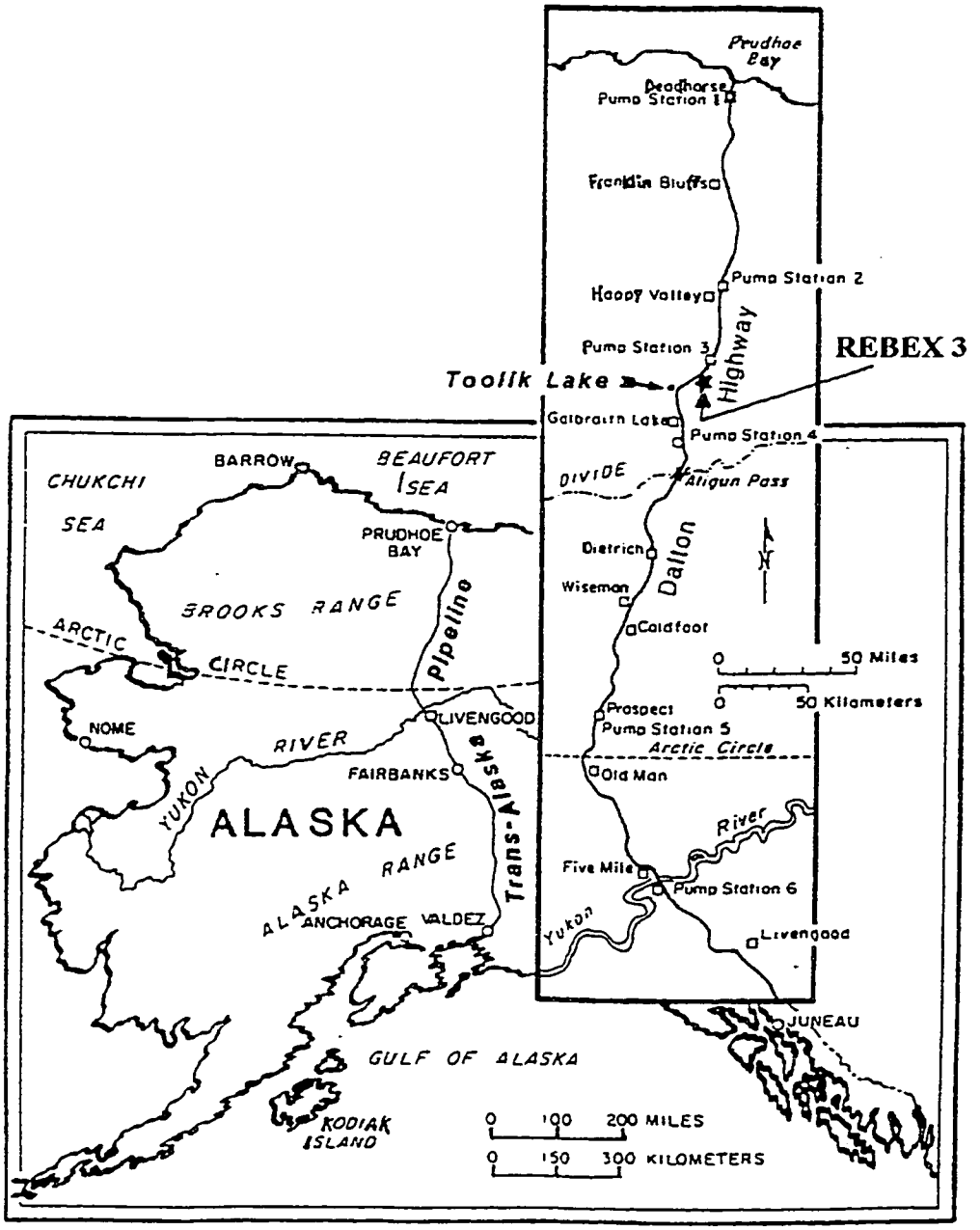

Figure 2.2: Location of REBEX-3 site in Alaska (adapted from IAB map).

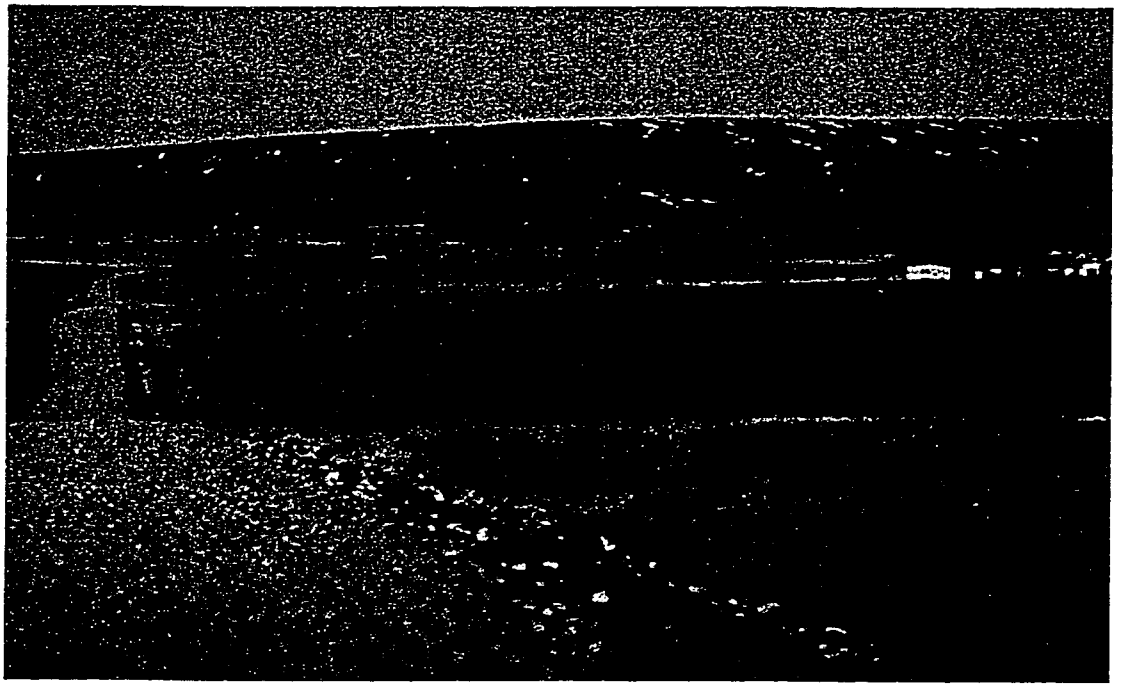

Figure 2.3: REBEX-3 site at Sag River, Alaska. View facing north along Pipeline Road to Prudhoe Bay. Buildings on right are the DOT camp. Small white dot near center of image is TMRS2 trailer. Distance across center of photo is 0.5 km.

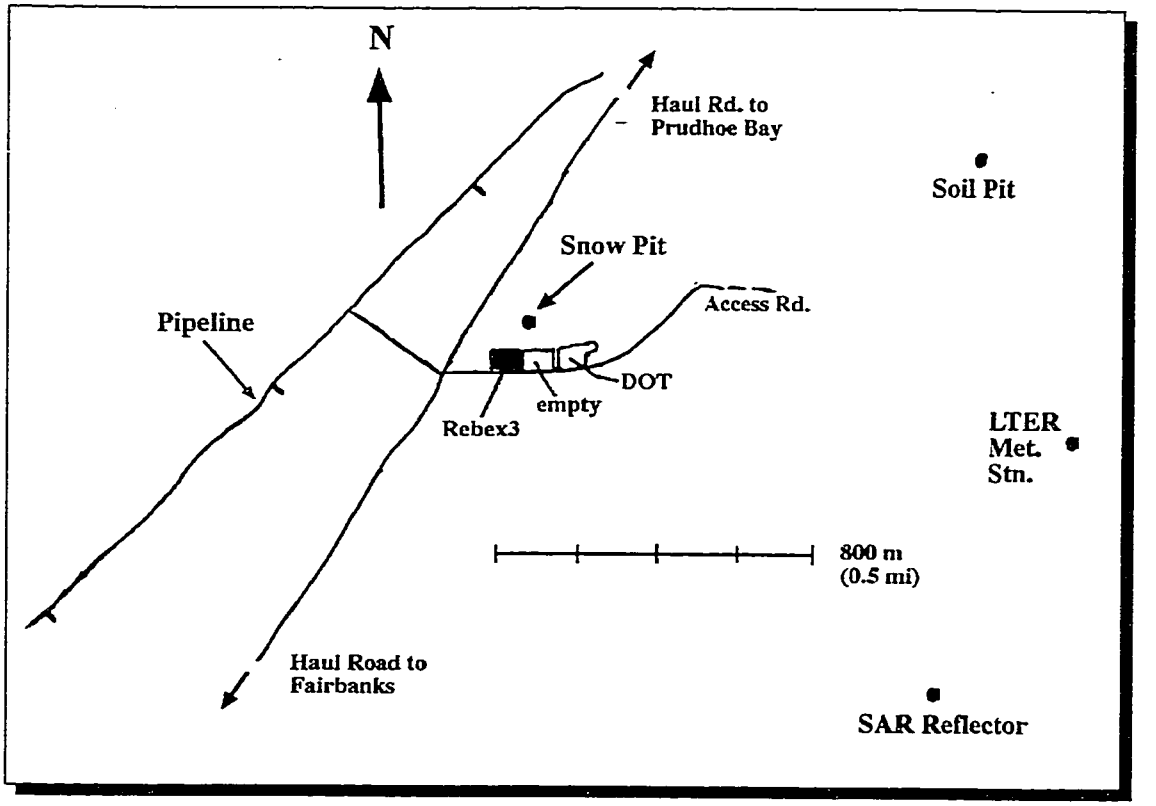

Figure 2.4: Nearby sites (traced from aerial photo).

collection sites, as well as a synthetic aperture radar (SAR) retroreflector.

Lodging, communications, shipping, and limited lab facilities and materials were available at various times from the University of Alaska Institute of Arctic Biology (IAB) Toolik Field Station, the NSF LAII Happy Valley Camp, the Arctic Wilderness Lodge, and oilfield facilities in Prudhoe Bay.

2.3 Methods and Materials

2.3.1 Overview of Tower Mounted Radiometer System 2

All of the data collected during REBEX-3 were collected using the Tower Mounted Radiometer System 2 (TMRS2). TMRS2 is a ground-based SSM/I simulator and surface energy balance monitoring system [25].

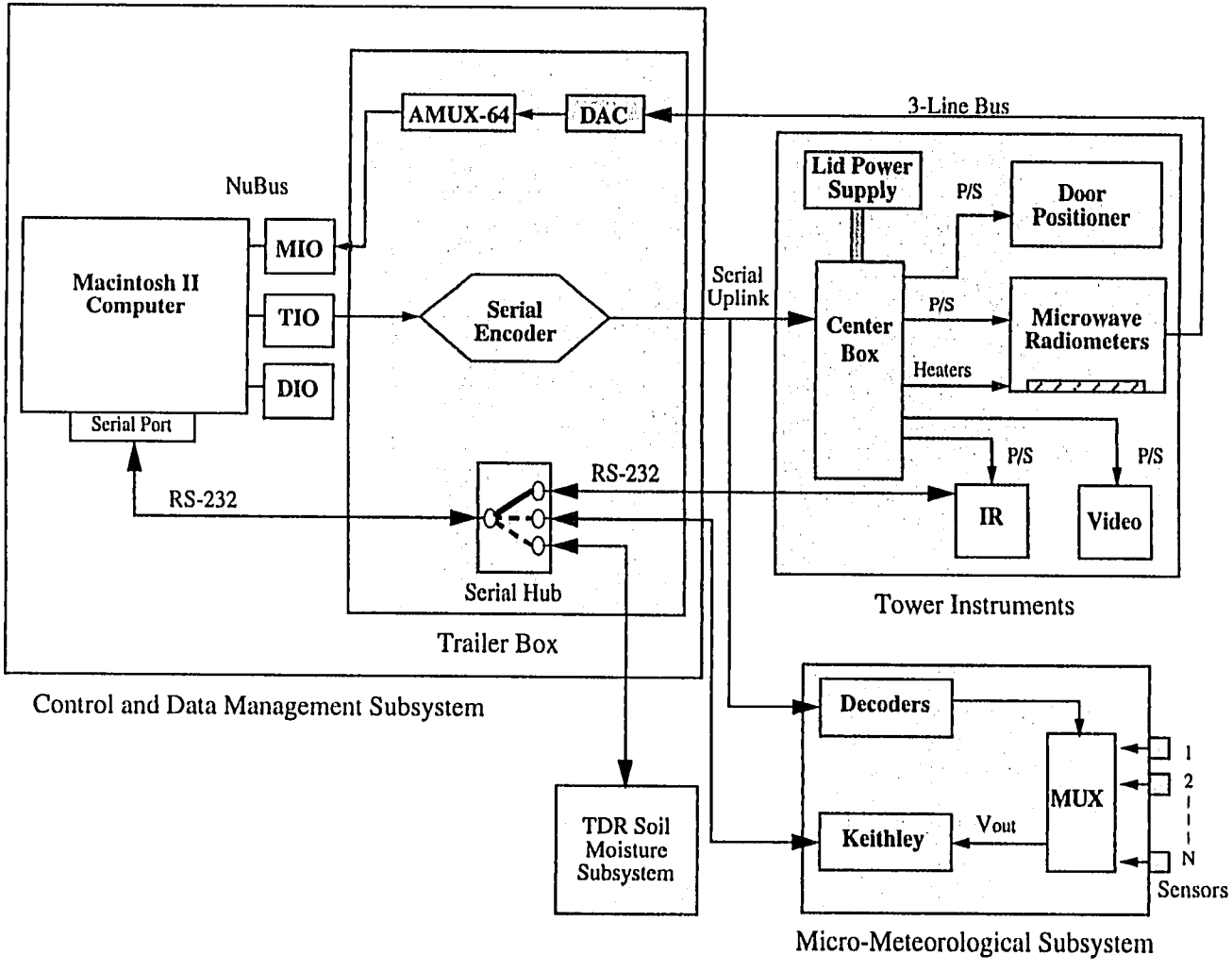

Figure 2.5: TMRS2 system block diagram. Shaded items were new or upgraded components. (Adapted from Fischman [25].)

The primary application of TMRS2 (and its predecessor, TMRS1) is in the collection of long-term (months) time-series data sets at sites representative of various biomes in support of land surface process modeling and remote sensing research. The system is also used in support of studies in the passive remote sensing of soil moisture, frozen/thawed soil state determination, permafrost, and snow.

As such, it is environmentally hardened and designed to operate autonomously with remote monitoring and control capabilities via a low-bandwidth communications link such as a typical long-distance voice telephone channel. After REBEX-3, TMRS2 was deployed for REBEX-4, a 1996 summer prairie experiment in Sioux Falls, and REBEX-5, part of the 1997 Southern Great Plains Hydrology experiment at the Atmospheric Radiation Monitoring (ARM) Program's Cloud and Radiation Testbed (CART) site in Oklahoma.

TMRS2 is composed of a Radiometer Subsystem, a Micro-Meteorological Subsystem (MMS), and a Control and Data Management Subsystem (CDMS). These subsystems are described in the following sections, with emphasis on the increased capabilities I added and the improvements and changes I made to upgrade the system for service in the arctic (shaded items in Fig. 2.5).

2.3.2 Instrument System Description and Improvements

Our experiences during REBEX-0 and REBEX-1 convinced me that major changes and enhancements in nearly all parts of the TMRS system would be needed to meet the goals of REBEX-3. After discussions with researchers who were already familiar with North Slope conditions, I outlined the following system-wide TMRS performance requirements and improvements.

- New sensors and increased number of certain existing sensors.
- Increased operating temperature range: -40° C to +30° C.
- Survivability to -55° C.

- Wind resistant to over 130 kph (80 mph).
- Improved tolerance of frost, ice, and snow.
- Self-supporting on uneven and unstable ground. Tussock tundra is lumpy and spongy.
- Animal and insect resistant. Bears and other large animals had knocked over other researcher's instruments. Smaller animals had gnawed through cables. Mosquitos had clogged openings.
- Tundra instruments locatable 30 m from support trailer.
- Improved mechanical ruggedness.
- Improved reliability over TMRS1 (hardware and software).

2.3.2.1 Microwave Radiometers and Tower Equipment

In order to limit the amount of mechanical redesign and the final wind area, the size of the tower housing for the microwave and IR radiometers was not increased. This proved to be a severe constraint as a significant amount of new hardware was to be installed in the housing.

The TMRS2 microwave radiometers retained the basic TMRS1 design at the block diagram level (Fig. 2.6). The receivers were single-conversion double sideband units operating in total power mode with better than 0.1 K resolution. All TMRS2 radiobrightness observations during REBEX-3 were conducted in total power mode. The TMRS2 radiometers were functionally capable of (unbalanced) Dicke mode operation, but we had had switch failures in the past, and I decided that since total power mode involved much less switching, the probability of switch failure was lower than in Dicke mode. The packaging density within the radiometers and the remoteness of the field site would make field replacement of a switch difficult, time-consuming, and costly.

A second linear polarization was added to the 19 and 37 GHz radiometers. The change

was not made to the 85 GHz radiometer due to the high cost of the additional microwave components and the marginal scientific usefulness of a second polarization at that frequency.

The TMRS1 radiometers had a "split" RF chain. The output of the IFs were routed through coaxial cable from the housing down the tower to detectors in the CDMS trailer. The cables were directly exposed to the weather and mechanical flexing. The radiometer outputs were digitized in the trailer. The TMRS2 radiometers were of a self-contained design: power went in and data bits came out. The entire RF chain plus post-detection amplification and digitization were included inside each radiometer. Along with the extra hardware for a second polarization, this doubled or tripled the volume of the components which had to fit inside the radiometers (shaded in Fig. 2.6). Smaller components and a denser layout were used to make everything fit. A modified radiometer mechanical design made the innards more accessible (Fig. 2.8).

An adjustable internal DC voltage allowed the radiometer output voltage range to be offset to avoid saturation. The voltage was temperature dependent, and also drifted over time. Knowledge of this voltage was critical for calculating brightness temperatures. In TMRS2, I added the capability to measure and record this important variable.

In TMRS1, radiometer temperature sensors were each wired directly back to the CDMS trailer, resulting in a large number of long cables with the potential for noise pickup and ground loops. In TMRS2, the sensor outputs were digitized inside each radiometer and multiplexed along with the radiometer output itself for serial transmission back to the CDMS (Fig. 2.7).

The TMRS2 radiometer specifications are listed in Table 2.2.

I added multiplexing of the CDMS command signals to the tower housing, reducing the number of wires which would otherwise have been necessary. The command uplink and the tower data downlink were transmitted over a new 1Mb/s digital serial link which used inexpensive plastic optical fiber. I tested the plastic fiber for cold temperature tolerance at -80° C using dry ice.

center freq. (GHz)	19.35	37.0	85.5
polarizations	H,V	H,V	V
IF bandwidth (MHz)	10–250	100–1000	100–1500
postdetection bandwidth	20 kHz		
integration time	1–2 s		
receiver self-noise, T_{REC} (K)	840	1280	3270
NEΔT (K)	0.05	0.04	0.07
antenna 3dB beamwidth	10°		

Table 2.2: TMRS2 radiometer specifications. NEΔT values assume 300 K antenna temperature, 1-second integration time, and gain variations $\Delta G/G = 10^{-5}$.

The TMRS2 radiometer thermal control was based on the successful TMRS1 design. The purpose of the temperature control was to reduce or eliminate temperature-dependent radiometer gain and offset variations.

The outer radiometer cases were lined with foam insulation. The receiver circuitry was mounted inside an inner metal box on a 6 mm-thick aluminum plate to provide a common high thermal conductivity core. Areal electric heating elements were attached to the plate and controlled by a proportional-integral-derivative (PID) routine in the CDMS software. Small fans circulated air within the inner box and between the inner and outer boxes to prevent the formation of convection cells and dead air space, thereby reducing internal thermal gradients. The tower housing also acted as a third layer of thermal isolation. The cutouts for the antennas were covered with mylar film to keep out ambient air and moisture. The horn antennas represented a large thermal pathway between the outside air and the receiver, so I attached heaters in order to reduce the temperature gradient along the antenna thermal path and minimize heat loss. The temperatures of the internal reference waveguide load in each radiometer could be stabilized to 0.2 K or better after adjustment of the PID constants.

The TMRS2 radiometer sky reflector was enlarged to reduce sidelobe and spillover biases. The reflector formed a hinged "door" covering the front face of the tower housing.

It opened during measurement cycles to allow the radiometers to view the ground. In intermediate positions, it acted as a reflector to provide estimates of downwelling microwave sky brightnesses. The larger door required a much more rugged motorized positioner than in TMRS1. Door position sensing was available from a sensor in the positioner (Fig. 2.12).

Frost and ice build-up could keep the door from closing or opening, and water on the door surface would affect sky brightness measurements. So, I added 700 W of heaters and thermal insulation to the back side of the new door. These heaters as well as the radiometer internal heaters were all operable from the CDMS trailer without the housing electronics turned on as part of the "cold start" capabilities of TMRS2.

In TMRS1, the power supplies for all the housing components were located in the CDMS trailer. This was not ideal as far as immunity to interference, ground loops, and voltage regulation were concerned.

So, in TMRS2, I moved the power supplies as close to the radiometers as possible—inside the tower housing itself. Individual voltage regulators were used for each active device, as physically close as possible inside the receivers. I added pre-regulation outside the radiometer boxes to minimize the ambient power dissipation inside each radiometer for reduced thermal gradient generation and improved temperature control. I also included temperature sensing for the housing supplies for cold start monitoring. Solid state relays were used for all load switching to eliminate any potential problems with mechanical relay contacts and to reduce total relay energization current.

High-power loads such as the heaters (1300 W total) and the AC motor for the door actuator were connected to separate "dirty" AC feeds from the CDMS trailer, in order to isolate the sensitive "clean" radiometer circuitry from switching spikes, voltage droop, etc.

The screw-type earth anchors for the tower guy wires would not hold in a peat soil and could not be inserted into permafrost. Instead, two sets of steel rods were hammered into the permafrost and used as anchors for each guy wire. This simple scheme worked so well that several of the anchors could not be removed at the conclusion of the experiment.

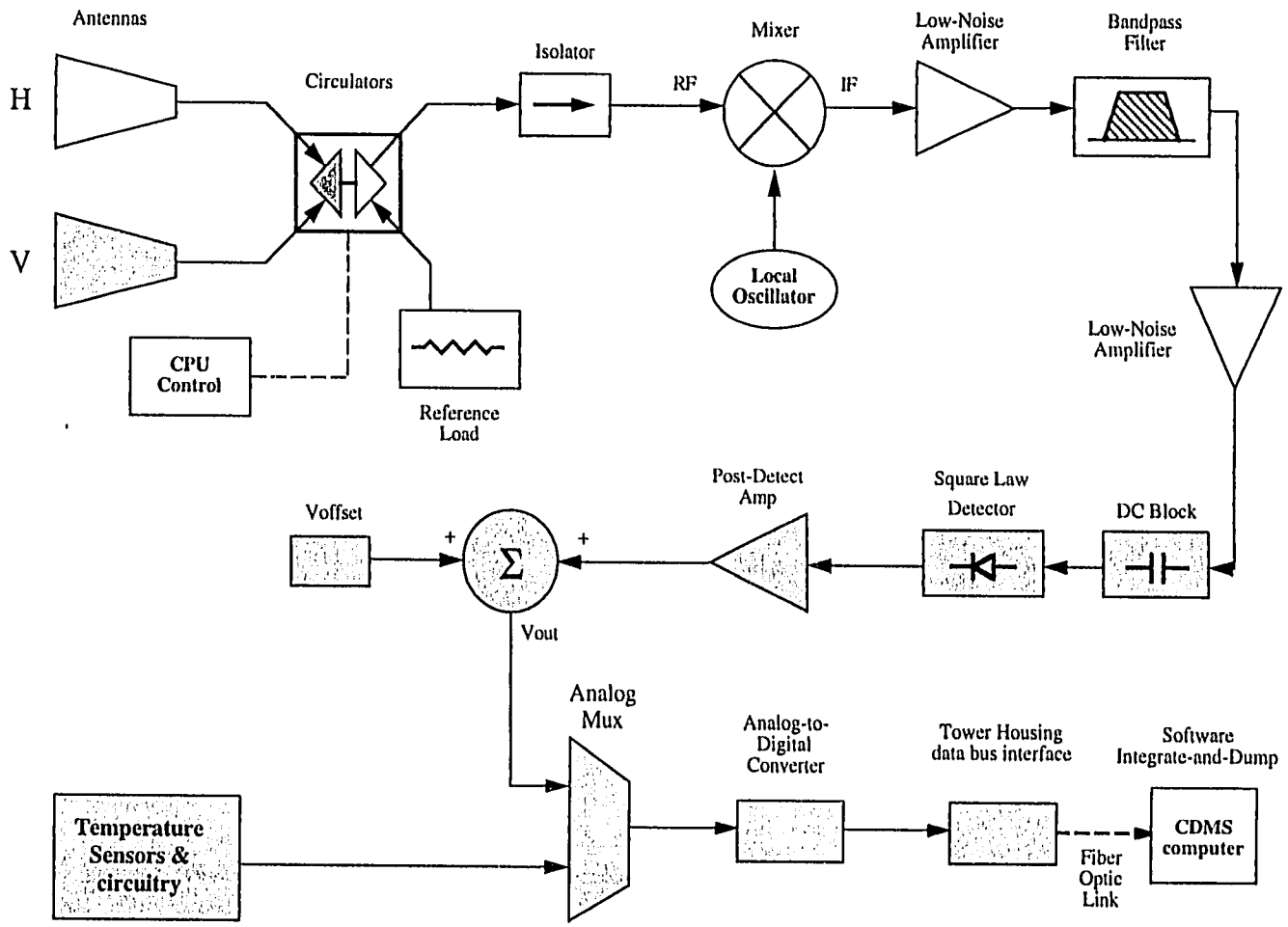

Figure 2.6: TMRS2 microwave radiometer block diagram. The 85 GHz radiometer had a single antenna and circulator. Shaded items were new components to locate inside the radiometer enclosures. (Adapted from Fischman [25].)

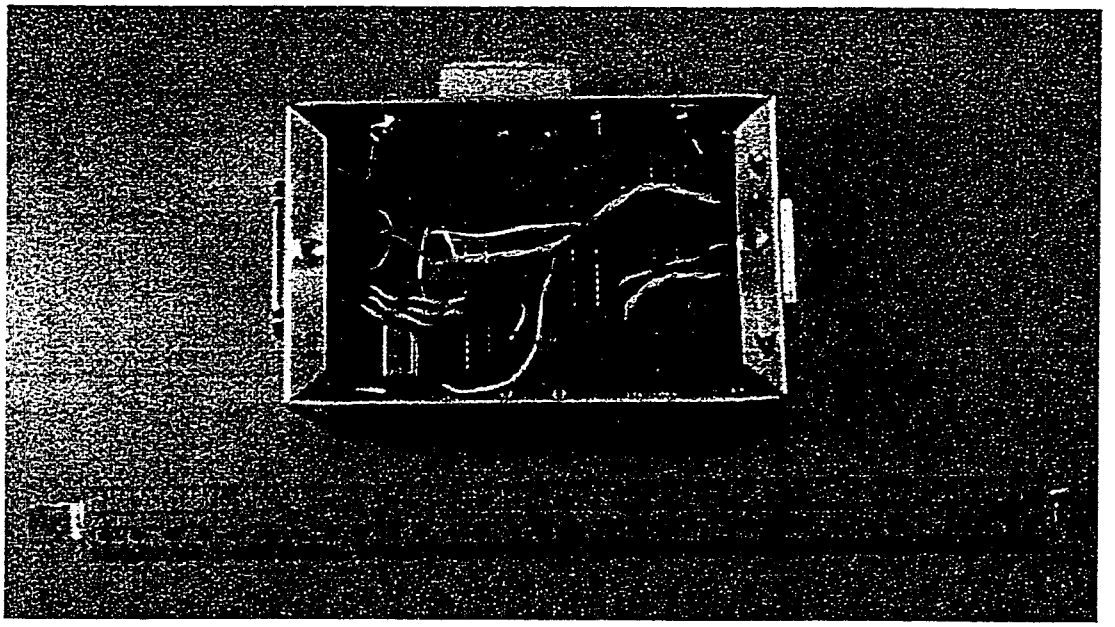

Figure 2.7: Compact radiometer signal multiplexer, A/D, and control interface module (one per microwave radiometer).

2.3.2.2 Micro-Meteorological Subsystem

A number of new sensors were added to the MMS, and the number of probes for other measurements was increased:

- Added: a 10-channel time domain reflectometer (TDR) automated soil moisture measurement subsystem, including a probe multiplexer converted from a proprietary serial interface to a parallel interface for connection to the CDMS.
- Added: a Bowen ratio sensible/latent heat flux measurement subsystem.
- Added: wind direction and speed sensors at 2 m height.
- Added: 12 snowpack temperature probes.
- Doubled: the number of soil temperature probes to 12.
- Increased: the number of soil heat flux sensors from 1 to 3.

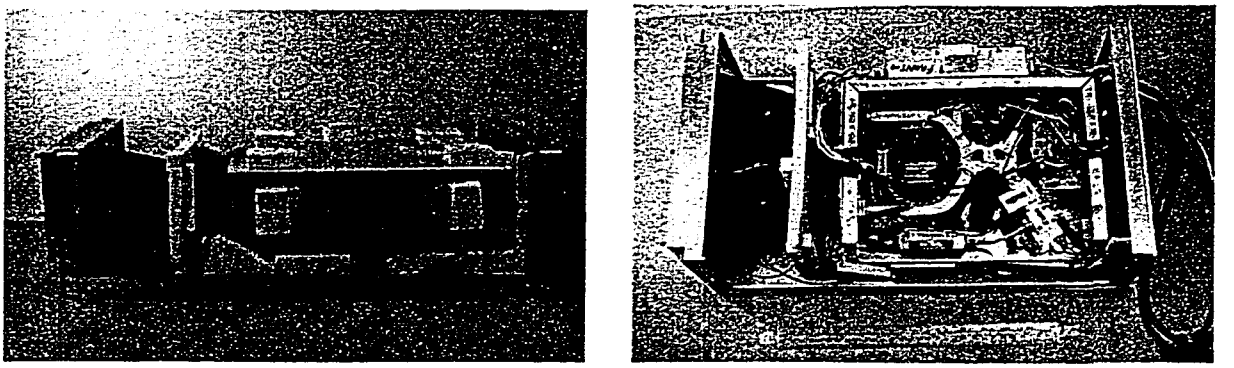

(a) (b)

Figure 2.8: 19 GHz radiometer (a) with outer cover removed (b) with outer and inner covers removed. Antennas are facing left.

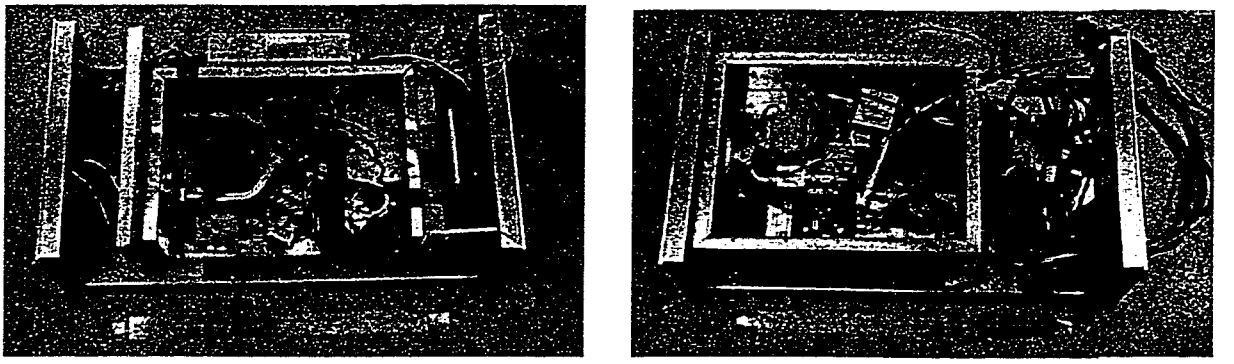

(a) (b)

Figure 2.9: (a) 37 GHz and (b) 85 GHz radiometers with outer and inner covers removed. Antennas are facing left.

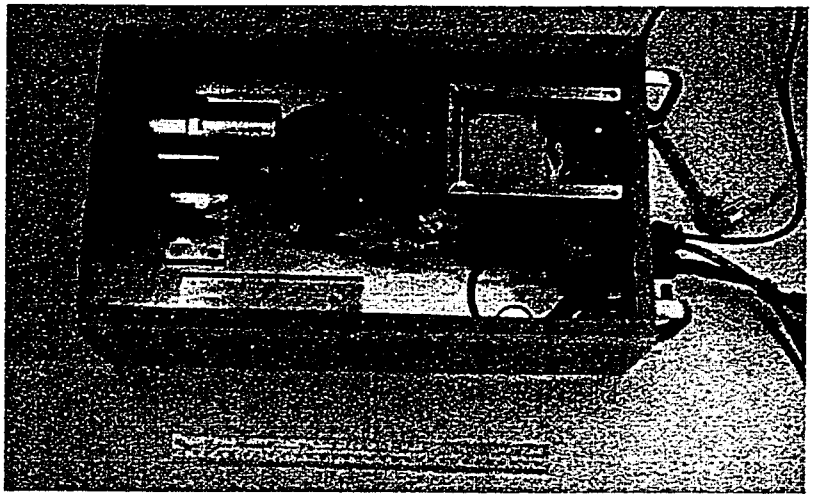

Figure 2.10: Photo of box containing the thermal IR radiometer (upper left) and fiber optic downlink circuitry (right). Video camera (removed) occupied the lower half of the box.

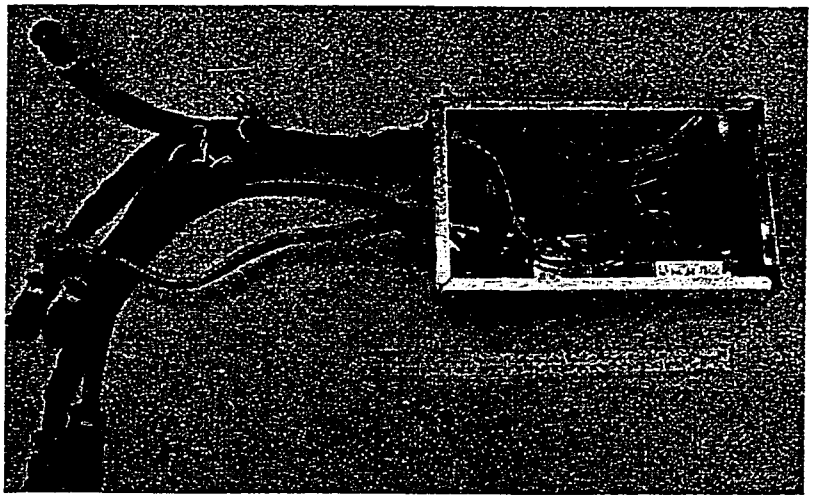

Figure 2.11: The "centerbox" contained power control and optical fiber uplink circuitry for the tower instruments. Cable harnesses distributed power and control signals to each radiometer and included a local data bus between radiometers and the fiber optic downlink to the CDMS trailer.

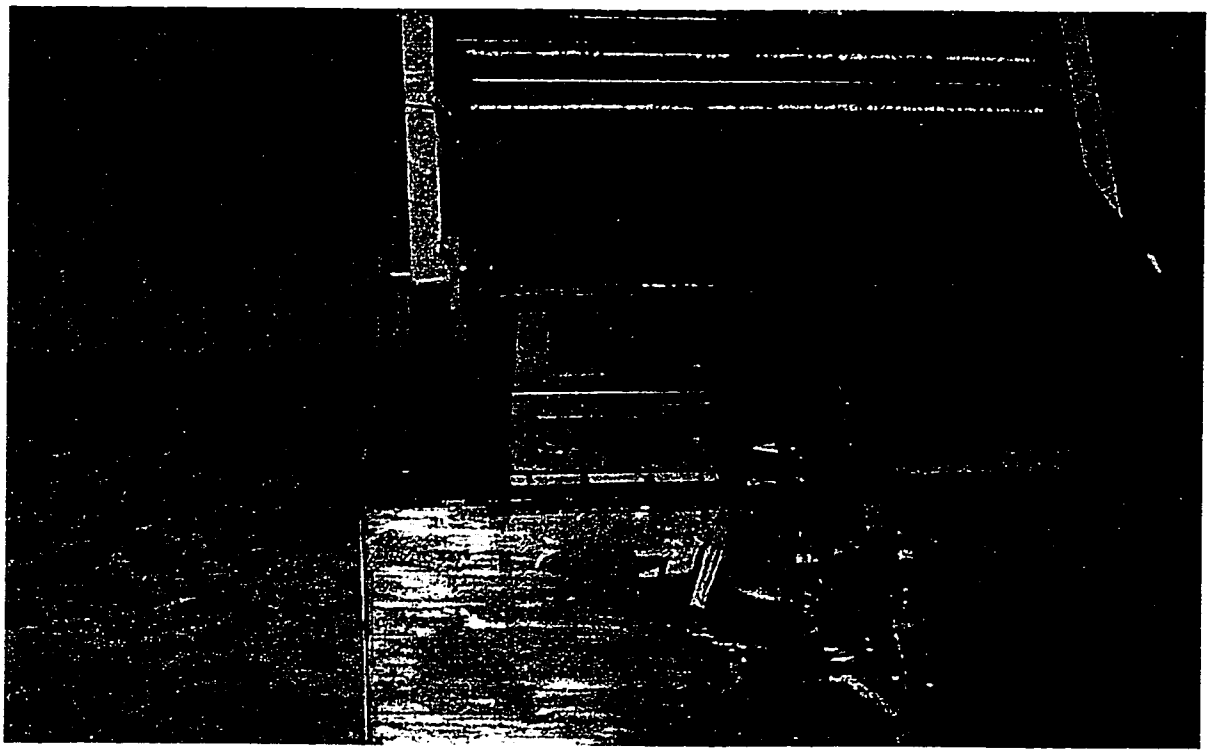

Figure 2.12: Housing closeup photo showing locations and orientations of the microwave and infrared radiometers: 19 GHz radiometer (upper right), 85 GHz radiometer (lower right), 37 GHz radiometer (upper left), and IR radiometer and video camera (lower left). The "centerbox" and door positioner occupied the center bay.

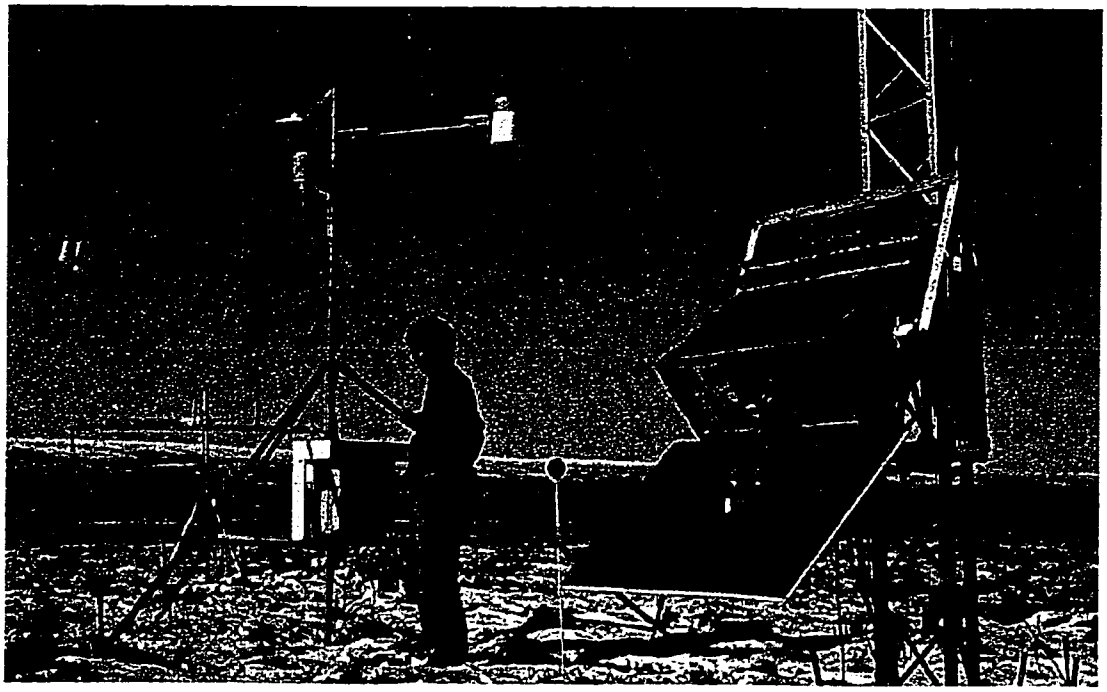

Figure 2.13: Author standing next to micro-meteorological "tripod". The tower housing (foreground) had been lowered for inspection.

- Added: an upwelling pyranometer.
- Added: an aspirator for the net radiometer to reduce wind speed bias variability.

Table 2.3 includes a list of the upgraded MMS instrument complement. The instruments were consolidated on self-supporting tripods for deployment on the spongy uneven tundra (see Fig. 2.13).

In TMRS1, signal conditioning circuitry for the MMS sensors was located in the CDMS trailer since all the sensors were located within 10 m. For deployment 30 m away in TMRS2, I re-designed the sensor signal conditioning circuitry and placed it as close to the sensors as possible—right at the main tripod. In similar fashion to the tower housing signals, I multiplexed the conditioned sensor outputs in order to minimize the number of long cables needed. And, I added a digital serial link for downlink of sensor outputs to the CDMS trailer and uplink of command signals to the MMS. All the MMS circuitry was placed in

an insulated, heated, weatherproof box. For cold start scenarios, a temperature sensor and the heaters were operable from the CDMS trailer even with tripod power turned off.

2.3.2.3 Control and Data Management Subsystem

Changes and improvements to the CDMS were as follows:

- Added: serial link multiplexing for the time domain reflectometer subsystem, infrared radiometer, and MMS instruments.
- Added: control signal multiplexing for the tower and tripod instruments to reduce cabling and improve the accuracy of measurements.
- Added: a variety of software enhancements to accommodate the new sensors and new system configuration as well as to improve robustness (courtesy of J. Galantowicz).
- Added: an uninterruptible power supply (UPS) for the computer and sensitive electronics for protection against short power outages.
- Added: a watchdog timer and computer self-reboot capability to improve robustness.
- Finished insulating the trailer walls and added a second 1500 W electric space heater. Sealed all gaps (door, vent, etc.) against insects and blowing snow.
- Added: a trailer interior temperature sensor for equipment freeze protection.

2.3.3 Deployment

I was primarily interested in collecting field data for the snow-free season of 1995 (May–August). Thus, the subsurface sensors (temperature, soil moisture, soil heat flux) had to be installed the previous year, while the active layer (upper portion of tundra which thaws each year) was sufficiently thawed. In fact, the complete instrument system was deployed in the fall of 1994, and the decision was made to collect data through the arctic winter. The risk was that the system might suffer major or catastrophic damage as a result, and affect

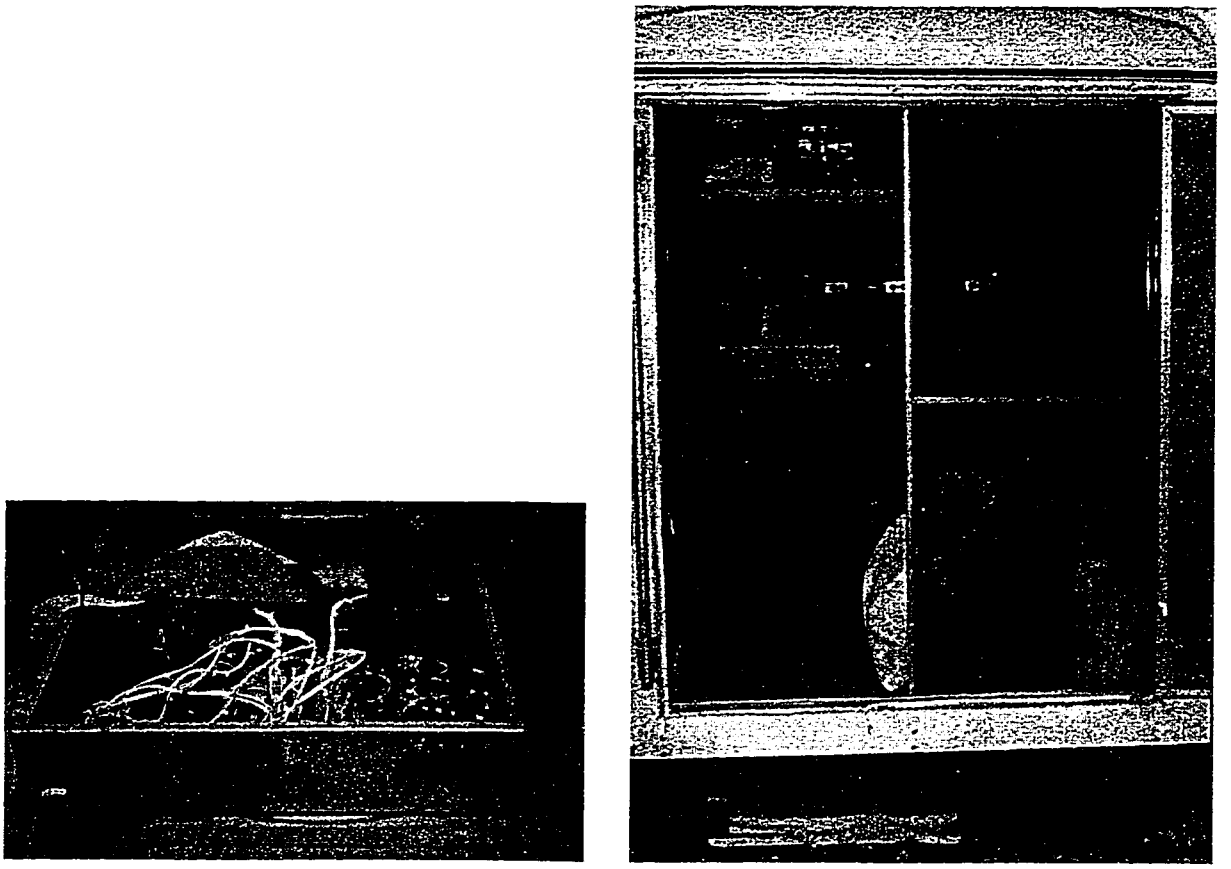

(a) (b)

Figure 2.14: (a) The trailer box was the interface between the CDMS and all TMRS instruments. The 4 thin cables exiting the right front of the box are the plastic optical fiber uplink/downlink to the tower housing. (b) CDMS trailer interior. Insulated walls and two 1500 W heaters kept the internal air temperature above freezing during the winter. Experimental data were saved locally on the computer hard disk for later transfer.

Description	Mfr/Model
MICRO-METEOROLOGICAL INSTRUMENTS:	
10-meter anemometer	Met-One 014A
2-meter anemometer and wind vane	Davis Instruments 7911
2m Air temperature and Relative humidity	Vaisala HMP-35AC
Bowen Ratio (intakes at 1 and 2 m)	Campbell 023
$\downarrow$ shortwave hemispherical flux	Eppley 8-48 (black and white)
$\uparrow$ shortwave hemispherical flux	Eppley 8-48 (black and white)
Net radiometer w/aspirator	REBS Q-6
Rain gage	Texas Electronics 525
Rain gage wind screen	Novalynx Alter-type
TDR Soil moisture (10 probes)	Campbell(Tektronix)
Subsurface temperature (12 probes)	Campbell thermistor 107, 107B
Snowpack temperature (12 probes)	Campbell-equivalent thermistors
Snowpack depth	graduated rod and video camera
Subsurface heat flux (3 disks)	Thornthwaite 610
OTHER INSTRUMENTS	
19 GHz radiometer	custom U. Michigan
37 GHz radiometer	custom U. Michigan
85 GHz radiometer	custom U. Michigan
IR radiometer	Everest Interscience 4000ALCS
Video camera	Panasonic 1410
CDMS COMPONENTS	
Data logger and controller (hardware)	Apple Macintosh, National Instruments
Data logger and controller (software)	custom Hypercard program

Table 2.3: List of TMRS2 Instruments

our ability to collect data during the following snow-free season. Fortunately, TMRS2 survived the winter and collected 8 months of unique data during this climatologically important season. Certain sensitive equipment such as the Bowen ratio instrument and the net radiometer aspiration fan were kept off during the winter without significant scientific impact.

2.3.3.1 Transportation

TMRS2 was transported from Ann Arbor to the REBEX-3 site and back using the project Jeep. The one-way travel time was two weeks. The Jeep also provided local transportation within Alaska throughout the experiment. We arrived at the site on 15 August, 1994 (day 227[1]).

The instruments were deployed on a flat moist acidic tussock tundra area adjacent to an abandoned gravel pad west of the pad used by the DOT camp. This location appeared to have tundra which was most representative of tundra in the area. The CDMS trailer was parked on this empty pad and cables were run across the tundra surface between the trailer and the tower and the MMS instruments (see Fig. 2.15).

2.3.3.2 Electrical Power

Maximum power usage was 7 kW during the winter with all heaters running. Summertime power usage was under 4 kW. The distance between the DOT generators and the TMRS2 equipment was 300 m. At 110 volts, the voltage drop due to ohmic losses was prohibitive for reasonable wire diameters. And, the drop would fluctuate unacceptably as various loads switched on and off. Thus, it was clear that TMRS2 would require a high-voltage connection to the generators. This was accomplished via a 300-meter arctic-grade 440 VAC "extension cord."

The DOT understandably required that a state-licensed electrician perform the installation. I found exactly one state-licensed electrician from Fairbanks who was willing to make

[1]1994 Julian day number. 1 January, 1994 = day 1, 1 January, 1995 = day 366, etc.

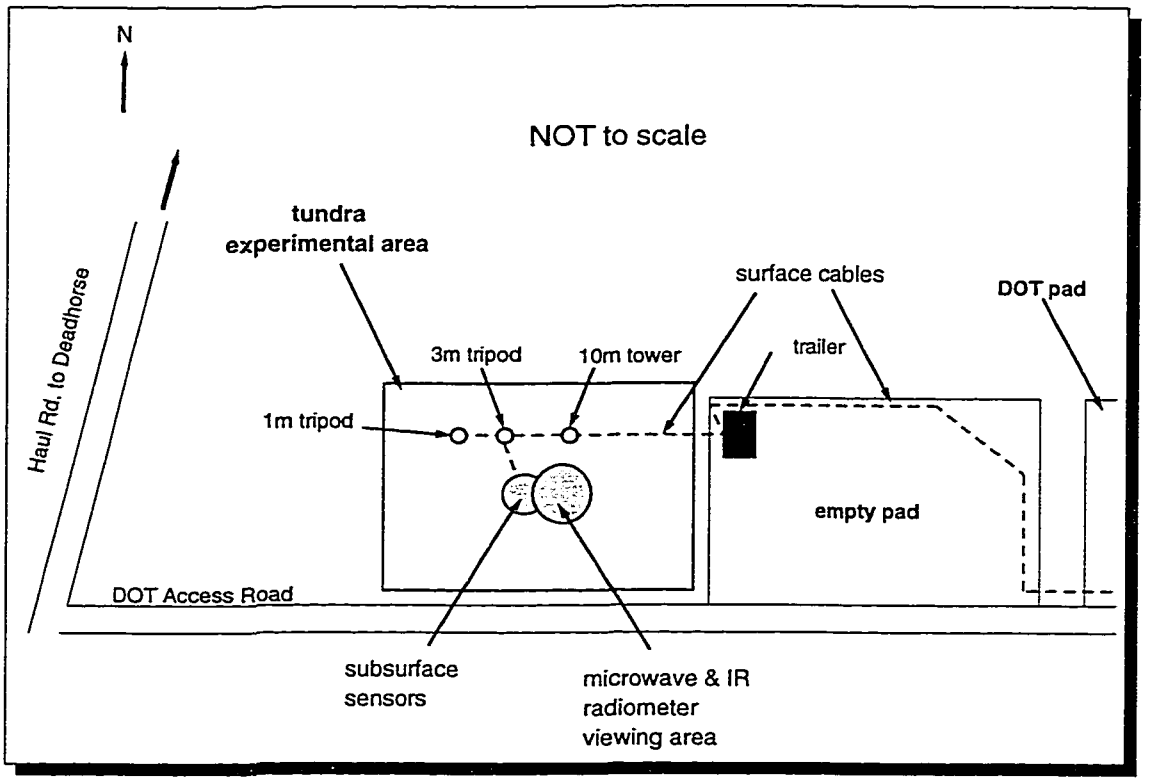

Figure 2.15: Diagram of DOT pad, REBEX-3 ("empty") pad, and roads.

the all-day drive to the REBEX-3 site to connect TMRS2 to the generators. He had to bring all necessary tools, the 300-meter spool of cable, his own food, and a tent. [The first morning on-site, a grizzly bear visited his campsite (without incident).]

I had brought a 10 kVA step-down transformer, which was installed at the TMRS2 end of the extension cord to convert the 440 VAC to two 110 VAC circuits for powering all the TMRS2 equipment. The transformer was sand-encased, rather than oil-filled, so direct exposure to arctic temperatures did not present a problem.

The extension cord had to be buried inside heavy steel conduit across much of the DOT facility to prevent heavy vehicle traffic from crushing the cable. A road grader and liberal student elbow grease were used to dig the burial trench.

2.3.3.3 Communications

The "Timbuktu" software package provided remote control and data transfer capabilities over a standard modem connection back to Ann Arbor. Of course, there were no existing phone *lines* at the REBEX-3 site, although the DOT camp had a radiotelephone. We rented our own VHF radiotelephone from the state-wide "local" service provider, Alascom, for $1000 a month. There were no economical alternatives. The REBEX-3 site was just at the edge of geosynchronous satellite telephone coverage (Inmarsat). However, a large dish antenna would have been required for a reliable link, and air time was extremely expensive. Only one of the various multi-satellite global communication systems was even partially operational at the time (Orbcomm), and all-day coverage was not available.

The radiotelephone was a major weak point in the remote control link. The connection was usually poor, with effective data rates of 300 baud or less, and "Timbuktu" had only a graphical user interface. At those slow speeds, redrawing the computer screen display sometimes took many minutes. Latency-induced errors were a constant problem (e.g., clicking on a button which didn't exist). Very quickly, we had to improvise a workaround using the TMRS2 control program's (i.e., Hypercard's) text interface—the only one available on the TMRS2 Macintosh.

Part of the reason for the poor telephone connection was the tortuous connection path–again, the only option for our situation. With an external Yagi antenna (Fig. 2.16), we were connected to the terrestrial microwave relay network operating along the Trans-Alaska oil pipeline. In Prudhoe Bay, that network connected us via optical fiber *right back down the pipeline route, right past the REBEX-3 site* to Anchorage. From Anchorage, all circuits went via geosynchronous satellite to the Outside.

2.3.4 Data Collection, Problems, and Fixes

The instrument system was fully deployed and operating by mid-September, 1994. Measured quantities included ground and sky microwave brightnesses at the SSM/I frequencies

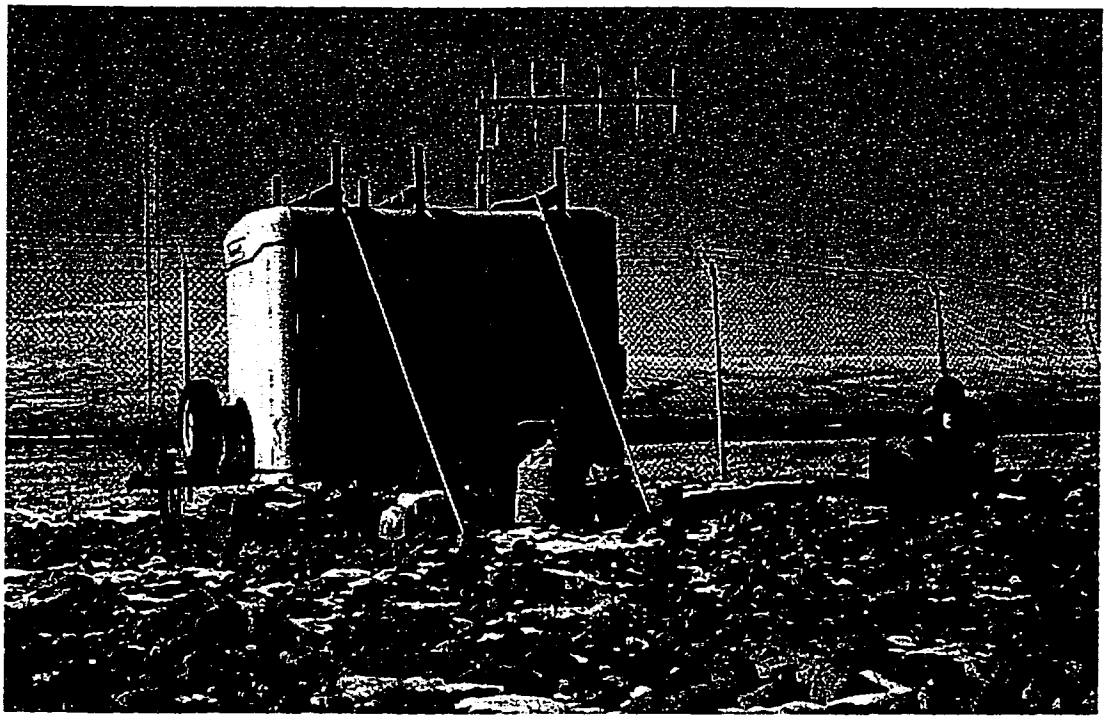

Figure 2.16: Radiotelephone antenna next to TMRS trailer.

of 19.35 and 37.0 GHz (horizontal and vertical polarizations) and 85.5 GHz (vertical polarization), thermal infrared ground brightnesses, net radiation, upwelling and downwelling solar radiation, Bowen ratio, soil moisture and soil temperature profiles, soil heat flow, air temperature, relative humidity, wind speed and direction, liquid precipitation, snow depth, and snow temperature profile.

2.3.4.1 Winter Operation

Fig. 2.18 shows winter conditions at the site.

The only significant problems encountered between October, 1994 and April, 1995 were a broken power supply in the MMS, a sometimes balky positioner for the radiometer sky reflector, and waveguide in the 37 GHz radiometer which shook loose in the spring. The power supply was replaced during a brief site visit in January, 1995, and MMS function was restored. The bad data associated with the other problems was eliminated, and the waveguide was reattached in April, 1995. The restored 37 GHz radiometer operated successfully

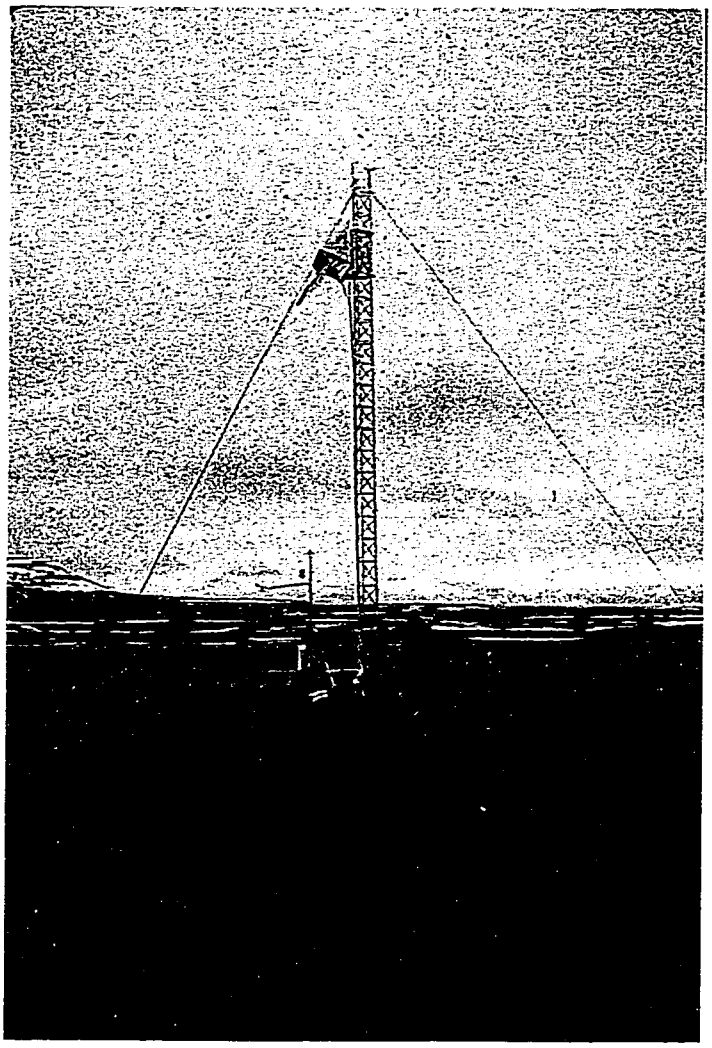

Figure 2.17: Snow-free conditions, May, 1995. Note lumpy tussocks. The microwave and IR radiometers view the ground at the SSM/I viewing angle: 53° up from nadir.

Figure 2.18: Snow-covered conditions, January, 1995. From left to right: 1-meter tripod with net radiometer and upwelling pyranometer; 3-meter MMS tripod; 10-meter tower; CDMS trailer and communications antenna (extreme right). See also Fig. 2.15.

for the remainder of the experiment.

2.3.4.2 Remote Operation

The utility and economy of the telephone remote control and data transfer capabilities for an experiment such as REBEX-3 cannot be understated. Only three site visits by experiment personnel were required aside from the initial deployment and retrieval trips during the entire REBEX-3 year (Table A.1). TMRS2 could have been entirely re-programmed over this link, if it had been necessary. In many respects, TMRS2 was operated in a manner similar to a operating a satellite.

Special procedures were implemented to prevent serious equipment damage or failure in the event of power failure, especially when outside temperatures were at or below freezing. Some of the procedures were less than optimal. However, the expense, delay, and difficulty associated with making on-site repairs was worth the tradeoff.

Cold Start Precautions and Procedures Electrical power from the DOT generators was subject to interruptions which lasted anywhere from seconds to hours. The UPS provided 10 minutes of continuity for critical items (computer, low-power or supply-sensitive instruments). High-power loads (primarily the heaters), however, were not connected to the UPS and would drop out, affecting radiometer temperature control among other things. During a sufficiently long outage, the MMS and the tower electronic circuitry would cool down to the outside air temperature. Restarting these circuits at sub-freezing temperatures was potentially catastrophic, so the control software first checked the temperature of the circuits using temperature sensors I installed for this purpose. If the temperature was too low for a safe turn-on, system heaters were used to raise the temperature to a point above freezing before the circuits were re-activated. To execute this cold-start protocol, the cold-start temperature sensors and heaters throughout TMRS2 were designed to be operable with only CDMS power turned on (the trailer interior remained above 10° C throughout the winter).

Watchdog Timer and Telephone Restart For reasons never fully understood, the control software would occasionally "lock up," halting active temperature control, stopping data recording, etc. This problem was independent of power interruptions, and would often occur during TDR soil moisture measurements. The solution was to reboot the computer. However, the only way to do this while the computer was halted was to manually press a reboot switch mounted on the computer case. An automatic reboot method was added in the field by wiring a relay in parallel with this switch and connecting the relay to a watchdog timer circuit. If the control software were executing normally, a command would reset this watchdog timer every minute. If the control software halted, the timer would expire and trigger a reboot via the relay. The timeout period was set at a compromise value of 2.5 hours. Power outages were often actually groups of outages several minutes apart over a period of up to 1.5 hours, and I did not want a short timeout such that the computer would be repeatedly rebooted under those conditions. On the other hand, a long timeout period would have meant a longer period during which the radiometers were not being temperature controlled, and during which observations were not being made.

When AC power was lost and the UPS had run out of battery power, the computer would shut down. When AC power was restored, the Macintosh computer would remain off. To remotely restart the computer, a commercially-available device (originally used with TMRS1) was installed which would re-start the computer under these circumstances when the telephone rang. If the computer was on and the control software was running normally, the modem would answer any telephone call. If the modem did not answer, the computer was either off or in the middle of a watchdog reboot. Throughout the yearlong experiment, I checked the status of TMRS2 usually once or twice a day by telephone, from wherever I happened to be. A more automatic restart procedure would have been nice, but I found that it was prudent to do more than just check if the system was on or off. I usually checked system status as well as the data values being recorded in order to detect more subtle problems.

2.3.4.3 Subsurface Temperature and Moisture

Subsurface temperature was measured with thermistors embedded in one "typical" tussock at the edge of the radiometer footprint area (see Fig. 2.19). One thermistor each was installed at depths of 30 and 40 cm. Pairs of thermistors were installed with 15 cm horizontal separation at depths of 5, 10, 15, and 20 cm. A final pair was installed at 1 cm depth, located on the north and south-facing sides of the tussock, 20 cm apart. All depths were with respect to the top of the tussock.

The TDR soil moisture subsystem was used for the first time during REBEX-3. Each TDR probe consisted of a pair of 30-cm long parallel metal rods, inserted horizontally into the soil 5 cm apart at depths of 2, 5, 10, 15, 20, 35, and 39 cm. All depths were with respect to the top of the tussock. A 10 m cable connected each probe to a multiplexer placed near the MMS tripod. A 50 m coaxial cable connected the multiplexer to the TDR instrument (a Tektronix cable tester) in the CDMS trailer. The cable tester sent pulses to a probe and displayed reflected energy (normalized reflected voltage) as a function of elapsed time. The time required for the pulse to travel the length of the probe is proportional to the square root of the apparent dielectric constant, assuming losses in the soil are small. [Investigators have found that typical soil losses do not significantly affect travel time [17, 16].] Provided the features corresponding to the beginning and the end of the probe can be identified in the resulting trace, volumetric soil moisture can be computed from a calibration curve.

Every 6 hours during the snow-free season, the control computer would make TDR measurements just after the normal TMRS2 measurement cycles at 0000, 0600, 1200, and 1800 Alaska Standard Time. One trace from each probe was recorded for later interpretation. Due to CDMS-TDR interface problems, ten TDR measurements would take up to an hour to complete. The problems would often cause the TMRS2 control computer to hang (and eventually reboot). As a result, 25% of the measurements were never made. The connection to probe 1 (at 39 cm) broke early in the experiment, so no data from that depth were usable.

There were problems with nearly every aspect of the TDR soil moisture measurements. The range of reflected signal amplitudes and elapsed times covered an order of magnitude, and *a priori* the chart display scale had to be set to span the entire possible range. As a result, the resolution of many of the TDR traces was poor, and it was difficult to determine the features corresponding to the beginning and the end of each probe. The probe configuration also made this determination difficult.

The calibration curve for organic soils, reported by Topp [89], was derived for a sample with a uniform density of 0.422 g/cm^3. It is not valid for apparent dielectric constants below 1.7. But tundra peat is mostly air voids near the surface—porosities of 90% are common [35]. My measurements included dry bulk densities as low as 0.02 g/cm^3 in the uppermost 3 cm. As suggested by Stein and Kane [84], this high porosity was likely to make the Topp curve inaccurate for TDR measurements of tundra peat.

The large size of the probes and their effective sampling volume (a radius of a few cm around the probes) compared to the size of the tussock made the depth resolution mediocre. The rapid vertical variation of peat porosity and density also made the interpretation of any results uncertain.

For these reasons, I decided that for the present REBEX-3 study, analyzing the TDR measurements was a low priority. Based on the work of Liou [52] and my own earlier work [45], I felt that at the SSM/I frequencies, the data for the tundra thermal regime were much more important in the modeling context.

2.3.4.4 Surface Energy Balance

MMS Radiation Instruments These included two identical pyranometers measuring downwelling and upwelling hemispherical solar (shortwave) radiation ($R_S \downarrow$, $R_S \uparrow$), plus a net radiometer to measure net shortwave and longwave hemispherical radiation ($R_N = R_S \downarrow - R_S \uparrow + R_{LW} \downarrow - R_{LW} \uparrow$). The upwelling pyranometer was installed on day 489 (4 May, 1995), at the beginning of the snow-free season. In past REBEXs, the radiation instruments

were mounted on individual poles or on arms pointing south to eliminate shadowing by any supporting structures. Above the arctic circle during the summer, the solar azimuthal angle ranges a full 360°, so the net radiometer and the upwelling pyranometer were placed on their own small (1 meter) tripod, several meters away from the other MMS instruments to minimize any shadowing (see Fig. 2.19). The downwelling pyranometer was simply mounted at the top of the main MMS tripod, and the tripod located west of the 10 m tower (i.e., *not* north), where only the tower might cause brief shadowing.

Since TMRS2 was not constrained by battery power, I was able to operate a continuous aspirator (blower) for the net radiometer beginning on day 500 (15 May, 1995). This consisted of a small fan which forced air into a 3.8 cm-diameter tube. The tube was mounted around and concentric with the net radiometer horizontal support arm, with the output end of this tube located a few cm from the net radiometer domes. The aspirator guaranteed a minimum wind speed over the domes of 2.2 m/s, effectively removing the variation in R_N due to wind speed. A +5% wind speed correction was then all that was required for the R_N data [76].

On day 588 (11 August, 1995), the plastic domes of the net radiometer cracked from exposure to the elements and/or bird pecking. Data after day 588.77 were unusable. That was 3 months into the snow-free season, so the impact on the overall experiment was minimal.

Road dust was not apparent on the domes of the MMS radiation instruments during any of the site visits, and I do not believe dust had a significant effect on the data. Nevertheless, the domes were cleaned in September and October, 1994 and in April/May, 1995. REBEX-3 $R_S \downarrow$ data and $R_S \downarrow$ data from the LTER site 1.5 km to the east (far enough from the road that dust could not be an issue) matched so well, that they could be used to patch each other's gaps without adjustments.

Air Temperature, Relative Humidity, Soil Heat Flux These instruments functioned without problems throughout REBEX-3. The three identical soil heat flux discs were placed

in different parts of the same tussock as the soil temperature probes. One disc each was installed at 2 cm depth in the north- and south-facing sides of the tussock. The third disc was installed at 5 cm depth at the center of the tussock. I believe differences in the measured heat fluxes are partially due to the difficulty in obtaining consistent thermal contact with the high-porosity peat, especially at 2 cm. The contact may also have been poor. REBEX-3 flux values are low by 0–100% in comparison to values measured by other researchers using different sensors at other North Slope sites [55].

Fetch Undisturbed airflow from upwind of the micrometeorological instruments was important for obtaining measurements which were representative of the local area. The vertical structure of the airflow influences the air temperature and humidity profiles. It also indirectly affects the entire surface energy balance through its influence on latent and sensible heat fluxes. Ideally, there would be no obstacles to wind flow in the vicinity of the instruments—i.e., an infinite fetch in all directions. In practice, there were several. These included the TMRS2 tower and support trailer, the gravel pad upon which the trailer was parked, the DOT buildings, the DOT access road, and the Pipeline Road ("Haul" Road). The exact location and orientation of each TMRS2 instrument was chosen to minimize the effects of instruments on each other, and to maximize the fetch in the most important directions.

I had learned, prior to deployment, that the prevailing winds at the REBEX-3 site are north-south. Because the gravel pads were to the immediate east, airflow from that direction would be most disturbed. The fetch was several km toward the north, 0.2 km to the west, over 100 m to the south, and 30 m to the east. Thus, the 2-m wind sensors and the Bowen ratio thermocouples and dewpoint air intakes were installed facing generally west so that the MMS tripod would disrupt airflow only from the east, the already-disturbed direction.

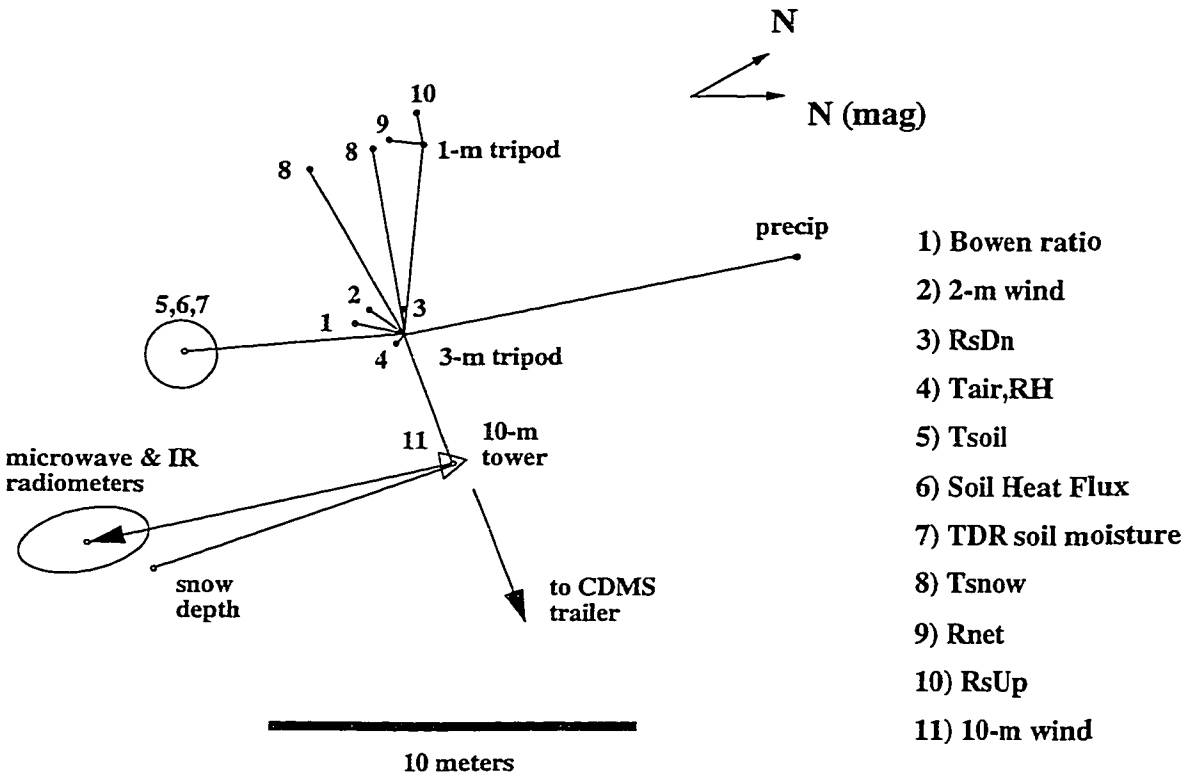

Figure 2.19: Plan view of REBEX-3 instrument locations.

Bowen Ratio Subsystem The new Bowen ratio subsystem experienced one major problem during REBEX-3: seals in the upper air intake arm leaked early in the snow-free season. The liquid water which entered that arm corrupted all further dewpoint readings for that arm, and therefore made it impossible to obtain measured latent and sensible heat fluxes for the remainder of the experiment. Fortunately, Bowen ratio is not a model *input* variable, so the failure was not fatal. The Bowen instrument fielded during REBEX-3 was the earliest version sold by Campbell Scientific. After REBEX-3, they upgraded the rubber seals in this product—so apparently, this was a design flaw of this instrument.

Precipitation Gage An Alter-type wind screen was added in April, 1995 to increase the accuracy of the "catch." The gage was also moved 10 m away from other instruments to reduce potential mutual airflow disturbances. The addition of a new debouncing circuit on day 490 (5 May, 1995) eliminated occasional spurious rain gage counts. This was prior to any liquid precipitation at the site.

For wind and animal resistance, all tripod legs were anchored to steel rods driven into the permafrost.

2.3.4.5 Snowpack

Although the primary goal of REBEX-3 was to collect data during the snow-free season, some snow-related measurements were made for possible future research. These are described briefly here for completeness.

Temperature Profile Snowpack temperature profiles were measured with two vertical thermistor stacks. Each stack had 6 thermistors spaced 10 cm apart. The bottom thermistor of one stack was flush with the tundra surface in an inter-tussock valley. The bottom thermistor of the other stack was flush with the top of a tussock. The vertical offset between the stacks was 10 cm. The thermistors were attached to nylon cable ties protruding 10 cm horizontally from a support pole in order to reduce the effect of the support pole on natural

snowpack conditions throughout the winter. The connection to probe 7 (bottom probe in the inter-tussock valley) broke, but the other probes worked fine.

Depth The snowpack depth gage was a wooden pole inserted into the tundra. The pole was marked with 5-cm wide alternating light and dark bands. The depth was estimated from once-per-day images taken by the tower video camera.

Video Images Although qualitative, these were found during previous REBEXs to help with assessments of site conditions. New snow, snowpack compaction during melt, snow and tundra surface conditions, and clear vs. overcast conditions (from the sharpness of shadows) could be identified from the images.

Stratigraphy On 31 March, 1995, a snow research team from the U.S. Army Corp of Engineers Cold Regions Research And Engineering Laboratory (CRREL) dug a snow trench 100 m north of the REBEX-3 site, and recorded the snowpack stratigraphy [86] for possible future research relating the snowpack conditions to the microwave signatures observed by TMRS2.

2.3.4.6 Infrared and Microwave Emission

Infrared Radiometer The IR radiometer was installed in October, 1994. The internal digital circuitry became intermittent during the winter. It was removed, repaired, and re-installed during the April/May, 1995 site visit. This instrument also experienced problems communicating with the CDMS, but it functioned correctly for 248 out of 332 days between October, 1994 and September, 1995. Most importantly, it provided continuous data from mid-May through the end of REBEX-3 except for a week in late July and 3 days in August.

Microwave Radiometers Overall, the microwave radiometers performed well during REBEX-3, proving to be highly consistent throughout the year as will be described later.

This is particularly impressive considering that they were the most complex TMRS2 instruments exposed to the elements.

Maintaining proper temperature control was the crucial radiometer-related chore for the CDMS. Door positioning problems made this difficult but not impossible during cold weather. The constant temperature (i.e., "thermostat") setting, T_{SET} for each radiometer was adjusted remotely over the course of the experiment, ranging from 318 K during the winter to 330 K during the summer. Since only active heating was used to effect temperature control, the T_{SET} values had to remain above the radiometer temperature due to quiescent power dissipation from the internal components alone.

Power interruptions and computer halts were the main causes of temperature control disruptions. The longer the interruptions, the longer the time required to recover control—anywhere from 2 minutes to 1.5 hours once power and control resumed.

The 85 GHz radiometer temperature control was intermittent until a bad wiring connection was replaced on day 483 (28 April, 1995). Even with temperature control working, the 85 GHz radiometer exhibited larger fluctuations of the waveguide reference load temperature vs. the 19 and 37 GHz radiometers. I attribute this to three differences associated with the 85 GHz unit: (1) there was insufficient room to install an antenna heater, (2) the thermal path from the antenna aperture to the waveguide load was much more direct than in the other radiometers, and (3) the cutout for the antenna at the front of the radiometer was oversize for the single 85 GHz horn, having originally been designed to accommodate a second horn. Mylar film covered and sealed these cutouts to at least prevent air and water, snow, ice, or insects from directly entering the radiometers.

As mentioned earlier, the antenna waveguide connections were shaken loose inside the 37 GHz radiometer. Bad data from day 435 until the radiometer was repaired on day 472 were deleted. This problem apparently had a significant effect on the system (self) noise of the 37 GHz channels, T_{REC}. In an ideal noise-free radiometer, $T_{REC} = 0$. At the start of REBEX-3 in September, 1994, T_{REC} was 802 K for the H-pol channel and 857 K for the

V-pol channel. After the repair, these had increased to 1265 K and 1277 K, respectively. In comparison, the 19 GHz T_{REC} values were 819 K and 809 K in September, 1994 and 827 K and 793 K in May, 1995, respectively. And, the 85 GHz T_{REC} was 2788 K in September, 1994 and 2918 K in May, 1995.

Door positioning problems All the tower housing instruments depended on proper operation of the housing door, which proved to be a balky mechanism—particularly during the winter. The normal position sequence was: start closed; open partially to make a sky observation at a zenith angle of ~30–35°; open a bit more to make a second sky observation at 53°(corresponding to sky brightness which may be specularly reflected at the SSM/I view angle); open fully to make a ground observation; close until next cycle. At each door position, observations at all 5 microwave channels plus an IR observation were recorded. So, for each measurement cycle, three observations were recorded per channel: $T_{B1}, T_{B2}, \text{and} T_{B3}$.

If the door were stuck in the closed position, observations were of the housing interior instead of ground and sky. If the door were stuck in the fully open position, observations of the ground could be made, but during the winter, the housing interior was exposed to the ambient cold temperatures and wind, making radiometer temperature control more difficult. And, of course, observations of sky brightness were not possible. If the door were stuck in an intermediate position, observations of both ground and sky brightnesses were affected.

Initially, positioning worked fine, and an integral sensor in the motorized door actuator gave accurate position readings. By the time of snowmelt, the integral sensor had stopped working, and sky observation angles were no longer directly measured with any accuracy. The positioner became less balky, and I rewrote the door control software to operate by turning on the door positioner for fixed lengths of time. The intermediate sky observation angles were approximate, and not measurable by TMRS2. On the other hand, the ground

observation (fully open) position and the fully closed position were reliably achieved by simply running the positioner for enough time to ensure that the mechanism reached its end-of-travel. This was the best option available at the time, and allowed TMRS2 to collect ground observations for the remainder of REBEX-3, including the critical snow-free season. However, the door would sometimes malfunction and the control software would not be synchronized with the actual door position, with the result that the positioning sequence would be out of order. Observations of the ground were the most critical data to measure, and fortunately, the door behavior was such that the overwhelming majority of ground observations were correctly made.

The geometry of the tower housing, the size of the door, and the radiometer viewing geometry were such that only a limited range of sky observations angles were realistically available (~30–55°). If the door was open too far, the ground was partially visible. If the door was not open far enough, the field of view included parts of the housing which also would bias the observations. The lack of accurate door angle information during the snow-free season meant that the sky observation data from that period were not quantitatively useful. Any impact on the comparison of *ground* brightness vs. SSM/I brightness was minimized since both TMRS2 and SSM/I observations included sky brightness reflected off the ground. The impact on the comparison of TMRS2 vs. model predicted brightness was minimized during the snow-free season since the tundra exhibited a low reflectivity of ~0.04 and downwelling sky brightness was under 30 K for the 19 and 37 GHz channels. So, the contribution to the total observed brightness is predictable and was less than $30 \times 0.04 = 1.2$ K. (The sky brightness was calculated based on surface air temperature and humidity conditions in order to examine the importance of atmospheric corrections on the SSM/I comparison in Chapter 4.)

2.3.4.7 Soil and Vegetation Samples

Soil and vegetation samples were collected on 12 and 13 September, 1994. This was just prior to winter snowpack accumulation. At the time the samples were taken, the upper few cm of tundra were frozen but snow was not present. The fibrous nature of the peat made it very difficult to obtain a useful soil sample. The standard soil corer used in previous REBEXs was completely useless. It did not cut through the peat and pushing the corer simply compacted the peat.

On September 12, an incision about 30 cm long and 10 cm deep was made in a typical tussock just east of the radiometer footprint using a knife. A well-defined incision was difficult to make, and controlled-volume samples of the peat were practically impossible to obtain with the knife. Compaction resulted while cutting both horizontally and vertically.

On September 13, samples were successfully obtained using a power drill equipped with a hole saw type of bit. The inner diameter of the hole saw was 4.8 cm, and the inner length was set at 3.0 cm by inserting a styrofoam spacer. The resulting core volume was 54.3 cubic cm. Reasonably accurate sample volumes of peat and vegetation were taken from four locations along the tussock: the top (T), bottom or inter-tussock valley (B), and on the north (N) and south (S) facing sides. The zero-cm reference height was chosen according to the method used by Hinzman and Kane ([34])—the depth of the bottom of one's hand pressing lightly on the tussock.

It should be noted that as soon as a core of peat was extracted from the tussock, water would drain out of the core. And, water from the surrounding walls of the hole would seep into the hole. [The same "flooding" problem was encountered while installing the subsurface temperature and TDR moisture probes. It was quite clear that accurate moisture or hydraulic measurements of moist or wet tundra must be made in-situ. And that subsurface probe installation must be done very carefully to avoid altering the characteristics of the natural soil profile.] Thus, moisture contents and quantities derived from moisture

values determined from these samples are to be used with great caution or not at all. And, the September 13 samples are primarily useful for estimating the soil dry bulk density profile, which depends only on dry masses and volumes.

Each core was placed in a paper cup and weighed ("wet" mass in Table 2.4). Later, the cores were baked at 100° C for 18 hours and re-weighed ("dry18" column). After 37 hours, the weights were checked again ("dry37" column). Only minor changes were observed between the 18- and 37-hour readings, so the 18-hour values were selected as the dry mass values. The dry bulk density profile from the "Top" samples was used for the tundra land surface process modeling described in Chapter 3. The factor of 0.9977 was a calibration correction factor for the balance used to weigh the samples.

More detailed soil composition data for modeling purposes (texture, porosity, bulk density, etc.) were obtained from Michaelson and Ping [61] and Hinzman and Kane [35]. These are described in Chapter 3.

2.4 Instrument Calibration

2.4.1 MMS Instruments

Unlike the microwave radiometers, the MMS instruments and the IR radiometer were factory-calibrated. However, extreme temperatures and long periods in the field might have affected instrument accuracy. So, I checked these instruments at the end of REBEX-3. The purpose was more to make corrections if large deviations were found rather than to fine tune every single sensor and probe. Many of the instruments (e.g., the net radiometer) could not be calibrated in the field, in any case.

The air temperature/humidity sensor and 10-m anemometer were factory re-calibrated after REBEX-3 with no significant changes found. The damaged net radiometer was upgraded after REBEX-3, so a post-experiment calibration was not available. The IR radiometer and the upwelling pyranometer had been factory calibrated in April, 1995, so re-calibration was deemed not necessary. The downwelling pyranometer was re-calibrated

sample ID	tare	wet*	dry18	dry37	wet-tare	h20*	bulk den	Mvol#	Mg_wet#	Mg_dry#
	(g)	(g+tare)	(g+tare)	(g+tare)	* (g)	(g)	(g/cc)	(%)	(%)	(%)
N_veg	7.34	12.15	7.9	7.96	4.80	4.24	0.010	0.078	0.884	7.555
N_0-3	7.31	31.19	10.21	10.37	23.83	20.93	0.053	0.385	0.879	7.201
N_3-6	7.39	26.63	9.96	9.95	19.20	16.63	0.047	0.306	0.866	6.457
S_veg	7.22	12.39	9.34	9.39	5.16	3.04	0.039	0.056	0.590	1.432
S_0-3	7.28	15.53	8.63	8.67	8.23	6.88	0.025	0.127	0.836	5.088
S_3-6	7.36	32.36	11.46	11.41	24.94	20.85	0.075	0.384	0.836	5.074
B_veg	7.33	9.44	7.48	7.52	2.11	1.96	0.003	0.036	0.929	13.007
B_0-3	7.33	21.63	8.43	8.38	14.27	13.17	0.020	0.243	0.923	11.945
B_3-6	7.31	24.19	9.16	9.23	16.84	15.00	0.034	0.276	0.890	8.087
T_veg	7.27	11.35	9.13	9.29	4.07	2.21	0.034	0.041	0.544	1.188
T_0-3	7.38	25.66	10.66	10.7	18.24	14.97	0.060	0.276	0.821	4.552
T_3-6	7.4	27.75	10.81	10.94	20.30	16.90	0.063	0.311	0.832	4.945
T_6-9	7.42	30.72	11.36	11.39	23.25	19.32	0.072	0.356	0.831	4.891
T_9-12	7.37	42.4	14.03	14.07	34.95	28.31	0.122	0.521	0.810	4.240
T_12-15	7.35	78.69	29.8	29.86	71.18	48.78	0.412	0.898	0.685	2.168
corer volume:	54.3	cm3		*under	estimate					
use dry18 #s				#derived	under	estimate				
wt. correction	0.9977									

Table 2.4: Soil and vegetation sample data from 13 September, 1994. "Mvol#" = moisture on a volume basis; "Mg_wet#" = moisture on a wet mass basis; "Mg_dry#" = moisture on a dry mass basis.

after REBEX-3, but the vendor had switched to a new standard and advised that a change in calibration constant might not reflect a true change in instrument sensitivity. The newer calibration factor was 6.4% more sensitive than the older calibration factor. Side-by-side comparison verified that the downwelling pyranometer reading was higher than the upwelling pyranometer reading by an amount consistent with this difference. Both read zero to within the accuracy specification in darkness. So, a reduction of 6.4% was made in the downwelling pyranometer data.

The snow and soil temperature probes were calibrated using an ice water bath at 0° C. The soil probes had an average warm bias of 0.43° C, and the snow probes had an average warm bias of 0.2° C. Corrections were made in the data.

Other sensors did not require recalibration or were not recalibrated. MMS instrument accuracies are listed in Table 2.5.

2.4.2 Microwave Radiometers

Radiometer Calibration Strategy

Consistency, precision, and accuracy are key performance measures for all microwave radiometers. This was even more important for a long-duration experiment such as REBEX-3. For a ground-based system such as TMRS2, integration times of 1 s are practical and deliver better-than-0.1 K precision without much difficulty. Accuracy, of course, depended on calibration, and consistency between calibrations depended on instrument stability. The TMRS2 radiometers had to operate for months between calibrations under wide-ranging conditions. Components would drift, age, be shaken, be subject to extreme temperature cycling (up to 100 K) during power outages, etc. Gains, offsets, mismatches, and operating temperatures would all change throughout the experiment. I needed a practical strategy for detecting and adjusting for such changes in a remotely-operated instrument:

1. **Design for stability.** I used a receiver with no RF amplifier. By doing so, gain variations $\Delta G/G$ can be reduced below 10^{-4} [92]. I used individual supply voltage

variables	accuracy	range
Bowen ΔT	[a] $\pm$0.006 °C resolution	$\pm$2 °C [b]
Bowen dewpoints	$\pm$0.5 °C 0.05 °C repeatability $\pm$0.003 °C resolution	-41 to 41 °C dewpoint [b] for -30 to +70 °C ambient 10–90% equiv. RH@26 °C
soil heat flux	[a]	$\pm$160 W/m^2 [b]
precipitation	$\pm$1.0%	0–5.1 cm/hr (0–50 °C)
relative humidity	$\pm$2% (over 0–90%) $\pm$3% (over 90–100%)	0–100% (-20 to +60 °C)
net radiation	$\pm$5% of full scale	-340 to +1020 W/m^2
shortwave radiation $R_S\downarrow$, $R_S\uparrow$ [a]	$\pm$1.0% linearity $\pm$1.5% temp. depend.	0–1400 W/m^2 (-20 to +40 °C)
snow depth	$\pm$4 cm	0–80 cm
shortwave albedo (calculated)	varies	0–1.0
air temperature	$\pm$0.4 °C [d]	-33 to 48 °C
soil temperature	$\pm$0.4 °C [d]	-33 to 48 °C
snowpack temperature	$\pm$0.4 °C [d]	-33 to 48 °C
10-m wind speed	$\pm$1.5% or 0.11 m/s (-50 to +70 °C)	0–45 m/s 0.447 m/s threshold
2-m wind speed	[a]	1.4–52 m/s
2-m wind direction	10° [a,c]	0–360° CW from N
sky reflector view angle	varies	-74 to +148° from zenith
TDR soil moisture	tbd	0–100% vol. fraction
IR skin temperature	$\pm$0.5 °C	-30 to +100 °C
time (AST,LST,UTC)	1 minute	

Table 2.5: Data accuracies. [a] no manufacturer's specification given; [b] intentionally limited; [c] estimate; [d] worst case: sensor interchangeability + bridge tolerance + polynomial Resistance→Temperature conversion accuracy; majority contribution = $\pm$ 0.2 K interchangeability

regulators for active components, for mutual isolation. Cascaded pre-regulation provided additional stability as well as reduced internal heat dissipation. I made sure the temperature-sensitive components were inside temperature-controlled portions of the radiometers. Antenna heaters helped reduce sensitivity to outside air temperature variations. The entire receiver chain was located inside each radiometer box, and output signals were digitized internally.

2. **Use of an internal reference to compensate for gain variations.** In lieu of frequent external calibrations, internal calibration sources can provide a means to calibrate everything downstream of the antenna. Two different source temperatures would be needed to perform an absolute calibration. For best accuracy, the two temperatures would be far apart and span the measurement range (e.g., 10–330 K). A simple passive waveguide load provided a robust, highly accurate, and repeatable hot source temperature. A simple, robust, accurate, and repeatable cold source suitable for TMRS2 could not be found. Thus, TMRS2 used the internal calibration approach of TMRS1. Namely, the temperature-stabilized waveguide load was used as a single calibration source to re-calculate the radiometer gain "constant" for each measurement cycle throughout the experiment. Without a second calibration source, offset was assumed to be constant. This approach had performed satisfactorily during REBEX-1, and did so during REBEX-3 as well.

3. **Perform absolute (hot/cold) external calibrations during every site visit.** The antennas would be calibrated during hot/cold calibrations and the effects of antenna temperature changes were included in the brightness calculations.

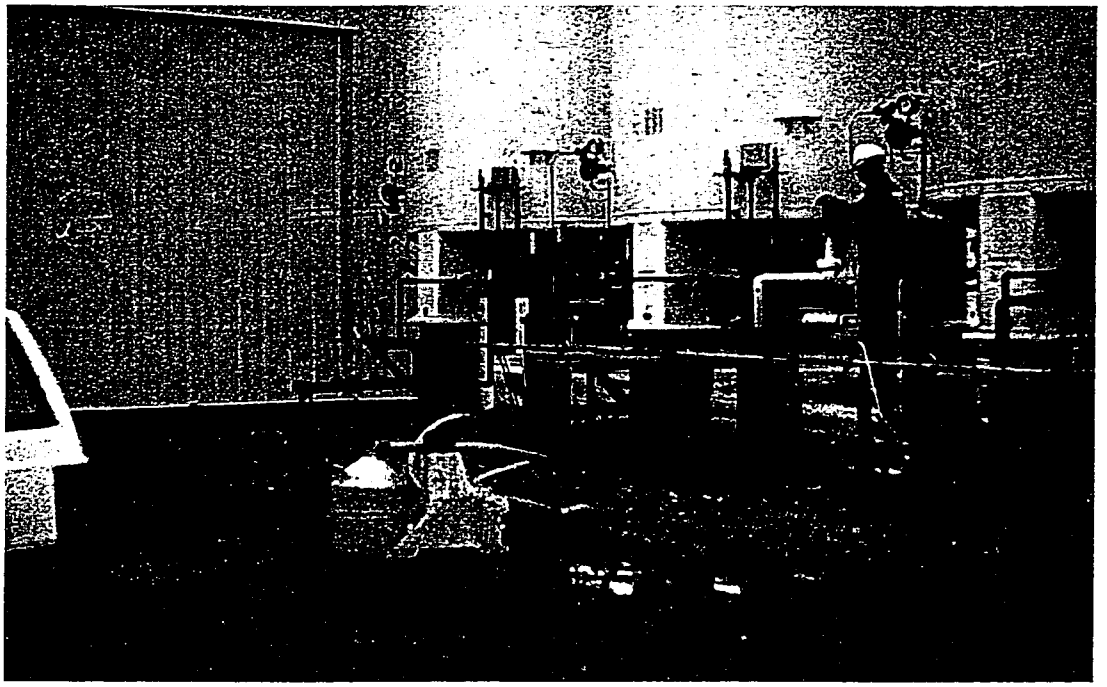

Figure 2.20: Filling the liquid nitrogen dewar in Prudhoe Bay, AK. LN_2 was needed to perform absolute radiometer calibrations. The hose was designed for filling tanker trucks.

Calibration Problems

In this section, I will discuss the instrumentation-related conclusions drawn from comparing TMRS2 brightness values vs. gridded, contemporaneous (within 15 minutes) SSM/I observations of the REBEX-3 site. The scientific implications and other details of the comparisons will be discussed in Chapter 4. Upon first making this comparison, a rather interesting and regular deviation was apparent. As the scatter plots in Figure 4.10 show, the basic 19 and 37 GHz TMRS2 vs. SSM/I brightness relationships are distinctly linear over the full range of brightness values over the whole REBEX-3 year. While these plots were both rewarding and exciting to see for *scientific* reasons, the large size of the departure from a 1:1 relationship at low brightness values was disturbing. It simply did not seem plausible that SSM/I and TMRS2 would observe brightnesses differing by as much as 20 K at the low end, for example, so *consistently.*

Moreover, the difference was too consistently linear with brightness to be attributable to natural phenomena. Note that there was no *a priori* expectation that the scatter plots would display "perfect" 1:1 relationships, or even linear relationships, for that matter. But, once the plots were generated and such a strong linear relationship was evident, it became difficult to find plausible explanations for why anything other than an instrumentation-related cause could be responsible for the remaining differences between the best-fit line and the 1:1 line.

A number of mechanisms were considered to explain the discrepancy. They fall into two categories: (1) problems with the calibration target and calibration procedure, and (2) circuit mismatches and losses. Biases due to these mechanisms were quantified and are tabulated below. Estimates of the absolute accuracy of the TMRS2 radiometers are also given.

Calibration target size and position The hot and cold calibration targets were rectangular pieces of open-cell microwave absorber material (foam rubber loaded with carbon).

The targets were unpolarized and had a convoluted surface. The absorber was 7.5 cm thick at the "peaks" and 2 cm thick in the "valleys" of the convolutions. The hot target was 36 x 20 cm and the cold target was slightly smaller (28 x 17 cm) in order to fit in a styrofoam liquid nitrogen container. During calibration, these targets were alternately held in front of the antenna corresponding to the channel being calibrated. The distance between the antenna aperture and the targets varied from 1–4 cm. The targets were beamfilling for the small 85 GHz aperture, but the cold target was marginally beamfilling for the large 19 GHz apertures. As a result, cold calibrations of the 19 GHz channels were sensitive to exact target position in all three dimensions. The 37 GHz channels also displayed some sensitivity, probably due to their slightly recessed installation within the tower housing. Laboratory tests were performed to measure the warm bias in the apparent cold target brightness due to horizontal position offsets and distance from aperture. Results are given in columns 2 and 3 of Table 2.6.

Calibration target orientation For the 19 and 37 GHz channels, the apparent cold target brightness was also sensitive to the orientation of the target relative to the E- or H-plane of the horn antennas because of the target's rectangular shape and marginally beamfilling size. The natural orientation was such that the H-polarized channels experienced slightly larger warm biases. Values for orientation warm bias are listed in column 4 of Table 2.6.

Calibration target emissivity The emissivities of the two targets were compared against a piece of new absorber and all were found to be equal to better than 7 parts in 10,000 (5 parts in 10,000 for the two targets alone) at room temperature. The difference in apparent brightness due to this emissivity difference between the two targets would be only 0.1 K for the 200 K hot target minus cold target temperature difference—insignificant for REBEX-3 purposes. Absolute emissivity was estimated from manufacturer data [20], to

be at least 0.9999 at the TMRS2 frequencies. The corresponding error due to assuming a value of exactly 1, would be less than 0.03 K for the REBEX-3 absorber temperatures—also insignificant for REBEX-3 purposes.

Cold target temperature To be solely responsible for the differences seen at low brightness values in the SSM/I comparison results, the cold calibration target temperature would have had to have been 22–40 K above the 77 K boiling temperature of LN_2. The observed difference between the best-fit lines and the 1:1 lines for the comparison channels is listed in the last column of Table 2.6. As explained above (and also listed in the table), contributions due to target position, orientation, and emissivity can account for only a fraction of the observed cold calibration differences. Great care was exercised during these on-site calibrations, and I initially thought that such a large warm bias was too large to have been due to actual target physical temperature.

The cold calibration procedure consisted of soaking the cold target absorber in the LN_2 bath, lifting the absorber out of the bath and holding the absorber in front of the antenna 1–4 cm away, waiting for TMRS2 to observe the absorber, then returning the absorber to the bath. It would have been preferable to have kept the absorber in its bath during the observation. However, the housing door prevented the LN_2 "bathtub" from being placed close enough to the antennas. The procedure for the hot target was identical, except no LN_2 bath was involved. I programmed the CDMS software to allow one person to perform the entire calibration procedure. During the course of a calibration session of all five microwave channels, the cold target would be removed from the LN_2 bath anywhere from 5 to 10 times.

I tried to minimize the total elapsed time for a calibration. However, radiometer temperature control duties required 20 sec of each minute of the computer's time and internal measurements also were made, so a complete calibration of a single channel took 2–3 minutes. Of that, the cold target sometimes remained outside the bath for as long as 80 sec. LN_2 would drain from the absorber pores during this time, and the target physical tem-

perature would rise. Later laboratory measurements demonstrated that the temperature rise was actually quite small for the particular type of absorber used, even after 60 sec outside the bath—*for a target in good physical condition.* But, the TMRS2 cold target was far from new. The "peaks" of the convolutions were worn, and the resulting "mesas" no longer had the original paint-like surface coating. Water and possibly CO_2 ice accumulated in the foam pores each time the absorber was out of the LN_2 bath and exposed to ambient air. Laboratory measurements demonstrated that the temperature of these mesas could be 140 K hotter than the temperature of the other areas of the face of the absorber (which remained near 77 K) after 80 sec.

I measured the projected area of the mesas to be 26% of the overall target area. The apparent cold target brightness due to 140 K warming of the mesa areas above 77 K would then be $(0.26 \times 217) + (0.74 \times 77) = 113$ K. That is 36 K hotter than 77 K! I actually used a cold target brightness value of 80 K in my calibration calculations to allow for small amounts of warming, so this warm bias constitutes a 34 K difference between the actual and assumed cold target brightnesses.

Calibration accuracy At this point, a few words about the accuracy of the hot calibration target are in order. The hot target temperature was much closer to the terrain brightness temperature than the cold target temperature. Thus, undesired energy viewed by the radiometers because of not-fully-beamfilling targets would result in only very small biases (hot or cold). The biases for the cold target listed in columns 2–4 of Table 2.6 are small (an indication that the cold target was actually quite close to beamfilling), and the corresponding biases for the hot target would be smaller. Furthermore, the hot target was larger (more beamfilling), and in better condition than the cold target. Ice buildup was not an issue. Thus, I am confident that the accuracy of the hot calibration points was much better than that of the cold calibration points.

Radiometer accuracy was a function of the scene brightness. If we take the EASE-

channel	horizontal offset	aperture distance	polarization orientation	sum	observed bias
19H	1.1	1.7	1.3	4.1	22.4
19V	1.7	1.7	1.0	4.4	39.9
37H	1.4*	2.8	2.2	6.4	33.9
37V	1.7*	0.4	1.2	3.3	39.9
85V	0*	0*	0*	0	NA

Table 2.6: Warm biases in Kelvins with respect to 77 K for the TMRS2 cold calibration target. Target temperature was nominally 77 K, but potentially warmer. Thus, values in all columns except the rightmost column might be larger. An additional bias of up to 36 K was due to mesa warming. When added to the "sum" values here, the bias mechanisms can account for the observed biases (to within 1 K for 37V). The 19H,V values are for an aperture distance of 2 cm. The 37H,V values are for an aperture distance of 4 cm. The 37 GHz radiometer was recessed approximately 2 cm relative to the 19 GHz radiometer. * indicates estimated values.

Gridded SSM/I brightness values to be less biased—and therefore more accurate—than the TMRS2 observations, then as seen in Fig. 4.10, TMRS2 overestimated the hotter brightnesses and underestimated the colder brightnesses.

By this measure, accuracy was best for scene brightness values near the crossover points of the best-fit and 1:1 lines, and worsening linearly with distance away from the respective crossover point for each channel. For example, if the crossover point for a particular channel was 240 K, the accuracy of a brightness reading of 250 K would be twice as good as that of a reading of 260 K. Again, I was mainly interested in the snow-free period. And, the brightnesses for all five channels during this period were closer to their respective crossover points than the colder wintertime brightness values. Thus, the accuracies for the brightnesses of interest were better than the accuracies at 77 K. The crossover points and amounts of under- and over-estimated brightnesses are listed in Table 2.7.

Radiometer circuit parameters In an ideal radiometer, only energy from the target would reach the receiver input ($T_{in} = T_g$ in Fig. 2.21). In a real radiometer, less than 100

channel	19V	19H	37V	37H
crossover	248.32	238.42	238.96	231.02
minimum T_b reading (whole year)	220.0	190.0	146.9	133.7
underestimate vs. SSM/I	-3.3	-9.6	-15.9	-20.0
minimum T_b reading (snow-free)	249.9	250.4	243.8	235.1
underestimate vs. SSM/I	0.2	2.4	0.8	0.8
maximum T_b reading	290.6	291.6	291.8	291.5
overestimate vs. SSM/I	4.9	10.5	9.1	12.5

Table 2.7: Absolute accuracy of TMRS2 microwave radiometer channels for $T_{b,gnd}$ observations during REBEX-3 using SSM/I as the standard. Add to the listed values ±0.3 K for the accuracy of the internal calibration load temperature and ±0.6 K for η_l error. Maxima for snow-free season are also the maxima for the year. All values are brightness temperatures in K.

percent of the target energy makes it to the receiver input. Some energy is reflected backward due to circuit mismatches and some is absorbed along the way by circuit components. Circuit mismatches and losses can introduce significant biases into radiometer observations. The mechanisms are independent (in theory, each can exist without the other), but in practice, biases are the product of both. The lossy components also self-emit, in proportion to their respective lossiness and their absolute temperature T_o, and some of this energy reaches the receiver input.

If η_l represents the efficiency of an antenna and its associated waveguide, then the self-emission is $T_o(1-\eta_l)$ Kelvins, and

$$T_{in} = T_g\eta_l + T_o(1-\eta_l). \tag{2.1}$$

When $T_g = T_o$, the self-emission balances the absorption, and the system becomes insensitive to mismatches and to the value of η_l. This condition was never achieved in the case of the TMRS2 radiometers due to their ovenized temperature control and total power configuration. During hot/cold calibrations utilizing external targets, hot target T_g values during REBEX-3 ranged from 270 K to 310 K, while cold target T_g values were nominally 80 K. T_o had values ranging from 318 to 330 K depending on time of year and the particular

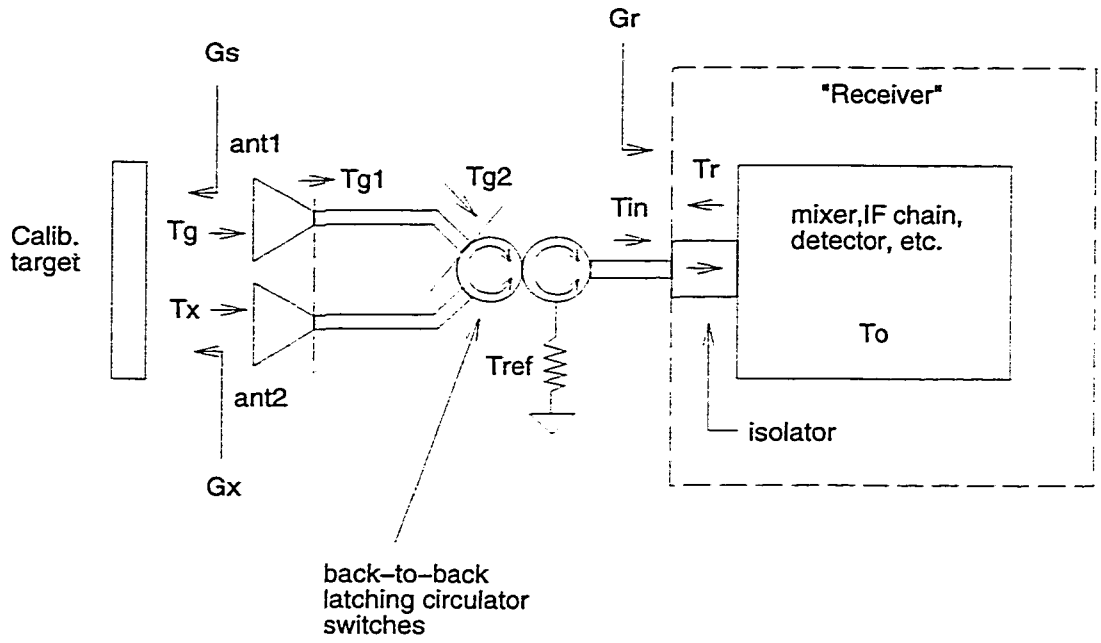

Figure 2.21: Simplified diagram of TMRS2 radiometer front end model. G_s, G_x, G_r are reflection coefficients, T_g and T_x are brightnesses entering antennas 1 and 2, respectively. T_{g1} is the brightness exiting antenna 1 and entering the waveguide. T_{g2} is the brightness available at the waveguide output. T_{ref} is the brightness temperature of the internal waveguide load. T_{in} is the brightness available to the rest of the receiver from the front end. T_r is the brightness of the rest of the receiver seen by the front end. And, T_o is the physical temperature of the receiver and circulators, assumed equal to T_{ref}.

radiometer.

Both mismatches and losses were accounted for during a TMRS2 calibration. However, if either changed, the calibration was no longer accurate. Mismatches were more likely to remain fairly constant vs. temperature and time, and I assumed this was so between on-site calibrations (except, obviously, for the 37 GHz radiometer). *Attenuation factors* were likely also fairly constant, but *self-emission* by the passive RF components was still proportional to their physical temperature.

I developed a detailed circuit model of the radiometer front end (see Fig. 2.21), and used it to conduct a sensitivity study of biases due to losses and mismatches. The model

indicated, as expected for a radiometer with no RF amplifier, that biases were most sensitive to the insertion losses of the passive components ahead of the mixer: the antenna, waveguide, isolator, and circulators. Biases were fairly insensitive to typical mismatch values of the waveguide reference load, the "source" matching of calibration targets held in front of the antennas, and leakage from the second antenna port due to imperfect circulators.

Measured antenna physical temperatures, T_{PA} were taken into consideration when calculating brightnesses using an assumed antenna efficiency, $\eta_l = 0.95$. The bias due to loss and self-emission in the antennas was

$$T_{b,target}(\eta_l) + T_{PA}(1-\eta_l) - T_{b,target} = \tag{2.2}$$
$$T_{PA}(1-\eta_l) - T_{b,target}(1-\eta_l)$$
$$(T_{PA} - T_{b,target})(1-\eta_l).$$

T_{PA} values during the snow-free season ranged from 300 K to 320 K. Using the tundra 1-cm temperature (range: 271–295 K) and the tundra emissivity of $(1-0.04)$, we can estimate the corresponding tundra brightness range as $T_{b,target} = 260 - 283$ K (12 K maximum difference), and thus the range of bias values as 0.55–0.60 K. Note that this bias was taken into account during calibration and in the calculation of microwave brightnesses.

The actual η_l may have differed from the assumed value. The potential error in the calculated brightnesses due to this is

$$(T_{PA} - T_{b,target})(\eta_{l,assumed} - \eta_{l,actual}). \tag{2.3}$$

A typical η_l range is 0.90–0.99, so this error was at most $12\text{K} \times \pm 0.05 = \pm 0.6$ K.

We can now estimate the absolute accuracy of the TMRS2 microwave radiometers by adding ± 0.3 K for the accuracy of the internal calibration load temperature and ± 0.6 K for η_l error to the limiting values listed in Table 2.7. Mismatches were accounted for by calibrations, and are assumed constant.

2.5 The Data

Summary annual and monthly plots of measured quantities are presented in Appendix A. Data are listed with respect to 1994 Julian Day for the entire experiment period in order to eliminate the need for end-of-year rollover detection in processing programs. So, 1 January, 1994 = day 1, 1 January, 1995 = day 366, etc. A calendar date conversion table is provided in Appendix A. The REBEX-3 data start officially on day 253 (10 September, 1994) and end on day 624 (16 September, 1995), a total of 371 days. The first and last days of microwave brightness observations were 29 August, 1994 (day 241) and 14 September, 1995 (day 622), a total of 381 days. All REBEX-3 field data in this dissertation are referenced to Alaska Standard Time, the civil time zone for the REBEX-3 site.

$$\begin{aligned} AST &= UTC - 9 \text{ hours} = UTC - 0.375 \text{ days} \\ LST &= UTC - (\text{Longitude in degrees})/360 \\ &= UTC - 148.88194/360 \\ &= UTC - 0.41356 \text{ days.} \end{aligned}$$

where

UTC = Coordinated Universal Time

AST = Alaska Standard Time

LST = Local Solar Time (the sun crosses the site meridian at exactly 1200).

Until day 259 (16 September, 1994), the nominal interval between measurement cycles was 20 minutes, or 0.0139 days. For the rest of the experiment, the nominal interval was 30 minutes, or 0.0208 days.

2.5.1 Gaps, Patches, and Interpolation

Gaps in both model input quantities and output comparison quantities were undesirable, particularly in the former. The tundra LSP/R model required continuous input values, but

gaps in the comparison quantities were fine as long as observations existed for the majority of the period of interest. Although there were many gaps in the data, the majority were brief: 1 or 2 missing data points (<90 minutes). I manually processed the 15,000+ data points for each model input variable and output comparison quantity. For most quantities, these gaps were trivial and reasonable to patch by linear or cubic spline interpolation.

Longer gaps up to 3 or 4 hours were also usually patchable in input quantities such as net radiation, which tended to change smoothly with time. For downwelling solar radiation ($R_S \downarrow$), screen air temperature (T_{air}), relative humidity (RH), 10-m wind speed ($U10$), and precipitation (P), LTER met data provided the best patches. The LTER data were from a site 1.5 km east of the REBEX-3 site, and except for RH, the match was so close that the LTER data could be used as-is to patch REBEX-3 data and vice versa. Through comparisons with the TMRS2 RH data, it was clear that the LTER RH sensor was defective. It displayed definite saturation behavior at RH values well below 100%. Nevertheless, the times of minima and maxima matched, and from periods when both sensors were operating, a running relationship between the LTER and REBEX-3 data was determined. Using this relationship, the gaps in REBEX-3 RH data were patched.

Thus, continuous model input data were generated for $R_S \downarrow$, $R_S \uparrow$, R_N, T_{air}, RH, P, $U10$, and ground IR brightness for days 502–588 (17 May–11 August, 1995). These 3 months of continuous data were more than sufficient for modeling purposes.

2.6 Summary

TMRS1 and REBEX-1 demonstrated the practicality of long-duration collocated microwave brightness and micro-meteorological observations for land surface process modeling research. REBEX-3 was undertaken from September, 1994 to September, 1995 in order to collect such data in the climatologically important arctic tundra region.

During REBEX-3, I successfully used the enhanced TMRS2 system to collect data for one full annual freeze-thaw cycle at a moist acidic tussock tundra site on the North Slope

of Alaska 160 km south of the Arctic Ocean. The tundra at this site is representative of a large fraction of North Slope tundra areas at the spatial scale of an SSM/I footprint, typically consisting of sedges, mosses, and lichens overlying Pergelic Cryaquept soils. Continuous permafrost underlies the entire region, and the active-layer depth at the site reached approximately 50 cm.

The site was adjacent to the Alaska Department of Transportation Sag River Maintenance Camp on the North Slope at mile 306 on the Dalton Highway. This is 30 km north of the Toolik Lake/Imnaviat Creek area and 50 km south of Happy Valley in a region along the Haul Road transect where few other energy balance measurements suitable for model input were made. These distances are such that at the resolution of both the 20-km ARCSyM arctic regional climate model and the 25-km Equal Area Scalable Earth-Grid (EASE-Grid) grids, a grid cell containing the REBEX-3 site would be in a cell between the cells containing the Toolik/Imnaviat vicinity and the Happy Valley vicinity.

Many changes and improvements were made to the instrument system, to upgrade it after REBEX-1 and to prepare it for operation in the arctic. The enhanced system, TMRS2, featured 55 sensors vs. 18, including a second polarization at 19 and 37 GHz, a Bowen ratio subsystem, a TDR soil moisture subsystem, snowpack temperature probes, an upwelling pyranometer, plus additional soil temperature and heat flux sensors.

All of these sensors were multiplexed so they could be deployed 30 m from the control computer and support trailer with a manageable number of cables. Control uplink and data downlink from the tower instruments utilized fiber optics for immunity against ground loops and electromagnetic interference. The control software was substantially upgraded to reflect all the changes and to increase robustness.

All temperature-sensitive circuits were contained in heated weatherproof enclosures, and heaters and temperature sensors which depended on only trailer power were designed into the system as part of a cold-start capability. The cold-start procedure helped prevent catastrophic system failure after power outages.

The instruments were deployed in August/September, 1994 on a flat moist acidic tussock tundra area west of the DOT camp. A 300-meter "extension cord" was installed to obtain electrical power from the DOT generators. Measured quantities included ground and sky radiobrightnesses at the SSM/I frequencies of 19.35 and 37.0 GHz (horizontal and vertical polarizations) and 85.5 GHz (vertical polarization), thermal infrared ground brightnesses, net radiation, upwelling and downwelling solar radiation, Bowen ratio, soil moisture and soil temperature profiles, soil heat flow, air temperature, relative humidity, wind speed and direction, liquid precipitation, snow depth, and snow temperature profile.

TMRS2 operated automatically during the year-long experiment, making observations every 30 minutes. A radiotelephone link provided remote control and data dump capabilities back to Michigan. In fact, the remote link would have allowed total reprogramming of the system, had it been necessary. Although we spent enough time in the field in person to ensure that our measurements accounted for the unique character of the tundra and the rigors of the North Slope, the remote link enabled us to collect data over a much longer time period than would otherwise have been possible. In addition to the deployment and retrieval trips, only three other visits were made to the site by the investigators for instrument calibrations, maintenance, and repair.

TMRS2 is one of only two such instrument systems for collecting collocated microwave, IR, and micro-meteorological observations. The radiometers are one of only 3 or 4 such SSM/I simulators hardened for extended ground-based deployment, and one of only two capable of long-duration remote operation without frequent absolute calibration. The system robustness has been demonstrated during REBEX-3 through REBEX-5, a total of over 500 deployed days.

I described specific problems with the Bowen ratio subsystem, the net radiometer, the housing door positioning, and the TDR soil moisture subsystem. These instrumentation problems encountered during REBEX-3 were not surprising considering the harsh environment, remote location, and many new and complex capabilities added to the system. None

of the problems was fatal. Plenty of useful data were obtained for model input purposes as well as for comparison vs. model output and vs. SSM/I observations. Several other research sites in the vicinity yielded related data, notably the Sag River LTER meteorological site whose data were used to patch gaps in the REBEX-3 data, and vice versa.

Cold calibration biases affected the *accuracy* of the REBEX-3 brightness observations, but the very strong correlation of the year's worth of TMRS2 radiobrightnesses vs. SSM/I radiobrightnesses during REBEX-3 (see Fig. 4.10) represents excellent proof of the stability, repeatability, and general accuracy of the TMRS2 radiometers across the 381 days of brightness observations and 371 days of collocated micro-meteorological observations—the longest such dataset I am aware of and the only one for arctic tundra. The primary conclusions and results based on these data and reported in the other chapters of this dissertation are not altered by these calibration biases. And, improvements to the calibration technique should drastically reduce biases for future observations.

CHAPTER 3

Tundra LSP/R Modeling

This chapter will address the first set of questions posed in the introduction chapter, which were: How well can we predict microwave emission by snow-free tundra underlain by continuous permafrost? Does it require special modeling considerations beyond those found adequate in a previous lower-latitude prairie grass case?

To answer these questions, I will describe the application of a modified prairie LSP/R model to the tundra case, beginning with a description of the model and the changes and upgrades made. Following the description is a presentation and discussion of outputs from the model run.

The current LSP/R models, including the tundra version described in this chapter, are not operational land surface models. That is, they cannot be directly included as the land surface package of a climate model such as ARCSyM [54] for two primary reasons. First and foremost, they were developed as high-fidelity research tools and are too computationally intensive. Many processes are represented in great detail. Of course, one of the intended roles of LSP/R models is to provide a means for developing simple parameterizations of land surface processes which *can* be used operationally. Secondly, the model input quantities are simplified. For example, the LSP/R models do not distinguish between large-scale and convective precipitation, and do not model CO_2 uptake and release.

3.1 Model Description

In this section, I describe the model physics, parameterizations, and assumptions. The tundra model traces its heritage from the prairie grass model of Liou [52], whose dissertation consists of a detailed description of the entire model. Here, there is space to present only enough detail to describe the model at a more general level.

A major philosophy during model development was to make changes in the model physics only when absolutely necessary. The forward component of the LSP/R approach is essentially a claim that a physically-based model can predict microwave emission signatures by modeling surface and subsurface state and surface flux quantities, provided of course, that the relevant processes are included with sufficient fidelity. And, the original model (validated for the prairie case), while not perfect, appeared to include the relevant physical processes for the tundra case.

The actual tussock tundra at the REBEX-3 site consisted of up to 20 cm of sedge, grass, and moss blending downward over 5 cm into an organic layer (peat) with an underlying mineral soil. The transition to the mineral horizon occurred at 15 cm depth. The definition of zero depth used throughout this chapter is the bottom of one's hand lying on the top of a tussock, chosen for consistency with other North Slope researchers [34].

In the tundra LSP/R model, this actual tundra is represented by a 2-layer vegetation canopy over a muti-layer 30-node soil column. The preceding sentence follows the usage of the soil science community in which the term "layer" refers to a depth interval possessing properties (e.g., hydraulic conductivity) that are different from those in other intervals within the column, and in which the term "nodes" refers to discretized depths at which model calculations are performed.

Within the canopy, I used exactly one node per layer. Within the soil, I specified profile quantities such as porosity and texture for 6 depths, which were then interpolated to generate values for all 30 nodes. Thus, I allowed soil parameters to vary continuously

vs. depth rather than specifying a "stairstep" discretized profile. This approach has the advantage of avoiding artificially sharp jumps in soil properties at layer boundaries with the potential distortion of the temperature and moisture profiles. However, care had to be exercised in the interpolation step to avoid oscillating or physically impossible values.

Since I used continuously varying profile parameters, the number of soil layers equaled the number of computation nodes. So, for simplicity throughout the remainder of this dissertation, I will use the term "layer" to refer to depth intervals of both properties and computations.

Together, the soil and canopy representations compose the land surface process (LSP) module. Microwave emission is modeled separately in the radiobrightness (R) module, which uses as its input the temperature and moisture profile outputs of the LSP module.

The entire soil-vegetation column is assumed to be horizontally uniform since the LSP/R model is one-dimensional. Of course, actual tussock tundra is quite "lumpy." Height differences from the tops of tussocks to the inter-tussock valleys averaged 20 cm at the REBEX-3 site. Tussocks diameters were 40–70 cm, and spacing was typically 50–80 cm. A one-dimensional model is appropriate for this first study, and most existing land surface process models are one-dimensional as well.

In the next subsections, I describe the processes and parameters modeled in the soil portion of the column. In the succeeding subsections, I describe the processes and parameters modeled in the vegetation canopy. And finally, I will describe the microwave emission module. The description is an abridged version of Liou's. I use the same variable names for consistency.

3.1.1 Soil Heat and Moisture Transport

Heat and moisture transport within the soil column are intimately coupled, and highly nonlinear in nature. The following conservation relations apply:

$$\frac{\partial X_h}{\partial t} = -\nabla \cdot \vec{Q}_h \tag{3.1}$$

$$\frac{\partial X_m}{\partial t} = -\nabla \cdot \vec{Q_m} \tag{3.2}$$

where X_h is the total heat content of a unit volume (J/m^3), X_m is the total moisture content of a unit volume (kg/m^3), $\vec{Q_h}$ is the vector heat flux density out of the unit volume (J/m^2s), and $\vec{Q_m}$ is the vector moisture flux density out of the unit volume (kg/m^2s).

$\vec{Q_m}$ includes liquid $\vec{Q_l}$ and vapor $\vec{Q_v}$ flux densities, i.e.,

$$\vec{Q_m} = \vec{Q_l} + \vec{Q_v} \, . \tag{3.3}$$

Moisture extraction from layers within the root zone (i.e., transpiration) is accounted for by reducing $\vec{Q_l}$ relative to the value it would have if there were no vegetation.

The original model included adaptive temporal resolution that varied with solar insolation and precipitation. I added memory so that temporal resolution remains high after the actual rainfall for a time which depends on the amount of precipitation. I found this necessary because of the high hydraulic conductivity of the surface peat layers, as well as freezing and thawing behavior. The model time step is approximately 10 seconds (low resolution) or 1 second (high resolution).

3.1.2 Soil Freezing and Thawing

The handling of soil freezing and thawing is accomplished through the addition of terms in the heat and moisture conservation equations to account for any ice in each layer. All heat and moisture transport coefficients in partially frozen layers (liquid water coexists with ice below 273 K) are reduced by a factor $10^{10\theta_i}$ from their unfrozen values at the same liquid content [87]. θ_i is the volumetric ice content (m^3/m^3). As is commonly done to simplify soil freezing models, no heave (expansion) is allowed.

Because of model problems which manifested themselves as an over-concentration of moisture at the freezing front, only the upper 20 cm of the active layer were modeled for the results presented in this dissertation. The 0–20 cm results are very nearly the same whether or not the lower depths are included in model runs. However, there was a tremendous speed

advantage to using fewer layers. And, until the freezing front behavior is corrected, I did not feel it particularly useful to include the lower depths.

3.1.3 Soil Column Boundary Conditions

The lowest (Nth) soil layer was subject to heat and moisture "forcings" from the (N-1)th layer, but not from below.

The energy and moisture boundary conditions at the top of the soil column are specified by

$$\vec{Q_h}\,(0) = R_{ns} - H_s - \rho_l L_v (E_s + E_{tr}) \tag{3.4}$$

$$\vec{Q_m}\,(0) = \rho_l (D_c - E_s - E_{tr} - Rr), \tag{3.5}$$

where R_{ns} is the net radiation (W/m^2) absorbed by the soil, H_s is the sensible heat flux (W/m^2) from the soil to the atmosphere, ρ_l is the density of liquid water (kg/m^3), L_v is the latent heat of vaporization of water (J/kg), D_c is the water drainage rate (m/s) from the canopy to the soil, Rr is the runoff rate (m/s), and E_s and E_{tr} are the evaporation and transpiration rates (m/s), respectively, from the soil to the atmosphere.

3.1.4 Vegetation Layers

Vegetation is modeled using two layers: a photosynthetically-active "canopy" layer above an insulating "thatch" layer.

Canopy Layer

The energy and moisture conservation relations for the canopy are

$$\frac{\partial X_{hc}}{\partial t} = F_c \tag{3.6}$$

$$\frac{\partial X_{mc}}{\partial t} = \rho_l (P_c - D_c - E_c), \tag{3.7}$$

where X_{hc} is the total heat content (J/m^2s) of a unit area of the canopy layer, X_{mc} is the total moisture content (kg/m^2) of a unit area of the canopy layer, P_c is the precipitation

rate (m/s), and E_c is the rate of evaporation (m/s) from the wet fraction of the canopy.

The total heat content $X_{hc} = (W_c c_c + W_l c_l)(T_c - T_o)$, where W_c is the canopy dry mass per unit area (kg/m^2), W_l is the mass per unit area (kg/m^2) of canopy moisture, c_c is the specific heat of the canopy (J/kg-K), c_l is the specific heat of liquid water at constant pressure (J/kg-K), T_c is the temperature of the canopy (K), and T_o is a reference temperature (K).

X_{mc} is the sum of the moisture (kg/m^2) inside the canopy plants, W_{ls}, considered constant, and the moisture (kg/m^2) on the outside of the plants, W_r. W_r is allowed to change, for example, due to evaporation.

F_c is net heat energy flux into the canopy from the atmosphere:

$$F_c = R_{nc} - H_c - \rho_l L_v (E_c + E_{tr}) \tag{3.8}$$

where R_{nc} is the net radiation absorbed per unit area of the canopy (W/m^{2}s), H_c is the sensible heat flux to the atmosphere per unit area of canopy (W/m^{2}s), and E_{tr} is the transpiration rate (m/s) from the dry fraction of the canopy.

Thatch Layer

The thatch layer was originally included in the prairie LSP/R model to account for the effects on the thermal regime of organic material at the base of the grass canopy, but above the soil. It consisted of a 2 cm layer of organic material exchanging radiative energy with the atmosphere, the canopy layer above, and the soil surface below. For tundra, the boundary between soil and vegetation is much less distinct. However, there is a significant amount of organic material at the base of the tundra canopy which then blends into the upper highly organic layers of the model soil column. Therefore, I decided to retain the thatch layer in the tundra model.

The energy conservation relation for the thatch layer is

$$\frac{\partial X_{ht}}{\partial t} = F_t \tag{3.9}$$

where X_{ht} is the total heat content (J/m^{2}s) of a unit area of the thatch layer.

$X_{ht} = W_t c_t (T_t - T_o)$ where W_t is the thatch wet biomass (kg/m^2), computed as a fraction of the total wet biomass of the canopy based on field measurements. c_t is the thatch specific heat (J/kg-K), and T_t is the temperature of the thatch (K).

$F_t = R_{nt}$ where R_{nt} is the net radiation absorbed by the thatch layer (W/m^{2}s) computed from a radiative energy balance with the atmosphere, the canopy layer, and the soil surface.

Shortwave and Longwave Radiation Budget

Downwelling solar shortwave and atmospheric longwave radiation are absorbed and reflected by the canopy, thatch, and soil. Shortwave and longwave emissivities, transmissivities, and reflectivities are all accounted for. For simplicity, scattering is neglected. So, for example, the canopy shortwave transmissivity is

$$\tau_c = \exp(-\kappa_c \mathrm{LAI_c}), \tag{3.10}$$

where κ_c is the canopy extinction coefficient ($= 0.4/cos(Z)$ [93]), $\mathrm{LAI_c}$ is the canopy leaf area index, and Z is the solar zenith angle.

And, the thatch shortwave transmissivity is

$$\tau_t = \exp(-\kappa_c \mathrm{LAI_t}), \tag{3.11}$$

where $\mathrm{LAI_t}$ is the thatch leaf area index.

The net radiation absorbed by the canopy layer R_{nc} is computed from (absorbed downwelling shortwave radiation) + (absorbed downwelling longwave sky radiation) + (absorbed longwave emission from the thatch) − (2-sided longwave emission by the canopy).

The net radiation absorbed by the thatch layer R_{nt} is computed from (absorbed downwelling shortwave radiation) + (absorbed longwave emission from the canopy) + (absorbed longwave emission from the soil) − (2-sided longwave emission by the thatch).

The net radiation absorbed by the soil surface R_{ng} is computed from (absorbed downwelling shortwave radiation) + (absorbed longwave emission from the thatch) − (1-sided

longwave emission by the soil) where I have assumed 100% vegetation cover (no bare soil).

Sensible and Latent Heat Fluxes

Canopy and soil sensible heat fluxes to the atmosphere are modeled by the bulk aerodynamic method [90]. For 100% vegetation cover, the model sets the soil sensible heat fluxes to zero. The canopy sensible heat flux H_c (W/m^2) is given by

$$H_c = \rho_a c_{p,a} \frac{T_c - T_{a,r}}{r_{ac}}, \tag{3.12}$$

where ρ_a is the density of air (kg/m^3), $c_{p,a}$ is the specific heat of air (J/kg-K), T_c is the canopy temperature (K), $T_{a,r}$ is the air temperature at screen height (K), and r_{ac} is the aerodynamic resistance between the canopy and the atmosphere (s/m).

For 100% vegetation cover, the model sets the soil evaporation to zero. The canopy evaporation E_c (m/s) is given by

$$\rho_l L_v E_c = \rho_a L_v \delta_w \frac{q_{sat}(T_c) - q(T_a)}{r_{ac}}, \tag{3.13}$$

where ρ_l is the density of liquid water, L_v is the latent heat of vaporization of water (J/kg), δ_w is the fraction of canopy area covered by water, $q_{sat}(T_c)$ is the saturation specific humidity at T_c, and $q(T_a)$ is the specific humidity of air at T_a.

Transpiration E_{tr} (m/s) takes place over the dry fraction of the canopy area, according to

$$\rho_l L_v E_{tr} = \rho_a L_v (1 - \delta_w) \frac{q_{sat}(T_c) - q(T_a)}{r_{ac} + r_c}, \tag{3.14}$$

where r_c is the canopy resistance (s/m), a function of LAI, shortwave radiation, soil moisture, air temperature, and air vapor pressure deficit [68].

3.1.5 Microwave Emission Regime

Dielectric Constant of Soil

The Radiobrightness-module computes the complex dielectric constant of moist soil from the LSP-module's calculated temperature and moisture profiles. It uses the semi-empirical

mixing model of Dobson *et al* [18] to account for soil solids, bound water, free water, and pore air, with a fifth component added to account for any ice.

Dielectric Constant of Vegetation

The complex dielectric constant of the tundra vegetation ϵ_{wg} is computed using the dual-dispersion relation of Ulaby and El-Reyes [91]. Although that relation was based on detailed measurements of corn, I have not found a more suitable model for tundra. This model's principal independent variable is gravimetric canopy moisture. In the original prairie version, the canopy moisture was held constant. I corrected the tundra version to use the canopy moisture predicted by the LSP-module and the dry canopy biomass (held constant).

Once ϵ_{wg} is known, the refractive index n_t of the vegetation layers is approximated using the following relation:

$$n_t = 1 + v_{wg} n_{wg}, \tag{3.15}$$

where $n_{wg} = \sqrt{\epsilon_{wg}}$, and the volume fraction of the wet vegetation v_{wg} is assumed to have an exponential height profile with a scale height h_{cs} (m).

The optical thickness of the vegetation is

$$\tau_o = 2 k_o h_{cs} \kappa v_{wg}(0)(e^{-h_c/h_{cs}} - 1), \tag{3.16}$$

where κ is the imaginary part of n_t, k_o is the vacuum wavenumber (1/m), h_c is the total vegetation height (m), and $v_{wg}(0)$ is the incremental wet volume fraction at the bottom of the vegetation column. I have changed the R-module to use this general expression in place of one which was specific to the prairie grass case.

The total observed brightness $T_{b,tmrs}$ (observed by the tower radiometers) is modeled as the sum of four components [23]: upwelling vegetation brightness, downwelling vegetation brightness reflected off the soil interface and attenuated by one trip through the canopy, upwelling soil brightness attenuated by one trip through the canopy, and downwelling sky

brightness reflected off the soil interface and attenuated by two trips through the canopy.

$$T_{b,tmrs} = T_{c,e}(1 - e^{-\tau_o/\mu}) \quad (3.17)$$

$$+ \; T_{c,e}(1 - e^{-\tau_o/\mu}) R_p(\mu) e^{-\tau_o/\mu} \quad (3.18)$$

$$+ \; T_{s,e}(1 - R_p(\mu)) e^{-\tau_o/\mu} \quad (3.19)$$

$$+ \; T_{sky} R_p(\mu) e^{-2\tau_o/\mu} \quad (3.20)$$

where $T_{c,e}$ is the effective emission temperature of the vegetation (K), $T_{s,e}$ is the effective emission temperature of the soil (K), $R_p(\mu)$ is the Fresnel reflectivity for polarization p at the soil surface (assumed smooth for simplicity), and $\mu = \cos(\text{SSM/I incidence angle, } 53°)$. As explained in Chapter 2, the quality of the REBEX-3 sky brightness data is suspect, so I set the sky contribution to zero when computing $T_{b,tmrs}$. In the next chapter, I do estimate the downwelling microwave sky brightness as having a range of 10–30 K (see Fig. 4.15). But with a tundra net reflectivity of ~ 0.04, neglecting the sky contribution results in a worst-case difference of only 1.2 K. This is not a significant difference for this study.

For simplicity, the radiobrightness module used in this dissertation does not currently consider scattering in its brightness predictions. At 19 GHz, this was not an issue in the earlier prairie grass case. At 37 GHz, however, the model predicted prairie brightness was an average of 6 K too hot, which is probably due to the omission of scatter darkening effects.

This completes the description of the soil heat and moisture transport regimes, the handling of soil freezing and thawing, the vegetation layers and surface flux modeling, and the microwave emission regime.

3.2 Comparison of Tundra Model and Field Observations

In this section, I present results from the tundra LSP/R model and a comparison of model predictions and field measurements. A discussion accompanies each set of graphs. The modeled period begins on 1995 day 142.0 and ends on day 161.0 (REBEX-3 days 507–526). I wanted to find a period near the beginning of the snow-free season in order

to investigate the deepening of the active layer before it passed the 30 cm mark (second deepest temperature sensor depth). I also wanted to have a few sufficiently cold nights to be able to test LSP/R model freeze/thaw behavior in the critical upper soil and vegetation layers.

Day 142 was at the beginning of the snow-free season, and the air and IR surface temperatures were just beginning to pass the freezing mark. Active layer depth was passing 10 cm, and the tundra was saturated from melted snow. By day 161, active layer depth had just passed the 20 cm mark. Nighttime cooling was sufficient to cause surface freezing several times, with subsequent thawing the next day. I will begin with a description of the parameter values and initial conditions used in the modeling.

3.2.1 Initial Conditions and Parameter Values

The prediction skill of any model depends on the process representations (reviewed in the previous section) and the accuracy of the soil and vegetation parameters and the appropriateness of the initial conditions (reviewed below).

For this study, I focused on modeling the tussocks (these being more "visible" to our tower instruments than the inter-tussock "valleys" and therefore of more direct interest).

3.2.1.1 Texture and porosity profiles

I specified the porosity and texture profiles at 6 initial depths following measured values reported by Hinzman *et al* [35] for the Imnaviat tundra site 20 km south of the REBEX-3 site. Both sites have similar tundra vegetation and underlying Pergelic Cryaquept soils [61]. The upper horizons are organic and contain no significant mineral matter (clay or silt; there is virtually no sand on the North Slope) from the surface downward until the transition to a silt loam mineral soil in the 10–15 cm depth range. The porosity and texture values I used are listed in Table 3.1.

Lower boundary depths for each model layer, $z(i)$, were calculated using the exponentially increasing function $z(i) = z(i-1) + z(1)\exp^{1.075i}$, where $i = 2$–30 is the layer number,

depth (cm)	soil type	porosity	organic vol. frac.	clay vol. frac.	quartz vol. frac.	sat. hydr. cond. (m/s)
0.1	peat	0.90	0.090	0.005	0.005	10^{-5}
2	peat	0.90	0.086	0.007	0.007	10^{-5}
7	peat	0.86	0.126	0.007	0.007	10^{-5}
12	muck peat	0.70	0.26	0.02	0.02	10^{-5}
17	silt loam	0.55	0.20	0.10	0.15	10^{-5}
22	silt loam	0.54	0.16	0.10	0.20	10^{-6}

Table 3.1: Texture and porosity values used to generate 30-layer interpolated profiles for modeling.

and $z(1)$= 2 mm. Soil properties for each layer were set equal to the midpoint values as determined by cubic spline interpolation.

3.2.1.2 Thermal Regime

Initial temperature values for each layer were interpolated from measured values on 1995 day 142, the beginning of the modeled period. Depths below 20 cm were not included for the model results presented in this dissertation. However, I have tested the model with soil columns which extended down to 5 m, well into the permafrost. In those cases, initial temperatures for depths below 40 cm (the deepest REBEX-3 temperature sensor) were determined from a separate annual model [53] as had been done with the prairie version of the LSP/R model.

Representative values of the specific heat, thermal conductivity, and density of the six modeled constituents are listed in Table 3.2 for comparative purposes. Actual values of several of these quantities are functions of temperature.

3.2.1.3 Moisture Regime

At the beginning of the test period the tundra was wet with melted snow, and the active layer was only 10 cm deep. From the on-site conditions and other North Slope tundra sites [33, 77], I know that the soil below approximately 15 cm was saturated. The initial soil moisture profile was set to 40% (uniform) on a volume basis. Experience had shown that

material	specific heat (J/kg-K)	thermal conductivity (W/m-K)	density (kg/m^3)
clay	702	2.93	2650
quartz	755	8.892	2660
organic matter	1932	0.251	450
water	4218	0.586	1000
ice	2106	2.240	917
air	1005	0.249	1.23

Table 3.2: Representative thermal properties of soil constituents, water, and air at 10° C and ice at 0° C (from Liou [52] and Nakano and Brown [63]).

initializing to a specific moisture profile was unnecessary as the model redistributes the moisture to a more realistic profile within the 1–2 day spin-up period. I decided that starting with as much moisture in the soil column as possible was the most realistic choice, and I found 40% to be the highest such value with which the model would survive spin-up.

Based on the porosity profile, I set the saturated hydraulic conductivity profile to (10^{-5} m/s) at the surface, decreasing to a value of 10^{-6} m/s at 22 cm. 10^{-6} m/s is of the same order of magnitude as measured values reported by Hinzman *et al* [35] for the active layer at Imnaviat and Rovansek [77] for tundra soils along the Arctic coast at Prudhoe Bay. 10^{-5} m/s was found experimentally to be the largest practical value which the model would operate under the conditions specified for the modeled period. This is a very high value, but justifiable in light of the 90% porosity at the surface.

3.2.1.4 Vegetation Parameters

Based on site observations, I set the vegetation height at 20 cm. I kept the exponential shape of the mass profile as in the Dahl, *et al* [15] grass canopy used for the prairie LSP/R model validation, but with the scale height reduced by same factor of 3 in order to maintain a similar relative profile.

For the root density profile, I again left the functional form unchanged, but reduced the

parameter	value
canopy albedo	0.15
thatch albedo	0.4
soil albedo	0.4
canopy IR emissivity	0.98
thatch IR emissivity	0.97
soil IR emissivity	0.96
vegetation wet biomass	1.56 kg/m^2
vegetation coverage fraction	1.0
initial stored water on canopy	0.4 mm
wind measurement height	10 m

Table 3.3: Other model parameters.

overall root zone depth from 30 cm to 20 cm to match REBEX-3 site conditions, placing the roots within the organic horizons.

I set the tundra LAI to 3, for compatibility with the LSM operational land surface process model of Bonan [7]. LSM actually uses an LAI which varies during the summer. The tundra LSP/R model employs a constant LAI, so I chose LAI=3, which corresponds to the LSM value for the comparison period.

I lowered by a factor of 2 the assumed minimum canopy surface resistance to 200 s/m, while keeping the maximum at 5000 s/m. This was an attempt to account for mosses. Mosses do not possess stomata, and thus can transpire quite freely vs. plants with stomata. Mosses are thought to significantly increase the overall latent heat flux from tundra to the atmosphere [60]. The effect of this change was minimal in test runs.

Based on a visual estimate, I increased the mass ratio of thatch to total vegetation from 0.0663 to 0.1.

3.2.1.5 Other Parameters

Other parameter values not requiring detailed explanations are listed in Table 3.3. Tundra-specific values were used when available. For example, canopy albedo and vegetation wet biomass represent REBEX-3 measured values. The other values were from the prairie case and still seemed reasonable for the tundra case.

3.2.2 Comparison Results and Discussion

In this section, I display the output of the tundra LSP/R model run using the parameter values and initial conditions described in the previous section. The model was forced using REBEX-3 observed variables, including solar and net radiation, precipitation, humidity, wind speed, and thermal IR skin temperature.

Model outputs shown below consist of soil temperature and moisture (liquid, ice, and total) profiles; canopy, thatch, and soil temperatures; canopy sensible and latent heat fluxes; and microwave brightnesses at 19 and 37 GHz (V and H polarizations).

For comparison, observed soil temperature profile data, thermal IR skin temperature, air and soil temperatures, precipitation, and TMRS2 brightness at 19 and 37 GHz (V and H polarizations) are shown.

3.2.2.1 Temperature

Comparison of the predicted and observed soil temperature contours (Fig. 3.1) indicates that the modeled soil column has many of the "correct" features, but is too warm vs. observed temperatures. I interpret this to mean that heat from the surface is penetrating downward too easily and/or that heat loss from the soil is not happening rapidly enough. The predicted 273.1 K contour remains essentially fixed at 20 cm throughout the comparison period, and just shows signs of moving downward toward the end. The measured contours are derived from temperature sensors at 1, 5, 10, 15, 20, 30, and 40 cm. So, the precision of the indicated 273.0 K contour should be taken with some caution. I believe, for example, that the sharp downward drop of at day 158.8 is an artifact of the coarse sensor spacing and the contour generation algorithm. The true 273 K contour must be a more gradually sloping one, and this may also affect the other contour lines.

Predicted canopy, thatch, and soil surface temperatures are shown in (Fig. 3.2) for the 142–162 period as well as a 2-day period for more clarity. These three temperatures display the expected relative relationships. In general, the canopy is the warmest during the day

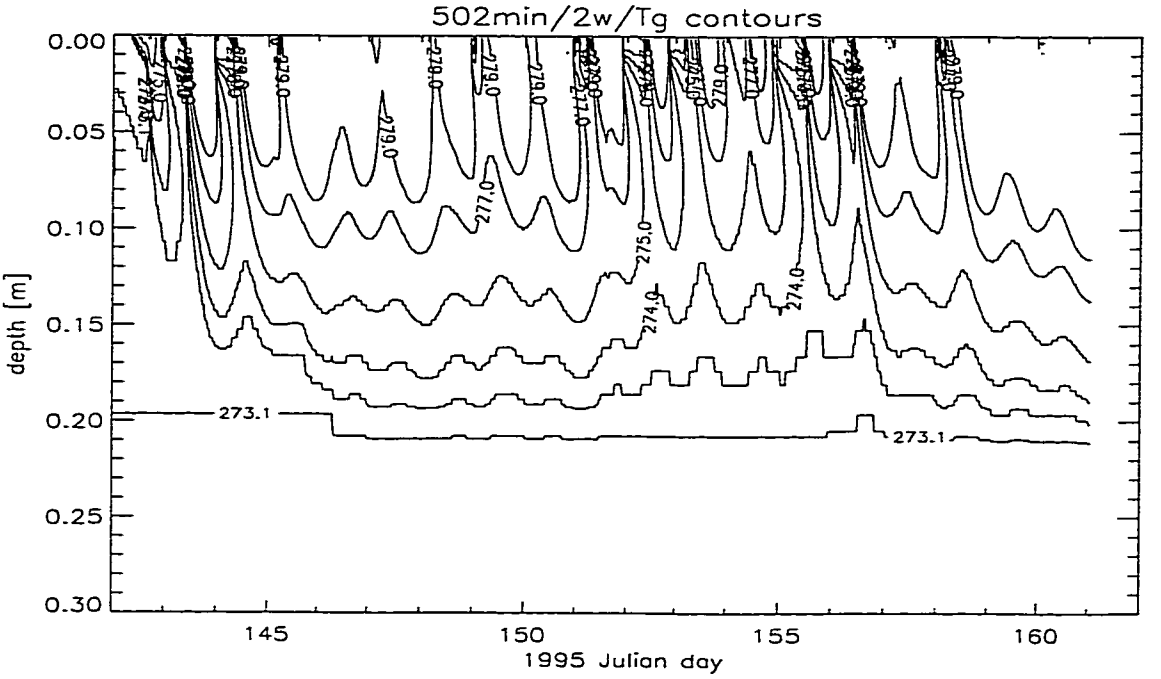

(a) Model predicted soil temperature contours (Kelvins).

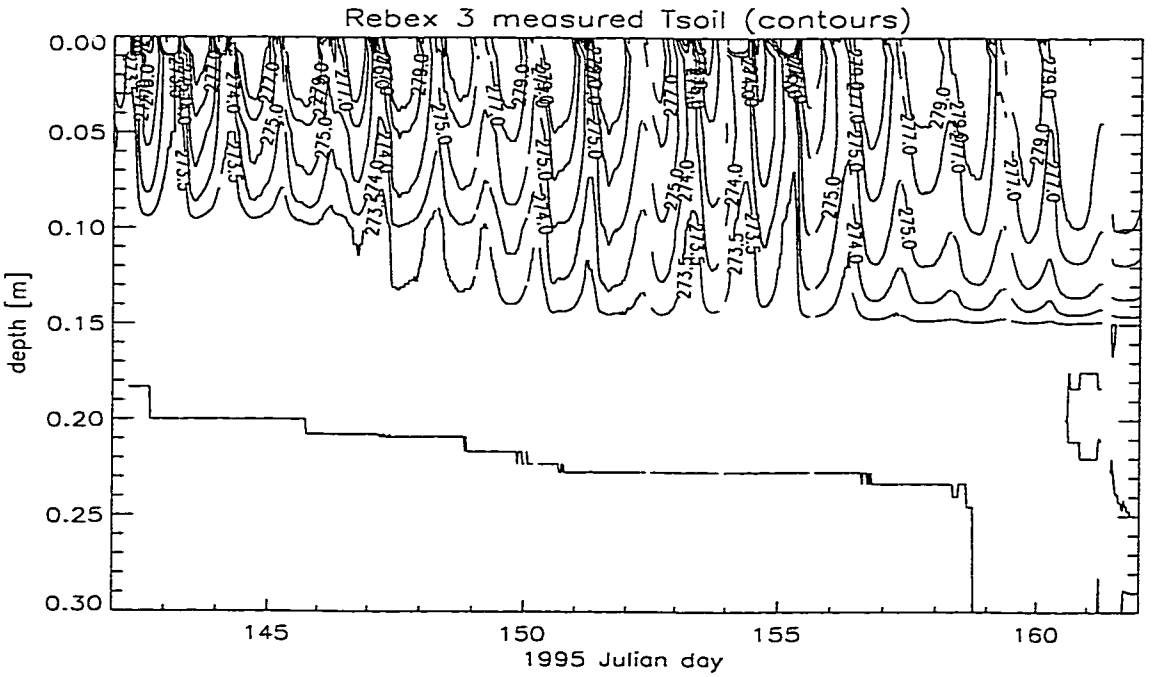

(b) REBEX-3 observed soil temperature contours (Kelvins).

Figure 3.1: Predicted and observed soil temperature contours.

and coolest at night, while the reverse holds for the soil surface temperature. The thatch temperature is between the other two. Observed 2 m air and IR temperatures are also plotted, and display plausible relationships vs. the model temperatures.

A better way to evaluate the predicted soil temperatures is to examine the temperatures vs. time shown in Fig. 3.3. The averages (AD) and standard deviations (SD) of the differences between measured and predicted canopy and soil temperatures are listed in Table 3.4. The match is best at 20 cm because of the proximity of the freezing front. The large latent heat of fusion of water tends to keep the freezing front from moving rapidly compared with thawed and dryer layers nearer the surface. Thus, since the predicted 20 cm temperature started out near the actual temperature which was at freezing, the predicted temperature tended to stay near the actual temperature. The predicted soil surface temperature was also a good match to observed canopy and IR temperatures as seen earlier. The temperatures at in-between depths do not match as well; the model overpredicts at all other depths. This could be due to incorrect soil thermal conductivity and/or too much solar radiation transmitted through the canopy and thatch and absorbed by the soil. Underestimated thermal conductivity would reduce thermal communication between all layers and the cold temperature reservoir at 20 cm, leading to overheating. And, in turn, underestimated thermal conductivities could indicate that porosity and texture values are off or that the soil was too dry. On the other hand, overestimated thermal conductivities could allow heat from the surface to penetrate downward more easily, which would also lead to overheating. Moisture appears to play a significant role. For example, following the large precipitation events of days 148, 151, and 152, the magnitude of the overheating at 5, 10, and 15 cm is reduced until day 156.

Farouki [24] notes that dominant heat transfer mechanisms in soils are a function of soil grain size and degree of saturation. Tundra peat is extremely porous, values of 70-90% in the top 15 cm being not uncommon [35]. The upper 10 cm of the active layer was never saturated, and the pore spaces were filled mostly with air. Under these conditions, the

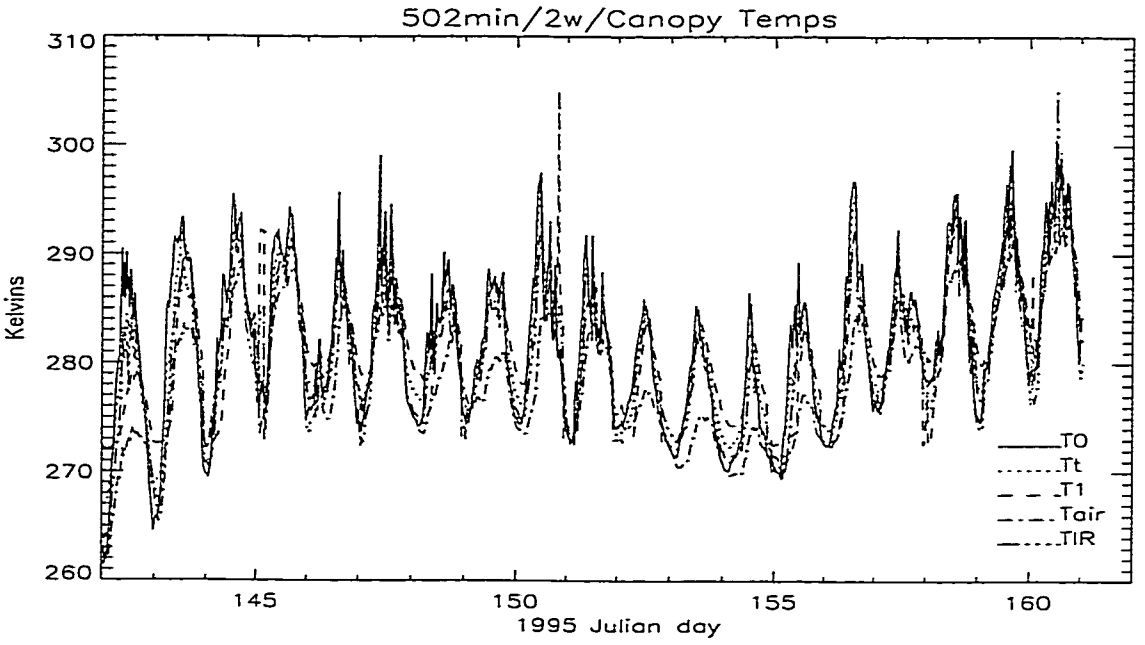

(a) Predicted surface temperatures.

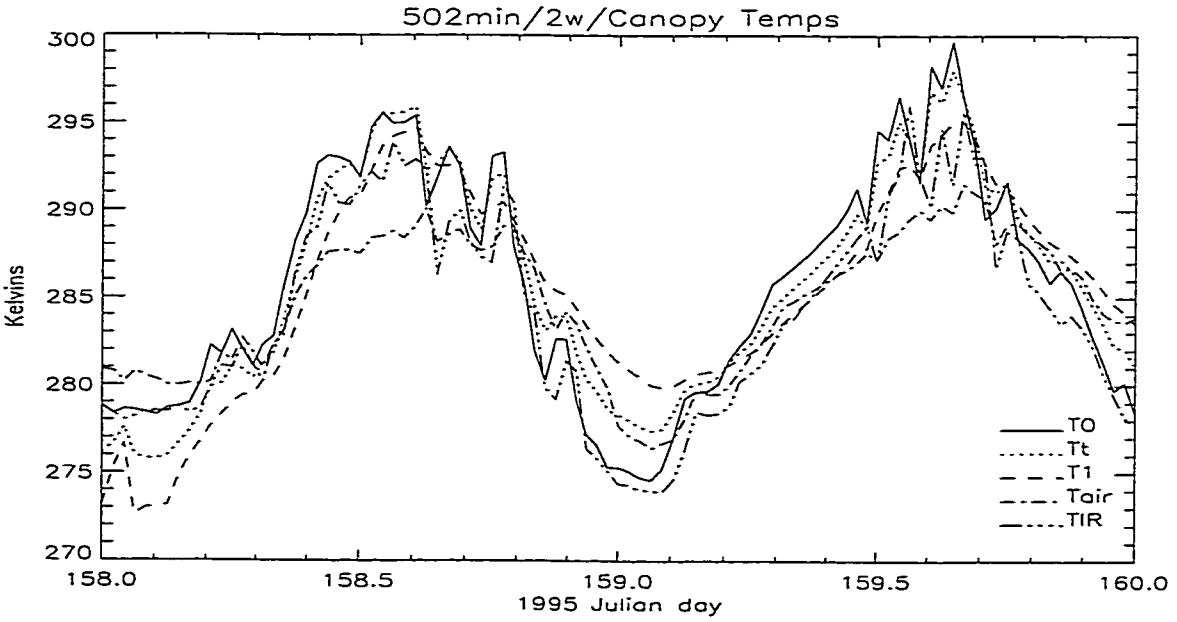

(b) Closeup of surface temperatures for days 158–160.

Figure 3.2: Predicted canopy (T0), thatch (Tt), and soil surface (T1) temperatures, and observed 2 m air (Tair) and IR (TIR) temperatures.

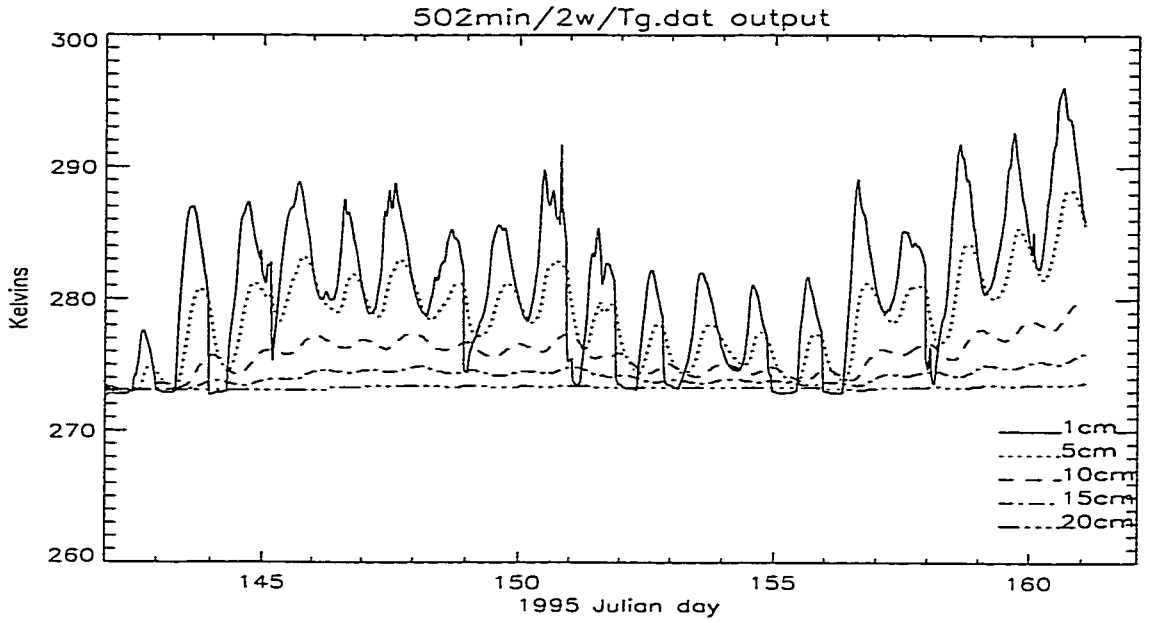

(a) Model predicted soil temperatures.

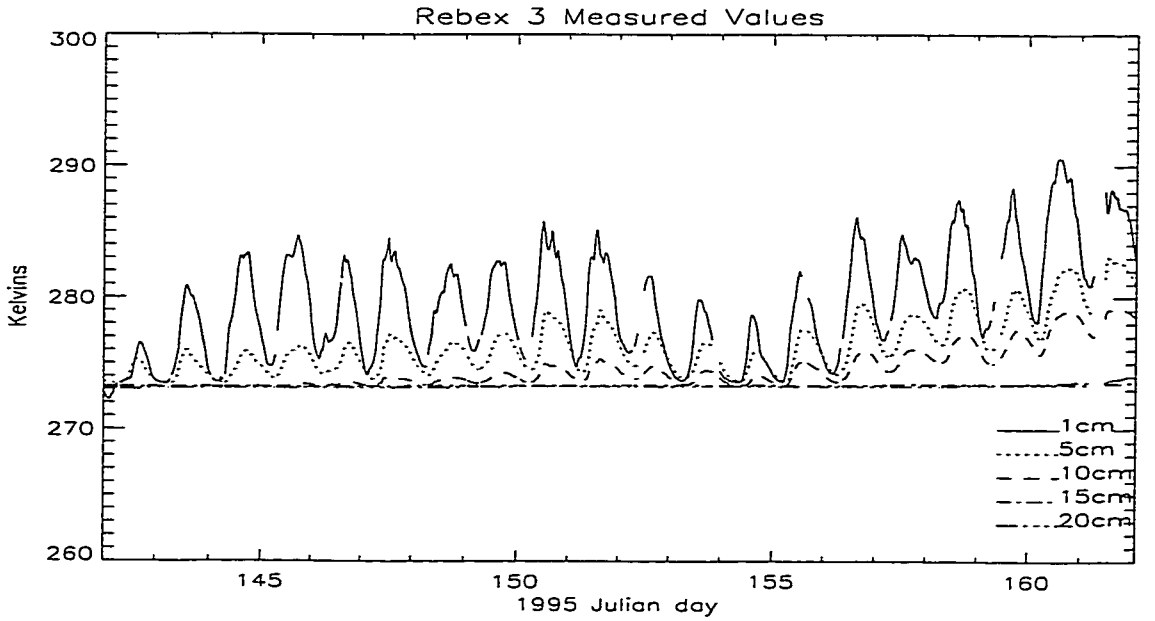

(b) REBEX-3 observed soil temperatures.

Figure 3.3: Predicted and observed soil temperatures at 1, 5, 10, 15, and 20 cm.

depth (cm)	AD	SD
canopy	1.56	2.97
1	1.77	3.11
5	2.58	3.35
10	1.39	1.89
15	0.84	1.00
20	0.05	0.10

Table 3.4: Statistics of the differences between measured and predicted canopy and soil temperatures (predicted - measured).

predominant heat transfer mechanisms are convection in air and heat radiation. In contrast, the significant heat transfer mechanisms in the saturated thawed portion of the mineral soil are conduction through soil particles and water, and heat transport due to water movement. The tundra LSP/R model did not include heat radiation as a transfer mechanism within its soil layers, only between the surface layer and the vegetation layers. Air convection and heat radiation from subsurface layers to the atmosphere would remove heat from the soil column and could help explain the model's overestimates of soil temperatures.

The un-modeled mechanisms of radiation and air convection would be less dominant during the wetter days mentioned above. On the other hand, the modeled processes of energy transport through the pore water would be more significant, and the predicted temperatures should better match the measured temperatures, as they do.

The 3-dimensional nature of actual tussocks might also explain some of these overestimates. The side of a tussock facing away from the sun would receive less solar insolation than if the tundra were flat. And, the inter-tussock valleys are partly shadowed and thus cooler. Both of these factors are consistent with cooler soil temperatures and cooler brightness temperatures.

3.2.2.2 Moisture

Total water, liquid water, and ice content contours are plotted in Figs. 3.5, 3.6, and 3.7, respectively. As explained in the previous chapter, the corresponding field measurements

are of uncertain usefulness and have not been fully processed. In spite of that, it is still possible to evaluate certain aspects of these outputs.

The response to precipitation—namely, evaporation from the canopy, wetting and drying of the surface soil layer, and infiltration into deeper soil layers—all appear realistic. Modeled infiltration into the highly porous peat layers is extremely rapid, as in real peat.

The appearance and disappearance of short-lived ice at the surface appears realistic. The timing is very consistent with cold nights and the availability of moisture from recent precipitation. Longer-lived ice, however, still represents a problem. This is more clearly seen in model runs with layers extending well below the front (see Figure 3.4). Qualitatively, ice formation and thawing at the freezing front (initially at 20 cm) appear realistic, with moisture being drawn to the front from above and below. This is expected, but the concentration continues to build. Eventually, the total moisture content exceeds the local porosity—a non-physical result. This problem only occurs when a freezing front persists for more than a day. I have not seen it for cases in which the whole temperature profile is either all frozen or all thawed. Interestingly enough, the predicted depth of thaw vs. time in Fig. 3.4 is quite close to measured values.

3.2.2.3 Surface Fluxes

Model predicted canopy fluxes due to evaporation (Flhec), transpiration (Flhet), and sensible heat (Fshc) are shown in Fig. 3.9. As plotted, negative values represent energy fluxes to the atmosphere, so positive peaks of sensible heat indicate nighttime warming of the canopy by the air.

3.2.2.4 Microwave Brightnesses

As seen in Figs. 3.10–3.12, model predicted 19 and 37 GHz brightnesses clearly have the right basic shape and signature compared to REBEX-3 observations. But the model overpredicts both the mean level and the amplitude of the diurnal variations. The averages (AD) and standard deviations (SD) of the differences between measured and predicted

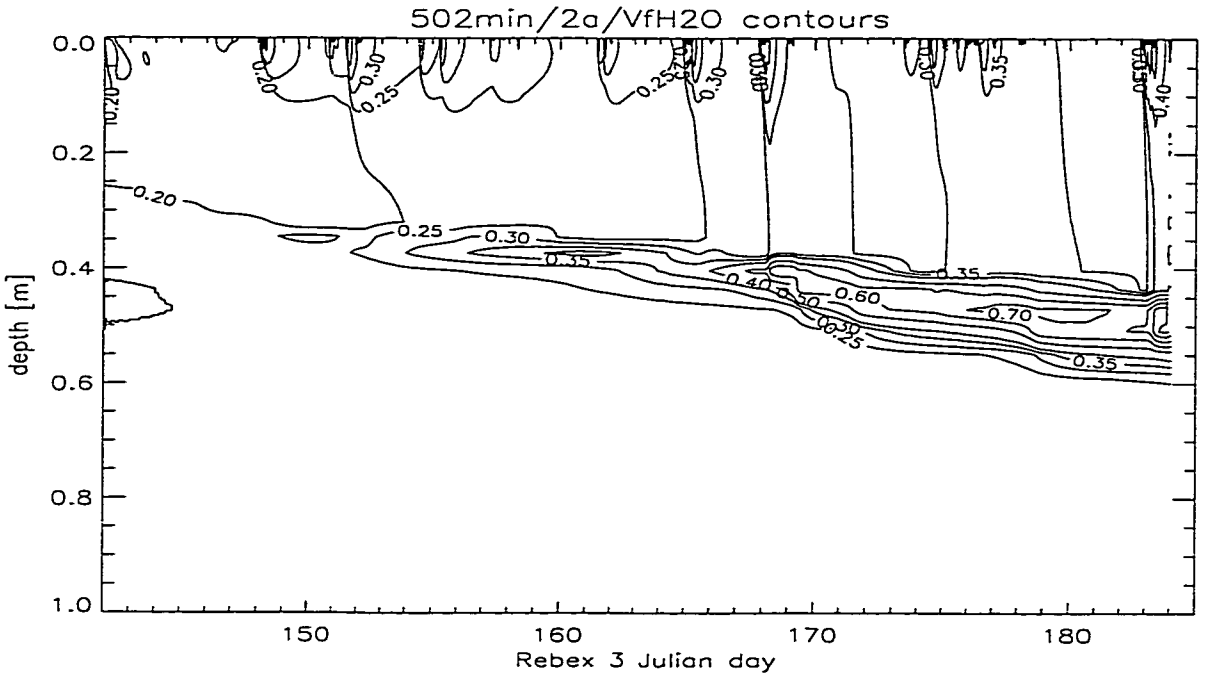

Figure 3.4: Model predicted total moisture content contours for a 60-layer run [volume fraction]. Concentration at the freezing front is qualitatively realistic, but quantitatively unphysical. Thaw depth vs. time, however, is close to measured values.

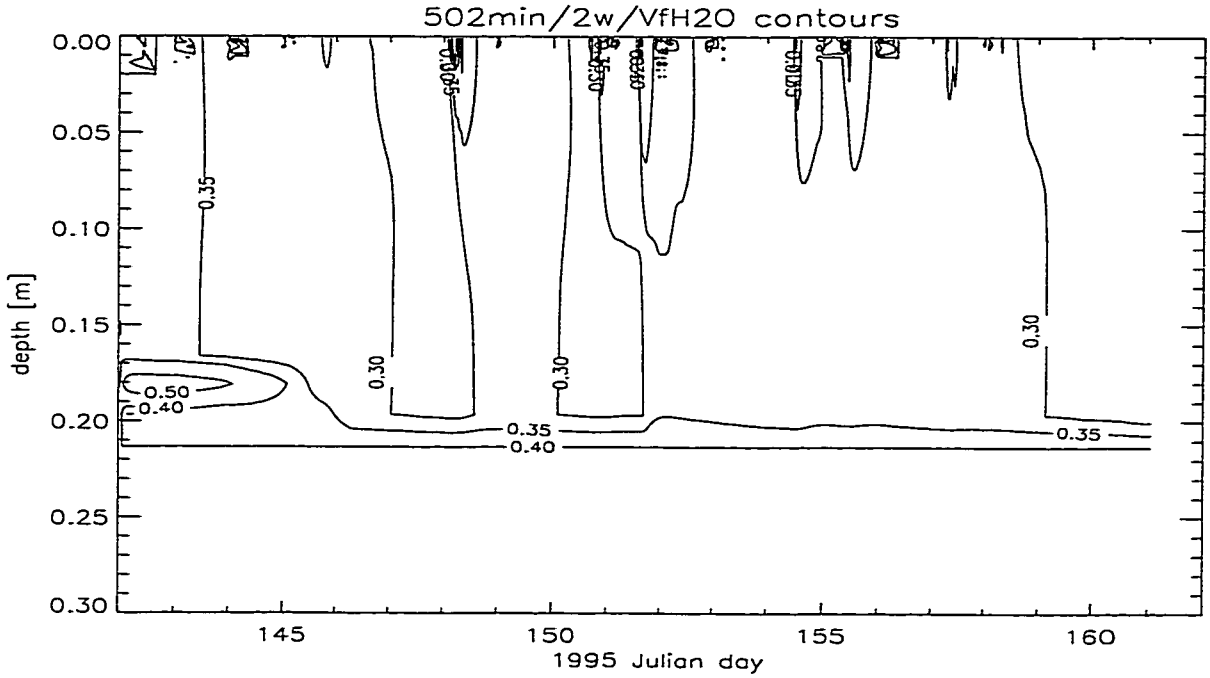

Figure 3.5: Model predicted total moisture content contours [volume fraction].

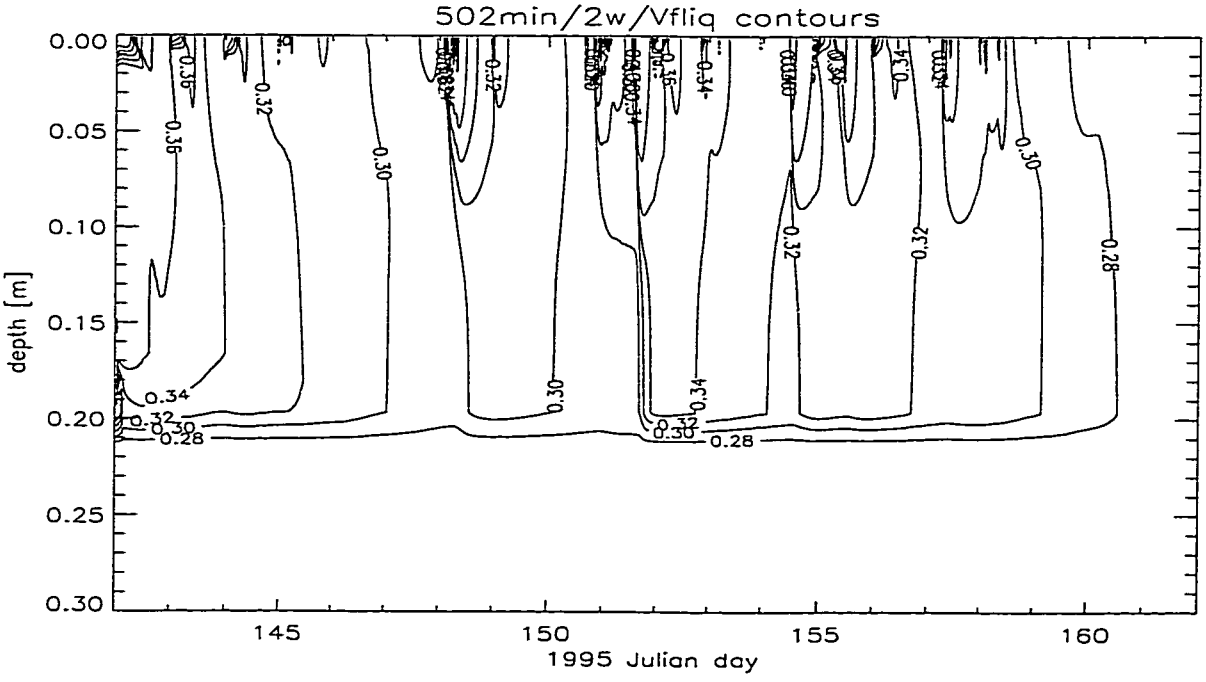

Figure 3.6: Model predicted liquid water content contours [volume fraction].

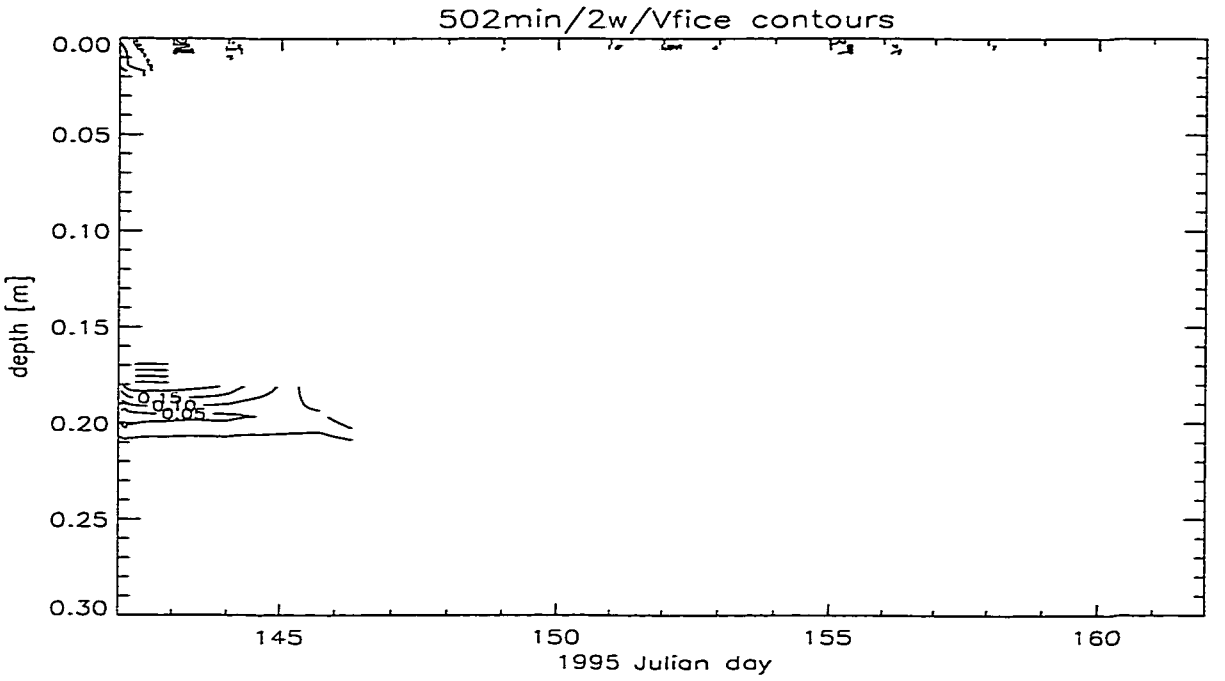

Figure 3.7: Model predicted ice content contours [volume fraction].

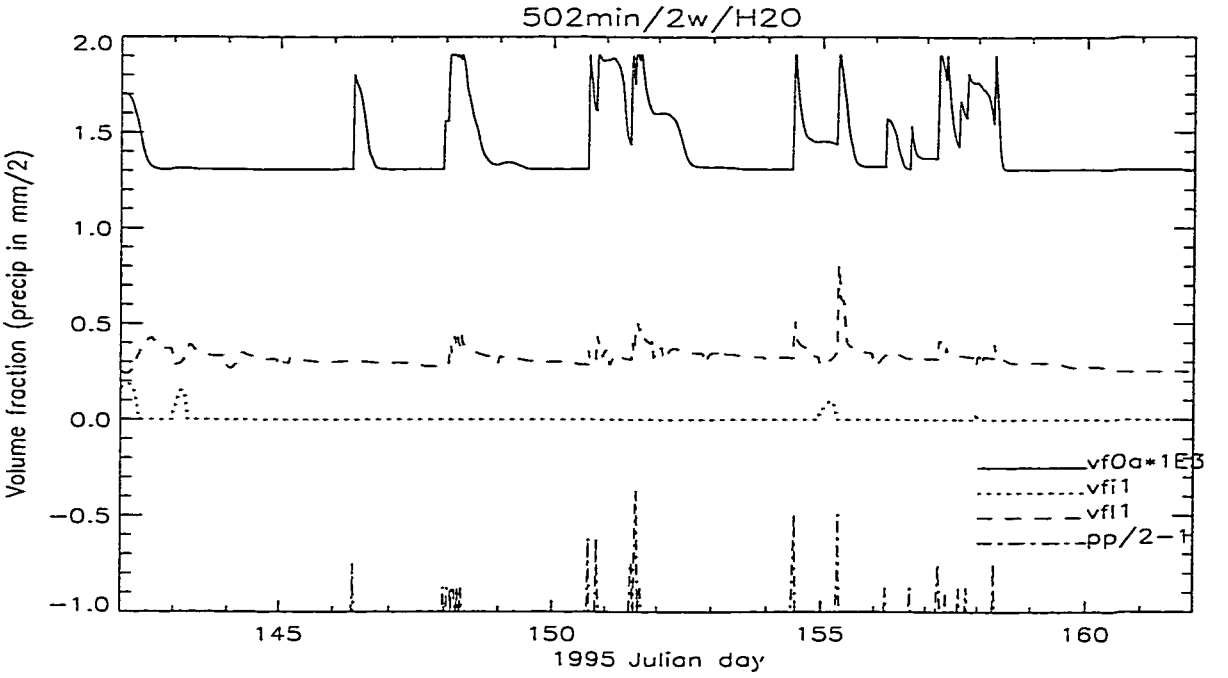

Figure 3.8: Model predicted canopy moisture (vf0a in mm), soil surface layer ice (vfi1) and liquid water (vfl1) volume fractions, and precipitation (in mm/2 and offset by -1 for clarity).

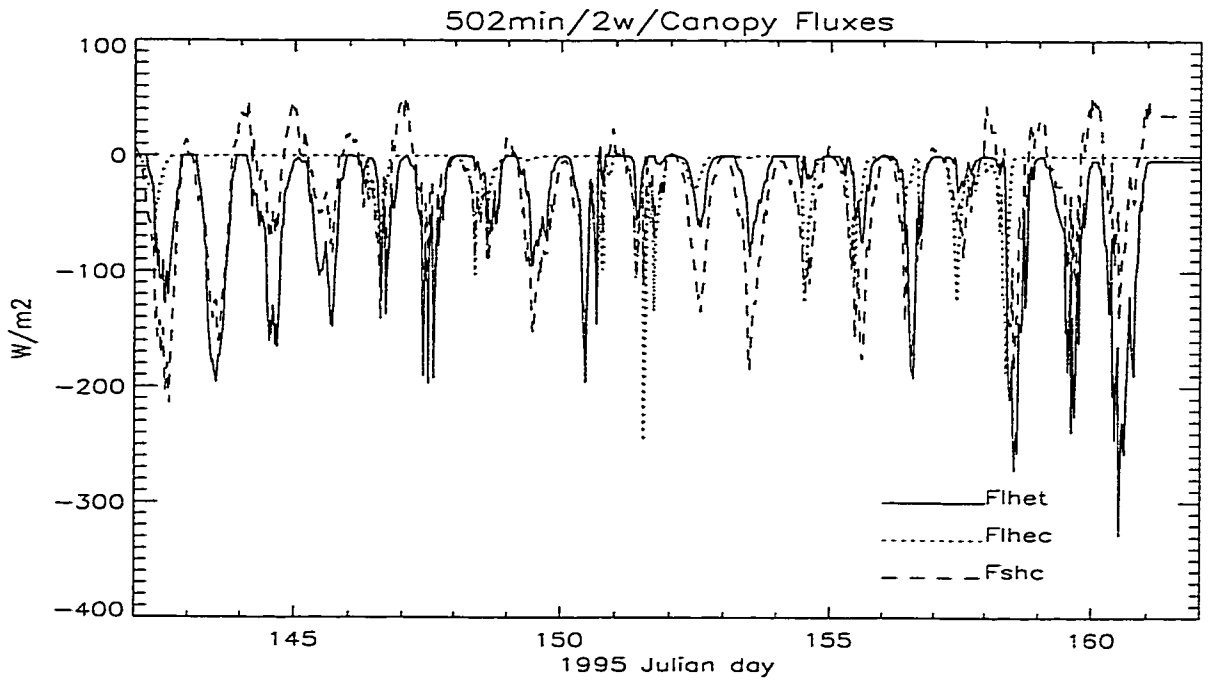

Figure 3.9: Model predicted canopy fluxes.

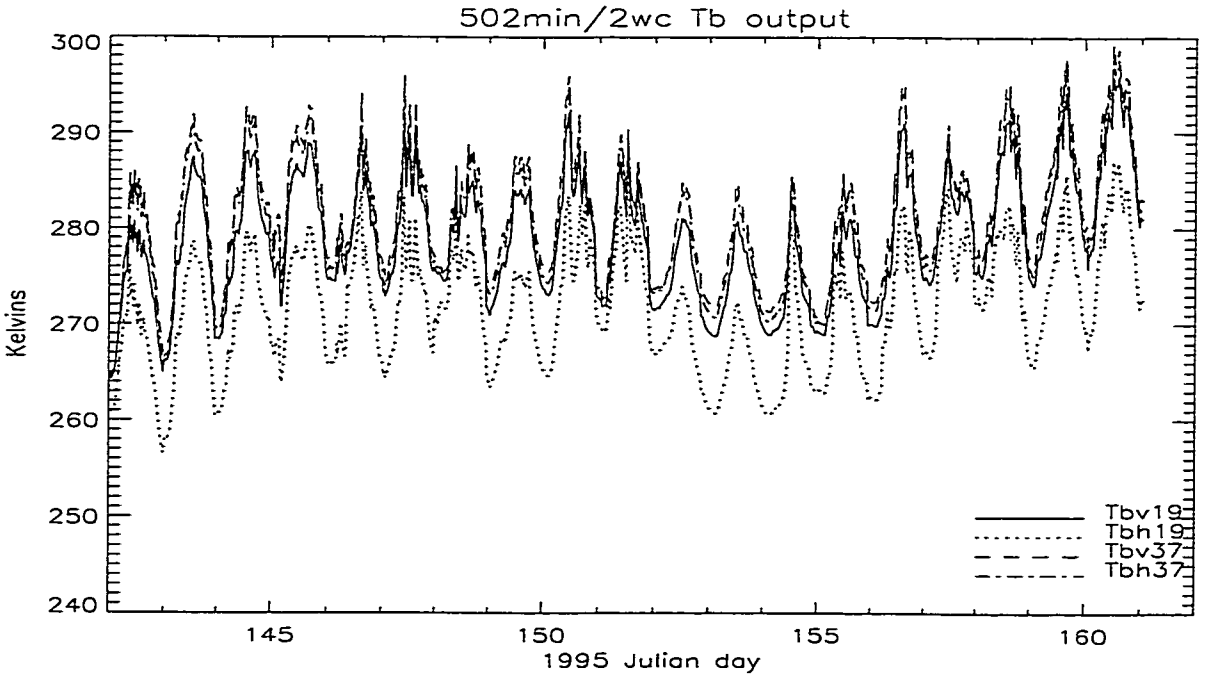

Figure 3.10: Model predicted 19 and 37 GHz brightnesses.

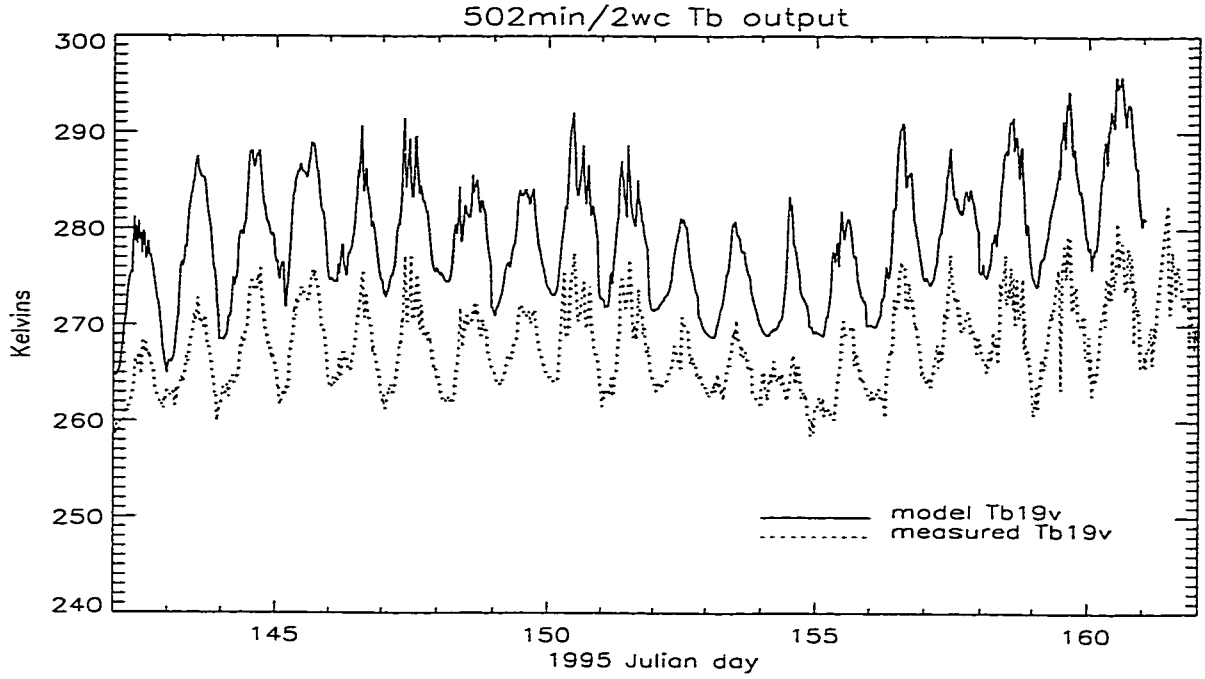

(a) 19 V

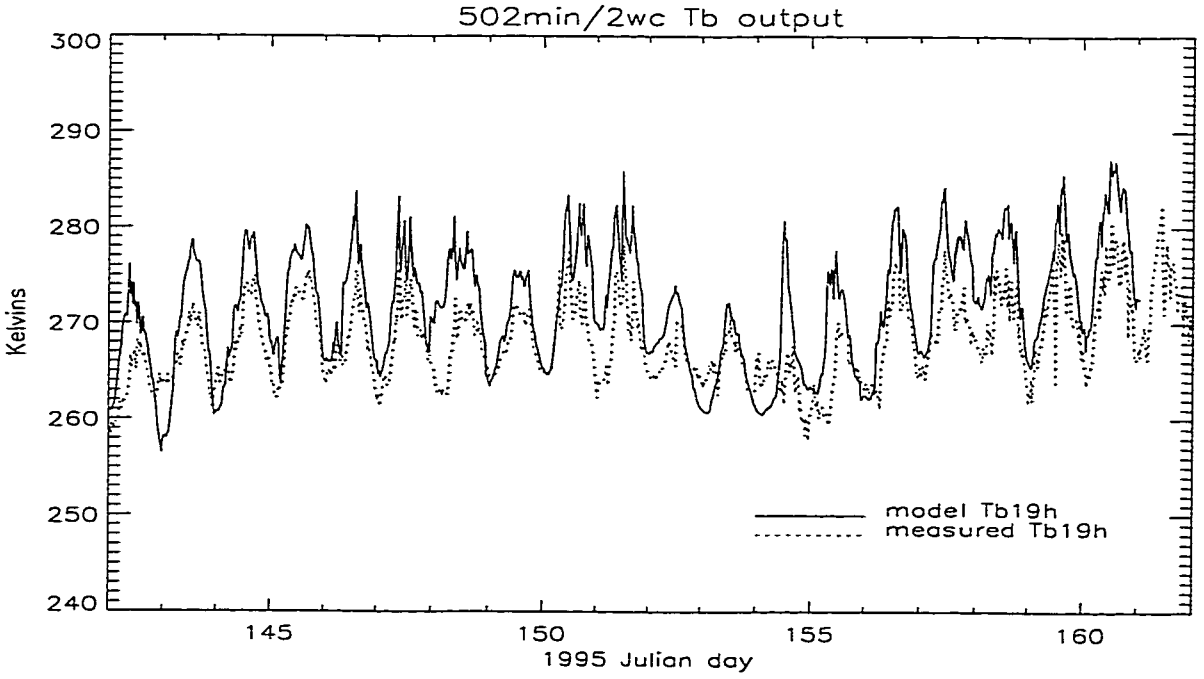

(b) 19 H

Figure 3.11: Predicted and observed 19 GHz V- and H-pol brightnesses.

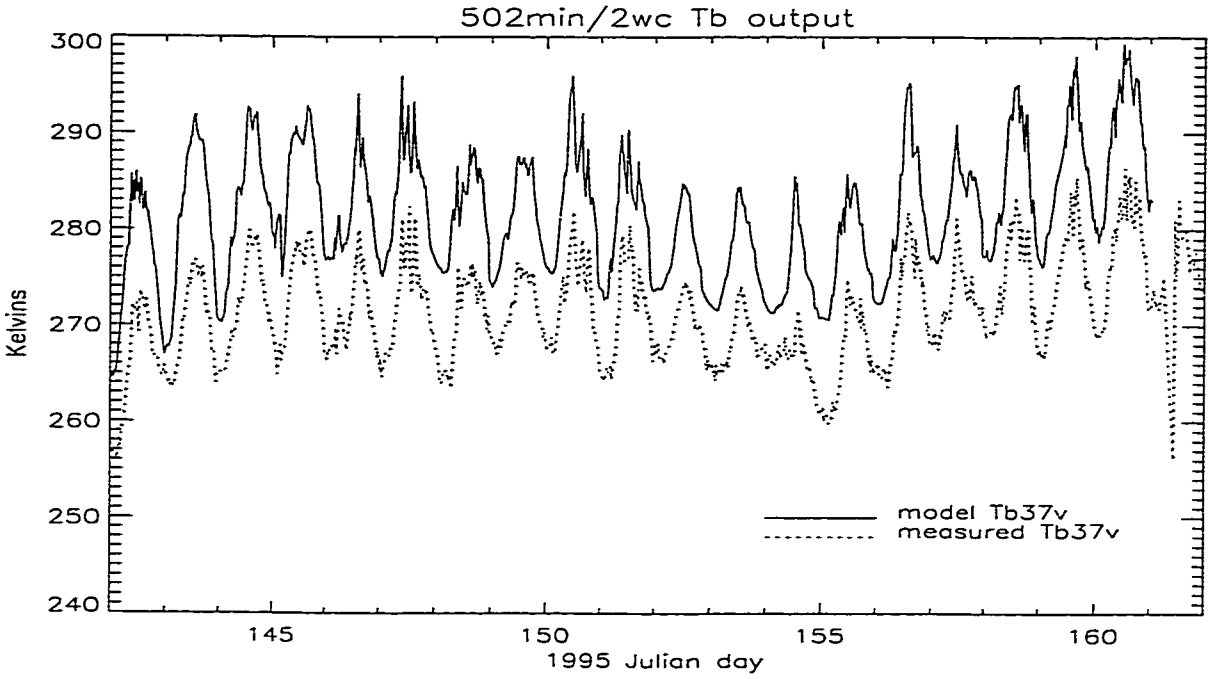

(a) 37 V

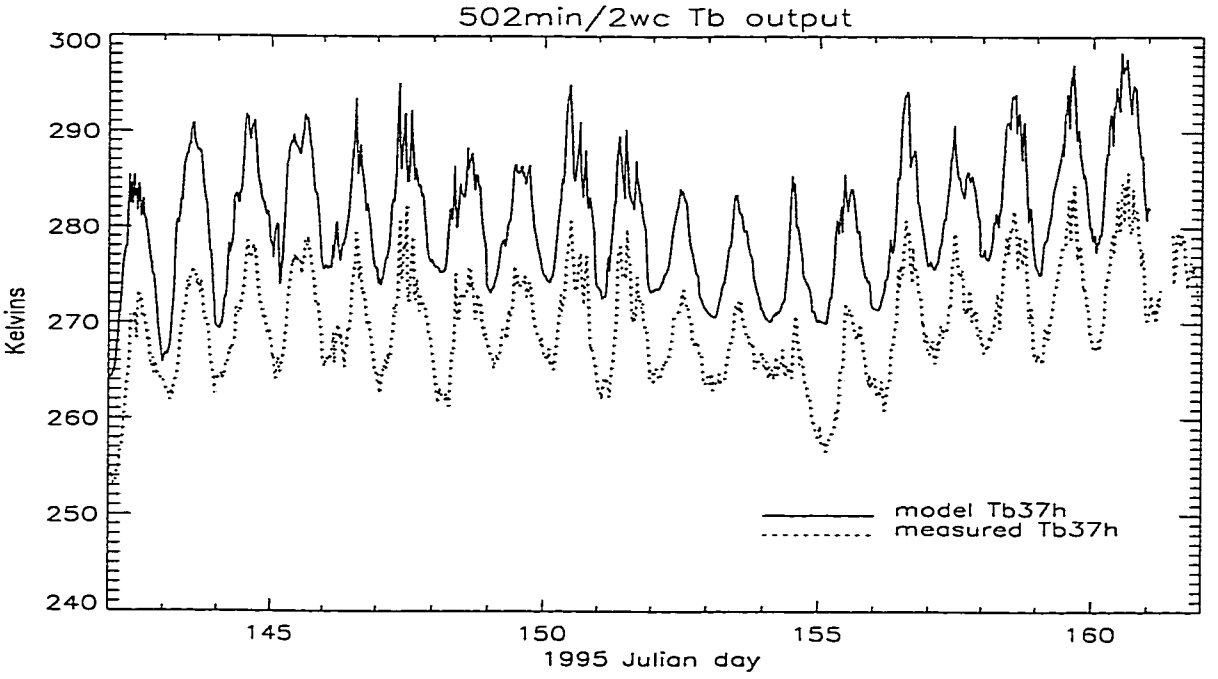

(b) 37 H

Figure 3.12: Predicted and observed 37 GHz V- and H-pol brightnesses.

channel	AD	SD
19 V	11.3	3.4
19 H	3.8	2.1
37 V	10.2	3.2
37 H	10.9	3.3

Table 3.5: Statistics of the differences between measured and predicted brightness temperatures in Kelvins (predicted - measured).

brightnesses are listed in Table 3.5. It should be noted that the cold calibration errors described in Chapter 2 would increase the AD values. Examination of the brightness components reveals that at 19 GHz 85–90 % of the predicted total brightness is the upwelling canopy brightness contribution. For 19H, 8 % of the total is contributed by the soil and 5 % by the downwelling canopy brightness reflected by the soil. The corresponding values for 19V are 2 % and 15 %. The modeled canopy attenuation is not polarization-dependent, so the lower 19H brightness vs. 19V brightness is due to the polarization-dependent transmissivity at the soil interface. At the SSM/I incidence angle, the difference is significant and the V polarization is near the Brewster angle. The model overpredictions of soil and canopy temperatures lead to overestimated effective emitting temperatures, which account for some of the difference—but not as much as the polarization effect. At 37 GHz, the greater canopy attenuation causes the upwelling canopy contribution to dominate, accounting for over 95 % of the total brightness. Consequently, the polarization effect is only slightly noticeable.

The R-module's assumption of a planar mineral soil boundary was realistic for the prairie case, but not for the tundra case. The uppermost tundra soil is highly porous peat—neither planar nor mineral. The brightness predictions are as close as they are only because of the nearly opaque vegetation layers.

Factors which were not considered in the modeling presented in this chapter include cooler inter-tussock valleys and cooler tussock faces as described earlier, an scatter darkening. All of these would lead to lower predicted brightnesses.

3.3 Summary

The tundra LSP/R model is a biophysically-based column model of heat and moisture fluxes within tundra vegetation and soil and between the tundra and the atmosphere coupled to a microwave emission model. It is an upgraded version of the original prairie LSP/R model, featuring true multi-layer soil capability, an adaptive time step with memory, corrected precipitation handling, and corrected handling of vegetation moisture in the microwave emission module.

Initial conditions are derived from a combination of field measurements and the temperature profile output from an annual model. The model was forced using REBEX-3 observed variables, including solar and net radiation, precipitation, humidity, wind speed.

In general, predicted soil and vegetation temperatures and moistures appear reasonable. The canopy temperatures compare favorably with REBEX-3 measurements, although subsurface temperatures were overpredicted in the thawed portion of the active layer. This was most likely due to incorrect thermal conductivities and/or the underestimation of heat loss by air convection and heat radiation from subsurface layers to the atmosphere.

The handling of precipitation in the canopy layer and the surface soil layer, plus infiltration into deeper soil layers all appear realistic. And, this is the first time that the LSP/R model has been operated with such high porosities, hydraulic conductivities, and highly organic soil textures. The model allows nearly instantaneous infiltration of precipitation, as would occur in the actual tundra peat.

Ice formation and thawing at the surface and at the freezing front appear realistic, with moisture being drawn to the front from above and below as long as the ice does not persist long enough for over-concentration to occur. Over-concentration only occurs when a freezing front persists. Surface ice formation is consistent with observed weather conditions at the site.

Model 19 and 37 GHz brightnesses clearly have the right basic shape and signature

compared to REBEX-3 observations. But the model overpredicts both the mean level and the amplitude of the diurnal variations. The majority of the predicted total brightness is the upwelling canopy brightness contribution. The model overpredictions of soil and canopy temperatures account for some of the differences, but the bulk of the difference must be due to unconsidered factors such cooler inter-tussock valleys and tussock faces within the field-of-view of the radiometers or scatter darkening.

CHAPTER 4

Comparison with SSM/I data

This chapter addresses the question of how well surface conditions in arctic tundra regions might be monitored using *satellite* radiobrightness observations. This can be done in a somewhat decoupled fashion from the comparison of ground-based observations and model predictions of radiobrightness presented in Chapter 3. For instance, if a land surface process/radiobrightness (LSP/R) model performs "well", its predictions would match those observed from a tower platform similar to TMRS2. But, there is no guarantee that satellite observations at their much larger spatial scale and with the possible effects of the intervening atmosphere will match as closely or even display a simple relationship in comparison with such ground measurements. Conversely, the satellite and ground-based observations might match very well, implying that satellite observations would be well-suited to the task, provided that the linkage between surface and near-surface conditions and microwave signatures is sufficiently well-understood.

One of the major products of this dissertation is a gridded SSM/I dataset suitable for comparison with the REBEX-3 ground radiobrightnesses. The comparison itself is presented in section 4.5. The sections following that explore calibration errors, timing differences, atmospheric effects, and topographic effects as explanations for the observed differences.

We shall begin with an overview of SSM/I instrument characteristics and DMSP satellite platform characteristics that are important for understanding the data preparation steps and the gridding technique—all of which affect the interpretation of the comparison.

Platform	F-10	F-11	F-13
Launch Date	1 Dec 1990	28 Nov 1991	24 Mar 1995
Information as of	2 Sep 95	2 Sep 95	Rev 1276
Inclination (deg)	98.8	98.8	98.8
Max. Altitude (km)	841	851	856
Min. Altitude (km)	728	844	844
Max. Swath Width (km)	1427	1483	Similar To F-11
Min. Swath Width (km)	1226	1414	Similar To F-11
Max. Incidence Angle (deg)	53.29	53.56	Similar To F-11
Min. Incidence Angle (deg)	52.10	53.16	Similar To F-11
Orbital Period (min)	100.5	101.9	102.0
Eccentricity	0.0078	0.00129	0.00083
Ascending Equator Crossing (Local Time)	22:09	18:25	17:43

Table 4.1: Selected DMSP platform-related SSM/I specifications.

freq. (GHz)	pol.	passband (MHz)	EFOV cross track (km)	EFOV along track (km)	NEΔT (K)	integ. time (msec)
19.35	V	10–250	43	69	0.43	7.95
19.35	H	10–250	43	69	0.41	7.95
22.235	V	10–250	40	60	0.67	7.95
37.0	V	100–1000	28	37	0.37	7.95
37.0	H	100–1000	29	37	0.37	7.95
85.5	V	100–1500	13	15	0.81	3.89
85.5	H	100–1500	13	15	0.74	3.89

Table 4.2: Selected SSM/I instrument-related specifications.

4.1 SSM/I overview

Special Sensor Microwave/Imager (SSM/I) is a passive microwave imaging instrument which flies aboard Defense Meteorological Satellite Program (DMSP) platforms. SSM/I instruments have been making earth observations since 1987 [36]. A summary of relevant instrument and platform specifications is given in Tables 4.1 and 4.2 [38, 64, 37].

The DMSP satellites fly in sun-synchronous polar orbits with staggered overflight times. Each completes 14.1 orbits per day, typically observing a given point on the earth twice per day. Poleward of 55 degrees latitude, the SSM/I swaths overlap, except for a small region at each pole (poleward of 87.6 degrees), as shown in Figure 4.1. For example, at the REBEX-3 latitude of ~69 degrees, each satellite makes typically 4–6 passes per day. These

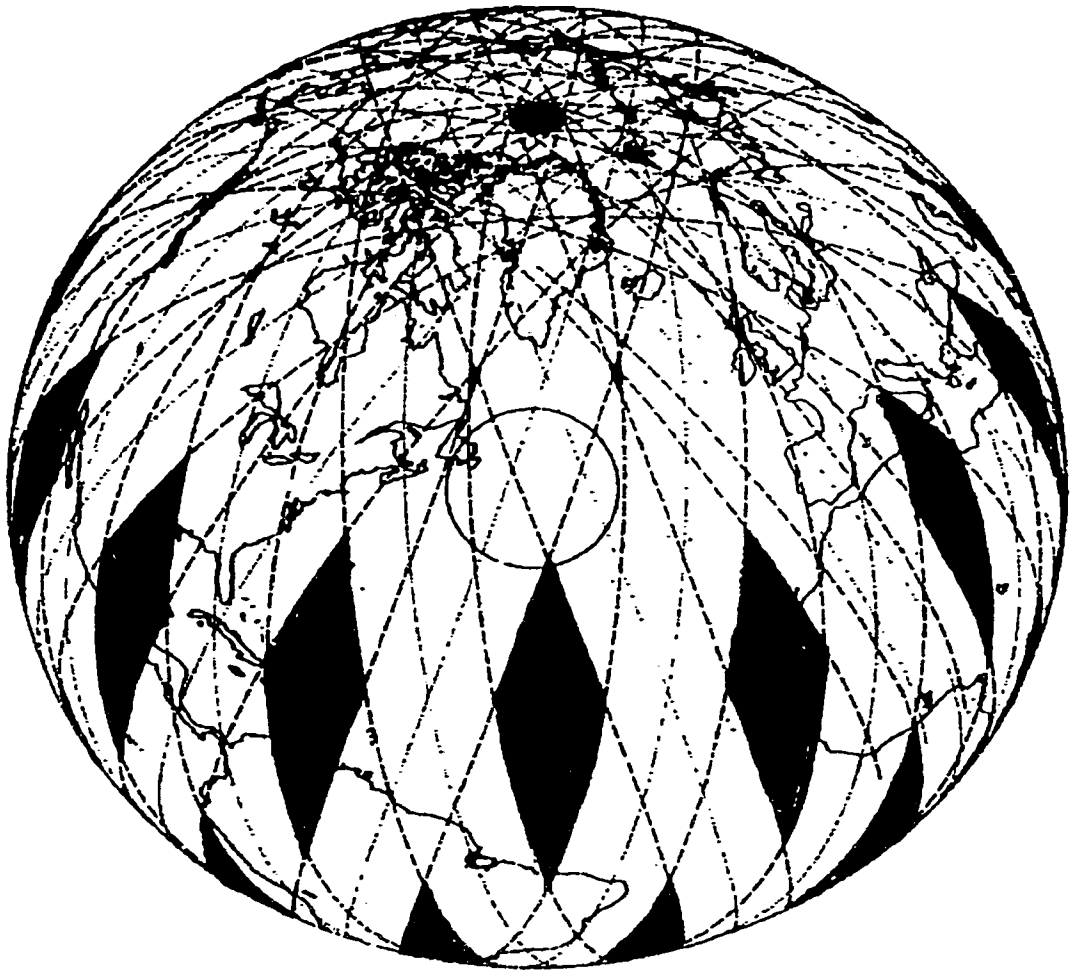

Figure 4.1: SSM/I swath coverage, from [65].

characteristics make the DMSP satellites excellent platforms for observing the arctic.

Three operational SSM/I instruments were in orbit during the REBEX-3 period aboard the F-10, F-11, and F-13 DMSP satellites. The F-10 satellite did not achieve the desired orbit. In terms of orbit parameters the F-10 eccentricity is an order of magnitude greater as compared with F-11 or F-13 [64], the perigee is approximately 15 % lower, and the local time of the ascending node (northbound equatorial crossing time) is not constant, increasing by 45 minutes per year. As a result, F-10 swath widths vary between 1226 and 1427 km

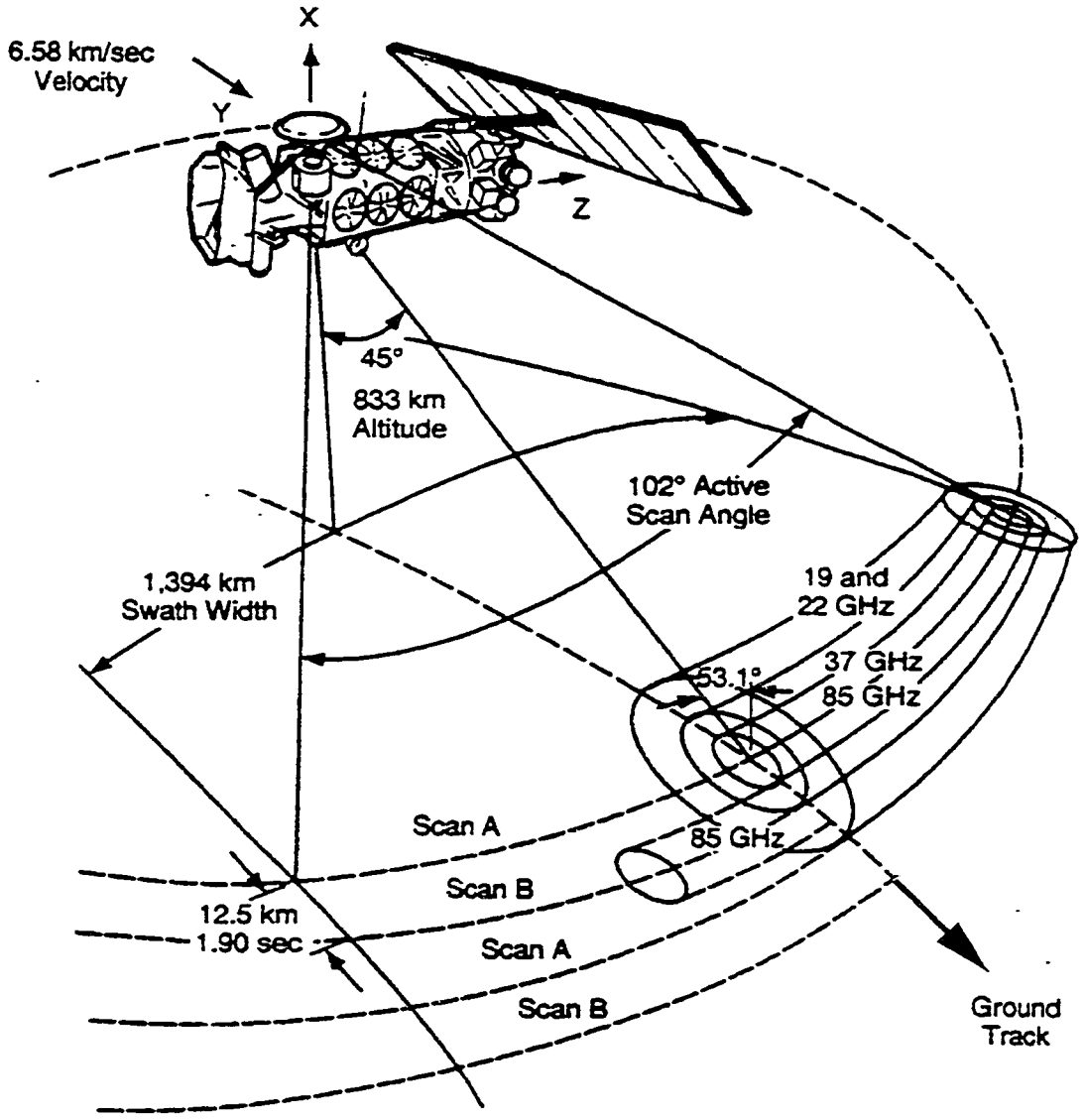

Figure 4.2: SSM/I scan geometry, adapted from [65].

with footprint dimensions varying by corresponding amounts. To avoid the effects of this "non-standard" orbit on the spatial resampling and gridding process, F-10 data were not used here.

F-11 and F-13 SSM/I Temperature Data Record (TDR) tapes were obtained from Marshall Space Flight Center Distributed Active Archive Center (MSFC DAAC). F-11 data were processed beginning with 1994 day 228 through 1995 day 273 (August 16, 1994 to September 30, 1995). F-13 data started to become available just before the REBEX-3 snow-free season in 1995. F-13 data were processed beginning with 1995 day 123 through day 273 (May 3–September 30, 1995). REBEX-3 ground brightness data span the period from 1994 day 241 to 1995 day 257 (September 14, 1995).

To conduct a fair comparison of REBEX-3 ground radiobrightness data and SSM/I data, we must consider those sources which might reasonably be expected to contribute to any differences. The sources expected to be responsible for the largest differences include calibration errors, non-stationary pixel effects as well as atmospheric, scaling, and topographic effects. I will attempt to quantify or bound each of these effects in turn in order to arrive at a measure of how well the SSM/I data and the REBEX-3 ground data match, the key results of this chapter. This should assist in the evaluation of how well surface conditions may be monitored from space.

Given that the footprint of the REBEX-3 tower radiobrightness data was approximately 2×4 meters and that the footprint of the resampled and gridded SSM/I data is 43×69 km, it seems very reasonable to limit the "analyses" to simple comparisons. More sophisticated analyses or "corrections" would require additional data on regional meteorological or surface conditions which were not available during REBEX-3, and which generally would not be available for such a remote area. For example, the location nearest the REBEX-3 site for which regular atmospheric sounding data are available is Barrow, Alaska, some 400+ km distant, and located within a different (coastal) climate zone.

4.2 Spatial fidelity of data

4.2.1 Problem: non-stationary pixels

While the conical scan geometry of SSM/I is convenient in that it provides observations made at a constant incidence angle and pixels of constant size and shape, it does not generate a convenient coordinate system for pixels on the earth's surface. Raw swath pixels fall along a series of circular arcs (Figure 4.2) at regularly-spaced intervals of 25 km for the non-85 GHz channels, and 12.5 km for the 85 GHz channels [38].

The actual swath pixel locations relative to a fixed location such as the REBEX-3 site are not constant on a daily or sub-daily basis, nor between the overlapping portions of two successive orbits. The standard DMSP orbit does have a repeat time of 16 days (interval between orbits with identical swath coverage), so *swaths* repeat to some level of accuracy. But, even for repeated swaths, the constituent *pixel* locations would differ. The use of data from multiple satellites further complicates matters. Such non-stationary pixels would only represent an unwanted variable in any comparison of SSM/I and REBEX-3 ground data. The REBEX-3 site was within 20–30 km of the Brooks Range, so the combination of footprint size and non-stationary location could result in pixels "contaminated" with variable brightness contributions from mountains. Other sites of future interest were within 10 km of the Arctic Ocean coastline with its potentially severe transition between low water brightness values and high land brightness values. Still other sites were located near transitions from the coastal plain to higher-elevation areas with different vegetation and moisture conditions.

4.2.2 Solution: EASE-Grid

The solution to the problem of non-stationary pixels was to resample the SSM/I data from the swath reference frame to a fixed grid. The Equal-Area Scalable Earth Grid (EASE-Grid) is a standard gridding scheme now used with a variety of datasets [9], including SSM/I data, its original application. The SSM/I EASE-Grid is composed of (1) map projection

definitions and a gridding scheme [50] and, (2) a specific method to interpolate SSM/I data from swath space to earth gridded coordinates. The two standard EASE-Grid projections are a polar azimuthal equal area projection and a cylindrical equal area projection. The latter is primarily suited for studying mid-latitude and low-latitude areas, while the former is ideal for studying high-latitude and polar areas. All the projections are based on a spherical model of the Earth with radius R = 6371.228 km. This is the value which corresponds to a sphere with the same surface area as an ellipsoid using the International Datum. The standard grid cell size is 25 × 25 km, but a 12.5 × 12.5 km cell size can also be used with data from the higher-resolution 85 GHz channels. Few cells have these exact dimensions, but all cells have the same area. Figure 4.3 shows an example of one day's worth of SSM/I ascending pass data displayed in all three EASE-Grid projections: north polar, south polar, and cylindrical.

For arctic areas, the north polar projection is preferred. The transformation from latitude-longitude coordinates to row-column coordinates for the 25 km north polar EASE-Grid is given by the following set of equations [67]:

$$col = \frac{2R_{\oplus}}{C}(\sin\phi)\,\sin(\pi/4 - \theta/2) + col0 \tag{4.1}$$

$$row = -\frac{2R_{\oplus}}{C}(\cos\phi)\,\sin(\pi/4 - \theta/2) + row0 \tag{4.2}$$

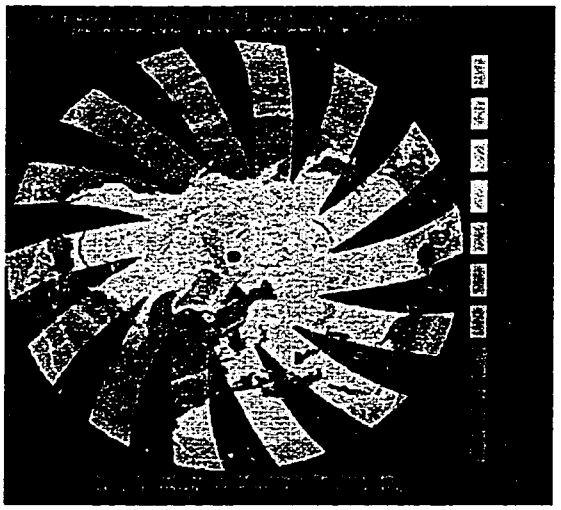

(a) north polar

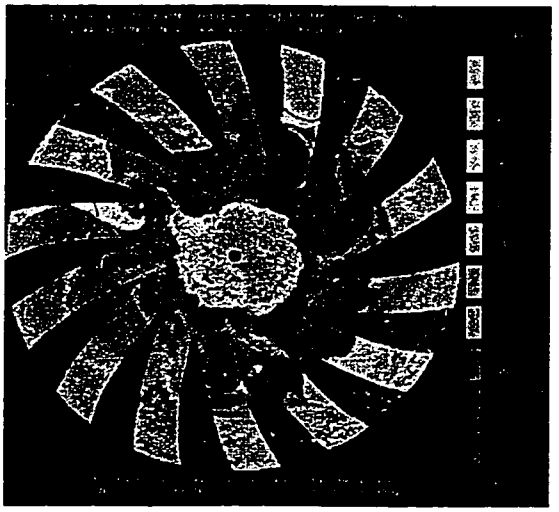

(b) south polar

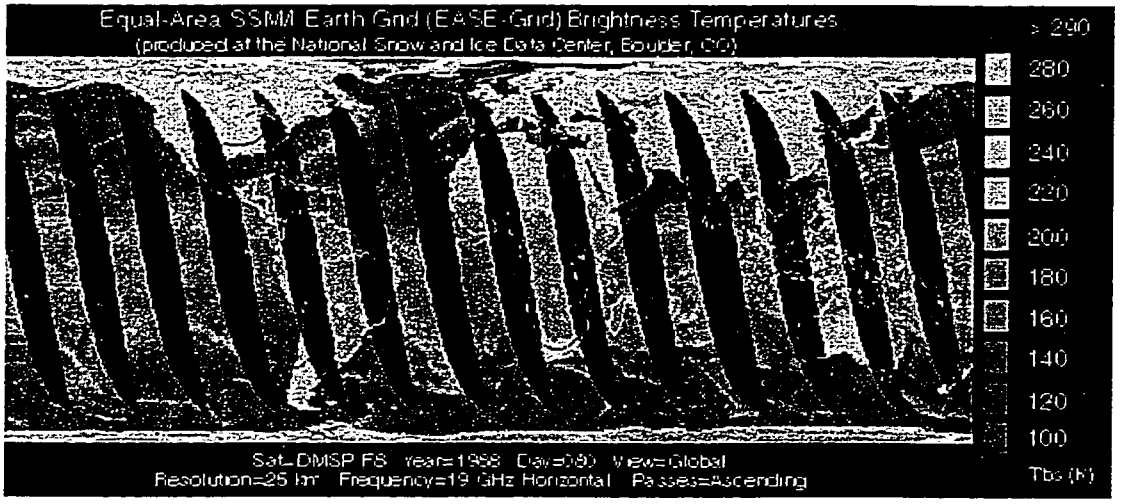

(c) cylindrical

Figure 4.3: One day's worth of ascending passes displayed in all three EASE-Grid projections.

where:

col = column coordinate (0–720)

row = row coordinate (0–720)

ϕ = longitude in radians

θ = latitude in radians

$R_{\oplus}$ = radius of the Earth = 6371.228 km

C = nominal cell size = 25.067525 km

$col0$ = column coordinate of map origin = 360.0

$row0$ = row coordinate of map origin = 360.0.

Row-column grid *cell* numbers are obtained by rounding the row-column *coordinates* up at .5. Thus, grid cell (i, j) includes the area $i - .5 \leq row < i + .5$ and $j - .5 \leq col < j + .5$ with its center at coordinates (i, j). For example, the REBEX-3 site at 68.763 N, 148.882 W has EASE-Grid coordinates of (279.81,311.59), which fall inside grid cell (280,312). For my purposes, the terms "cell" and "pixel" are interchangeable.

It is worth pointing out that the projection and gridding schemes are independent of the type of data or the particular satellite sensor. For example, EASE-Grid is also used with Scanning Multichannel Microwave Radiometer (SMMR) and Advanced Very High Resolution Radiometer (AVHRR) data and even ground data [8]. The grid cell sizes may differ, but the grids are all co-registered so inter-sensor comparisons are facilitated. Only the SSM/I EASE-Grid is discussed here, so it will be understood hereinafter that "EASE-Grid" refers to the SSM/I EASE-Grid except where specificity with respect to SSM/I is important.

4.2.2.1 Resampling scheme: modified Backus-Gilbert optimal interpolation

The spatial interpolation scheme employed with the SSM/I EASE-Grid utilizes modified Backus-Gilbert optimal interpolation [5], based on the work of Galantowicz and England [28] which, in turn, is based on the earlier work of Poe [75], and Stogryn [85]. The interpolation

is optimal in the sense that an interpolated value for a particular location approximates the value which would have been obtained if the sensor had observed that location directly. A detailed description of the resampling technique has been given by Galantowicz [28, 26] and Poe [75], so only an overview is presented here.

In the EASE-Grid implementation, actual SSM/I antenna patterns were used to generate the weighting coefficients for combining swath pixel brightnesses to form interpolated brightnesses. Coefficients were tabulated for interpolation points that form a grid with a density 16 times that of the original swath pixel spacing in the swath reference frame (i.e., a grid spacing of 6.25 km for the 19, 22, and 37 GHz channels, and 3.125 km for the 85 GHz channels).

From this densified array, the brightness value of the point closest to the center of the desired EASE-Grid cell is re-registered to that EASE-Grid cell location and used as the brightness value for that cell. This method of assigning interpolated values has two notable features. First, the original swath data are not temporally or spatially averaged as is the case with the "drop-in-the-bucket" method used in another SSM/I gridded product[1]. This was a design requirement of the EASE-Grid in order to preserve temporal and spatial fidelity [4]. Second, the use of a finite-spacing densified grid (rather than interpolating exactly to each EASE-Grid point) provides significant computational savings. The weighting coefficients need be computed only once since the basic SSM/I scan geometry is consistent. The current EASE-Grid processors rely on pre-tabulated values. For a densified grid spacing of 6.25 km, the maximum re-registration distance is about $\sqrt{2}/2 \times 6.25 = 4.4$ km or 10% of the 19 GHz effective field-of-view and less than the 10 km maximum geolocation error for swath pixels cited by Wentz [101].

To make the brightness values for the different SSM/I channels represent observations from the same footprints, EASE-Grid standardizes the footprints of all channels to match

[1]The "DMSP SSM/I Brightness Temperature Grids"[66], which cover only polar regions and use daily (24 hour) average data.

that of the 19 GHz V-polarized channel. So, although the data presented in a "low-resolution" EASE-Grid *image* are displayed on a 25 km grid, and the brightness values are depicted with square 25 × 25 km pixels, the actual *resolution* of each pixel is that of the 19V channel (43 × 69 km). [The Backus-Gilbert technique also permits limited spatial resolution enhancement at the expense of radiometric (i.e., amplitude) accuracy. Thus, for example, the resolution of the 19 GHz swath pixels could be increased, but the entire image would suffer from increased noise resulting from this process.] NSIDC also processes the 85 GHz swath data into an EASE-Grid product using a 12.5 km grid to retain the higher resolution available from the 85 GHz channels.

4.3 Obtaining maximum temporal fidelity

4.3.1 Problem: discarded pixels

The previous discussion presented the case for EASE-Grid as a solution to the problems associated with using non-stationary pixels in a comparison with observations from fixed points. Through the NOAA/NASA Pathfinder Program, NSIDC produces CD-ROMs containing SSM/I brightness data in EASE-Grid form [67]. However, the CD-ROMs for the REBEX-3 period were not available at the time the present comparison study was conducted. Furthermore, even if they had been available, the CD-ROMs would have contained daily images just like those in Figure 4.3. These are generated from swath data which overlaps at high latitudes, resulting in a maximum of two data points for a given earth location per channel per satellite per day since EASE-Grid discards overlapping pixels rather than averaging them.

This no-averaging choice preserves the temporal fidelity of the SSM/I data. Without it, observations taken hours apart could be combined into a single data point, and any diurnal signal in the observations would be partly filtered out. As mentioned earlier, for locations at the latitude of the REBEX-3 site (69 N), SSM/I observations are made 4–6 times per satellite per day. And, since I was interested in examining the satellite observations at

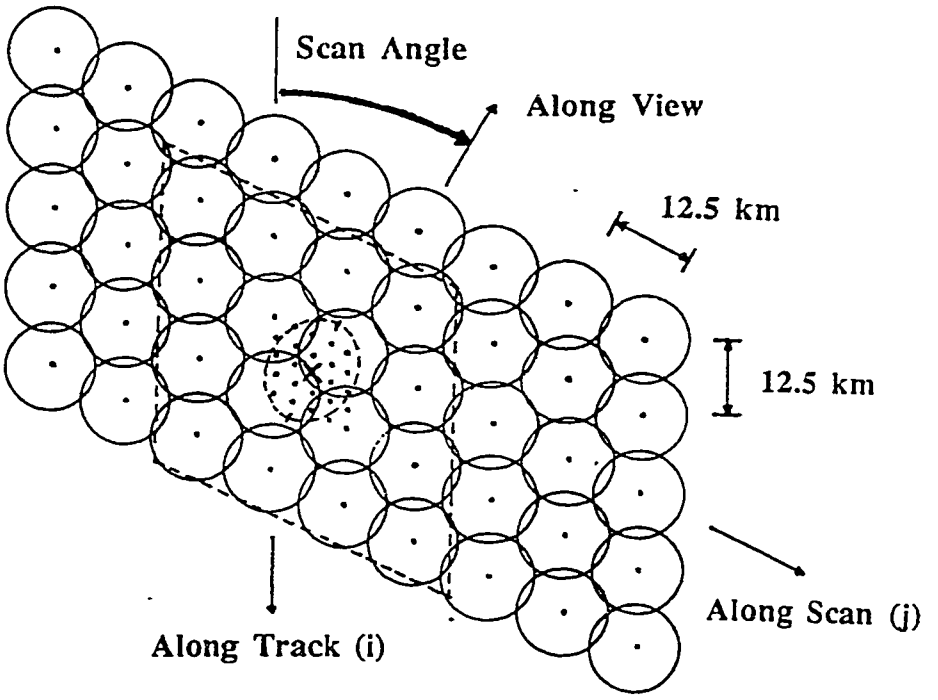

Figure 4.4: A portion of 5 consecutive scans is shown. Circles represent raw swath pixels (note: actual footprints are not circles). Weighted brightness values from the 16 pixels within the dashed box are combined to generate interpolated observations on the densified grid. The dashed oval represents the footprint of the desired resampled observation, with the 'X' marking the center. The data from the nearest-neighbor pixel on the densified grid is re-registered to the EASE-Grid cell located at 'X'. From [28] with permission.

the highest possible temporal resolution (to look at diurnal signals, for example), retaining *every* observation was important.

4.3.2 Solution: a custom EASE-Grid processor

The obvious solution was to perform EASE-Gridding on one orbit's worth of data at a time, avoiding the overlapping swath problem. Unfortunately, NSIDC's operational EASE-Grid processor (referred to here as the "standard" processor) is not configured to operate in this mode. But, a "custom" EASE-Grid processor could provide the solution.

A major by-product of this dissertation was the development of exactly such a "custom" processor: an automated customizable software package for generating EASE-Grid data from readily-available low-cost swath data in Temperature Data Record (TDR) format [49]. This software package is now publicly downloadable for use by the entire SSM/I user community.

The TDR data used here were obtained from the NASA MSFC DAAC, now closed. Basic quality control checks (out-of-bounds and along-scan bias corrections) were performed on these data prior to EASE-Grid processing, utilizing programs provided on the tapes [62, 101] and updated information [41].

The custom processor splits full orbits into individual ascending and descending orbit segments prior to processing, so that no overlapping data is discarded [72]. For consistency, the core modules which implement the Backus-Gilbert resampling are the exact resampling modules from the standard processor itself.

The TMRS2 85 GHz radiometer experienced temperature control problems during much of the experiment, so the REBEX-3 85 GHz observations are not as accurate as those from the 19 and 37 GHz channels. And, adding 85 GHz capability to the custom processor would have required substantial extra effort due to the different 12.5 km grid. So, for simplicity, the 85 GHz SSM/I data were not EASE-Gridded.

Furthermore, atmospheric opacity at 85 GHz is several times the opacity at 19 and

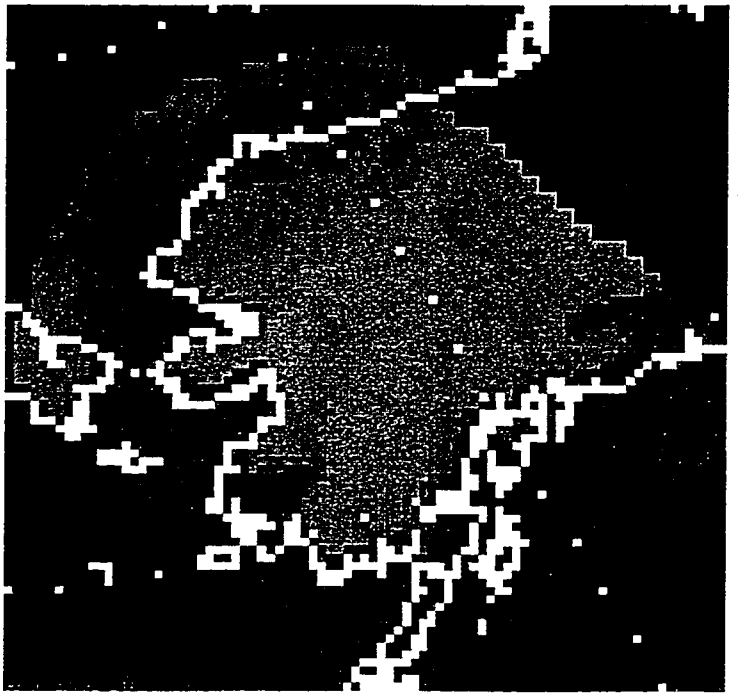

Figure 4.5: An example of custom EASE-Grid processor output zoomed to the region of interest. F-13, 19V channel, 1995 day 154, ascending pass.

37 GHz for identical conditions [92]. As a result, satellite observations with the 19 and 37 GHz channels more nearly represent surface conditions than do 85 GHz observations. So, there was insufficient potential advantage at this time vs. the additional complexity of incorporating the 85 GHz data in the processing. Of course, the 85 GHz *swath* (pre-EASE-Grid) data for the vicinity of the REBEX-3 site were subsetted and archived along with the swath data for the other channels. A more sophisticated future study which accounts for the above-mentioned effects might benefit from the increased spatial resolution achievable at 85 GHz.

A total of 3101 SSM/I orbit files from the F-11 and F-13 satellites were processed for the comparison studies in this chapter. An example EASE-Grid image processed using the custom processor is shown in Figure 4.5.

4.3.3 Other calculations

Additional features were incorporated into the custom EASE-Grid processor specifically for use in studying REBEX-3 SSM/I data. These include the ability to filter both pre-EASE-Grid (swath) and post-EASE-Grid data down to individual pixels or groups of pixels, and for swath data, to calculate the direction the SSM/I sensor was pointing in when a pixel was observed as well as the distance from each filtered pixel to a fixed site. Descriptions of these sensor look direction (SLD) and distance to site (DTS) calculations follow.

4.3.3.1 Sensor look direction

Sensor look direction is a needed precursor for the DTS calculations. SSM/I makes surface observations along a 102.4-degree segment of its conical scan symmetric about the satellite ground track (the imaginary line on the earth's surface traced by the subsatellite point). Thus, the sensor look directions for pixels along one scan range ± 51 degrees with respect to the ground track bearing (the direction of flight drawn on a map with due north = 0, due east = 90, etc.). 'A' scans and 'B' scans are interlaced, spaced 12.5 km apart in the along-track direction as depicted in Figure 4.6. Co-boresighted data for all 7 SSM/I channels (see Fig. 4.2) is recorded at 64 locations along each 'A' scan, so pixels are spaced 1.6 degrees apart. Additional readings are made using only the 85-GHz channels midway between the 'A'-scan pixels and at 128 locations along each 'B' scan. So 85-GHz swath pixels are spaced 12.5 km apart along-track and along-scan, and the corresponding number for the other channels is 25 km.

The footprints of the swath pixels are oval-shaped, with the long axis along the sensor look direction. The interpolated EASE-Grid footprints are likewise not circularly symmetric, and thus they have an orientation related to the sensor look direction [28]. Poe [75] shows several comparisons of swath ("true") vs. interpolated footprints. One artifact of the standard EASE-Grid processing is that the sensor look direction associated with the data in a particular grid cell is not explicitly retained. So even with gridded brightness values,

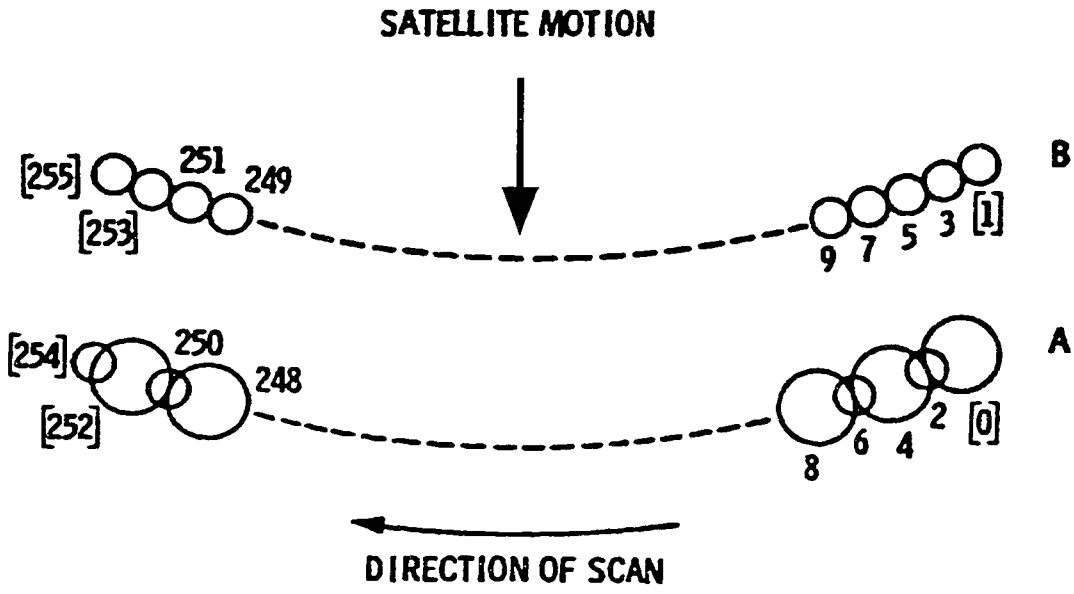

Figure 4.6: SSM/I A/B scan geometry. Numbers indicate pixel indexing in the swath reference frame. Large circles–all channels. Small circles–85 GHz channels only. Adapted from [66].

there is a remaining possible variation. Analyzing the precise effects of this variation is beyond the scope of this comparison, however it might be the source of some of the observed differences.

The sensor look directions for EASE-Grid pixels can be reconstructed *ex post facto* using the time tag associated with the pixel, however since the along-track satellite velocity is 6.58 km/sec and the along-scan time interval between pixels is 4.22 milliseconds, this would require an orbit model to achieve reasonable accuracy. An alternate scheme for determining sensor look direction using only the pixel geolocations (supplied on the original data tapes) without time tags provided sufficient accuracy.

4.3.3.2 Distance to site

Once the sensor look direction is determined for a given swath pixel, the distance from the pixel to a fixed point such as the REBEX-3 site can be trivially found. The distance to site and the sensor look direction are needed during the comparison of swath and EASE-Grid data.

4.4 Swath vs. EASE-Grid comparison

The final item to consider before comparing satellite and ground radiobrightness observations, and a worthwhile comparison in its own right, is the accuracy of the interpolated EASE-Grid brightness values. We wish to compare brightnesses from swath pixels in the vicinity of the REBEX-3 site (some include the site itself) with brightness values for the EASE-Grid cell (280,312) which includes the REBEX-3 site. The comparison includes the five low-frequency channels, but not the 85 GHz channels for reasons described earlier.

It is difficult to formulate a rigorous comparison. On the one hand, swath pixels represent observations from moving locations, the footprint orientation varies, and the footprint size varies with frequency. On the other hand, an EASE-Grid pixel has a fixed size and a fixed center location (to within the maximum re-registration distance), although there is a

remaining variation of the footprint orientation.

Because we will always be comparing EASE-Grid pixels to the swath pixels they were derived from, both sets of pixels represent brightnesses for the same time (to within seconds). Thus, there are two factors which we can ignore. First, any geolocation error should displace the coordinates of both sets of pixels by the same amounts in the same directions, effectively removing geolocation errors as a consideration in this comparison. Second, the orientation of the semi-major axes of both sets of footprints will be parallel to within 4.8° (3× along-scan pixel spacing, the maximum difference within any 4 × 4 group of swath pixels), an insignificant difference here.

We are left with two variables to consider: d, the distance between the center of a swath pixel and the center of EASE-Grid cell (280,312), and the size of the swath pixel based on the SSM/I channel (from Table 4.2). The maximum re-registration distance of 4.4 km is constant.

Let $T_B(\theta, \phi, t)$ represent the brightness of a swath pixel at latitude θ, longitude ϕ, and time t, and let $T_B(r, c, t)$ represent the brightness of the nearby (in space and time) derived EASE-Grid pixel at row r, column c, and interpolated time $\hat{t}$. Since $\hat{t} \simeq t$ to within seconds, I will simply use t to denote both swath and interpolated times. Scatter diagrams of $T_B(r, c, t)$ vs. $T_B(\theta, \phi, t)$ are shown in Figures 4.7 and 4.8 for the five low-frequency channels for F-11 and F-13, respectively. The high R^2 values indicate a very strong linear correlation between EASE-Grid and spatio-temporally matched swath pixels. The slightly lower F-13 R^2 values most likely reflect the mid-experiment F-13 turn-on date and the consequently smaller overall range of T_B values.

The comparisons are intended to represent brightnesses from the same areas on the ground. The spatial selection criterion for swath pixels was any pixel whose footprint was within the potential footprint of EASE-Grid cell (280,312). The potential footprint is the area potentially "observed" by the footprint of the EASE-Grid pixel including the re-registration distance. We make one simplification for computational convenience: instead

channels	$r(f)$ (km)	d (km)
19 H,V	27.2	4.4
22 V	24.5	7.1
37 H,V	16.2	15.4

Table 4.3: Center-to-center pixel distances (km) for Figures 4.7 and 4.8.

of treating the footprints as ellipses, we treat them as circles with equivalent areas—let $r(f) = \sqrt{a(f)b(f)}$ be the radius of a circle having the same area as an ellipse with semi-minor radius $= a$ and semi-major axis $= b$ (see Table 4.2). There is sufficient overlap that the comparisons should not be significantly affected.

With this simplification, the radius of the potential footprint is $r(19) + 4.4 = 31.6$ km. The maximum distance between the nominal center of an EASE-Grid pixel and the center of swath pixels enclosed by the potential footprint of the EASE-Grid pixel is then $d = r(19) + 4.4 \text{ km} - r(f)$, where $r(f)$ is the radius of a swath pixel at frequency f. Values of $r(f)$ and d are listed in Table 4.3.

For each SSM/I channel, we define the mean brightness difference as

$$\overline{\Delta T_B} = \frac{1}{N}\sum_{t=t_1}^{t_N}(T_B(r,c,t) - T_B(\theta,\phi,t)) \tag{4.3}$$

and the standard deviation of the difference as

$$\sigma_{\Delta T_B} = \left[\frac{1}{N-1}\sum_{t=t_1}^{t_N}(T_B(r,c,t) - T_B(\theta,\phi,t) - \overline{\Delta T_B})^2\right]^{1/2} \tag{4.4}$$

where N is the number of swath-EASE-Grid pairs compared, and $t = t_1, \ldots, t_N$ are the observation times. The mean of the EASE-Grid brightnesses alone is

$$\overline{T_{B,eg}} = \overline{T_B(r,c,t)} = \frac{1}{N}\sum_{t=t_1}^{t_N} T_B(r,c,t). \tag{4.5}$$

The standard deviation of the EASE-Grid brightnesses alone is

$$\sigma_{T_{B,eg}} = \left[\frac{1}{N-1}\sum_{t=t_1}^{t_N}(T_B(r,c,t) - \overline{T_B(r,c,t)})^2\right]^{1/2}. \tag{4.6}$$

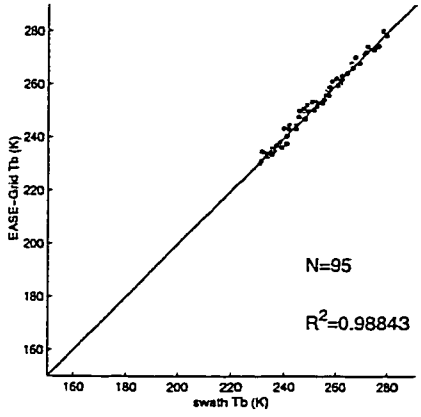

(a) 19V

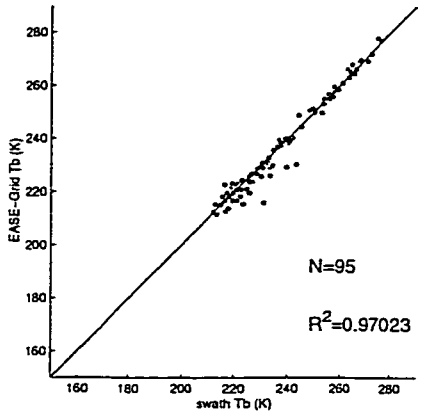

(b) 19H

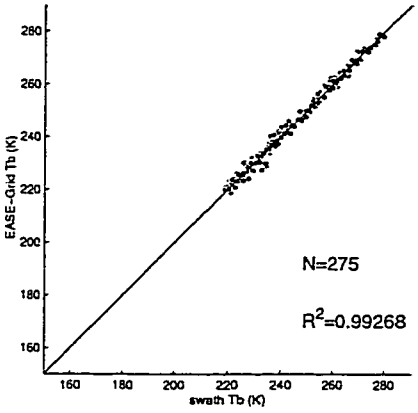

(c) 22V

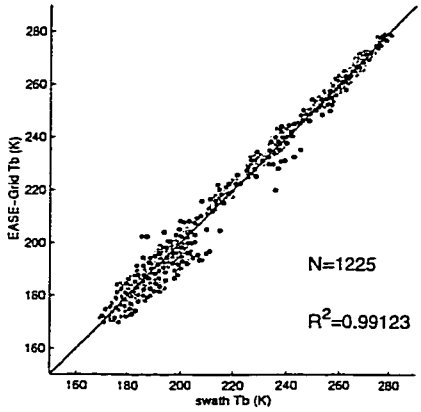

(d) 37V

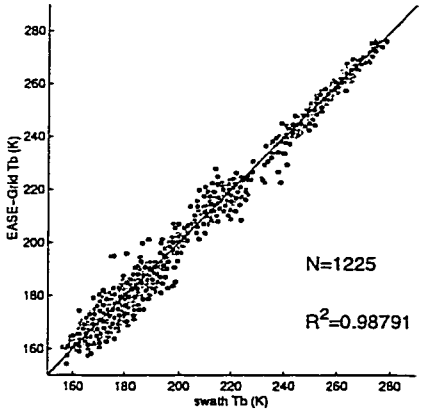

(e) 37H

Figure 4.7: F-11 swath vs. EASE-Grid brightnesses.

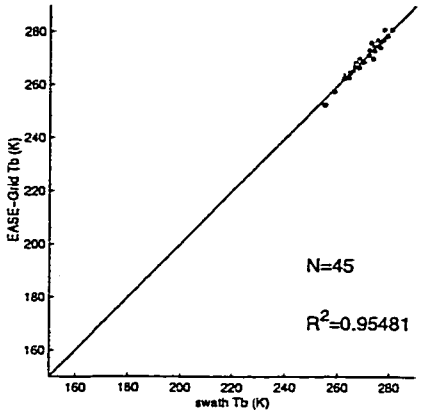

(a) 19V

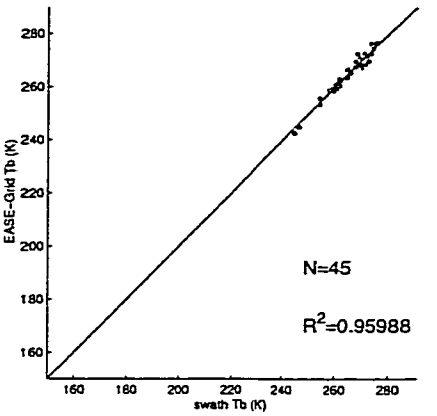

(b) 19H

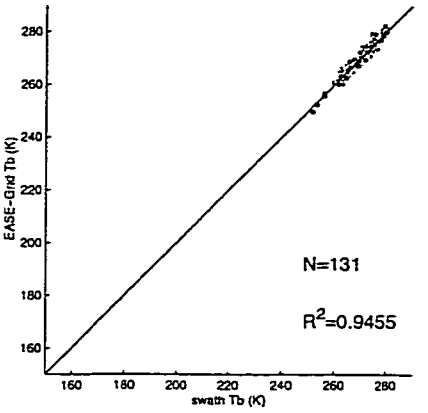

(c) 22V

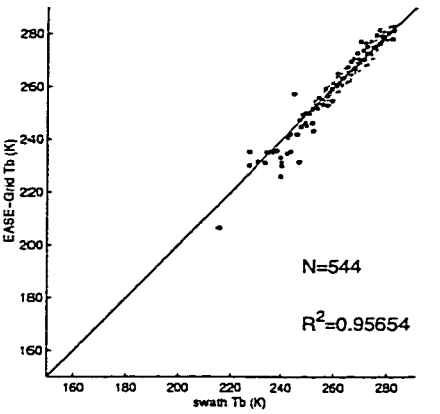

(d) 37V

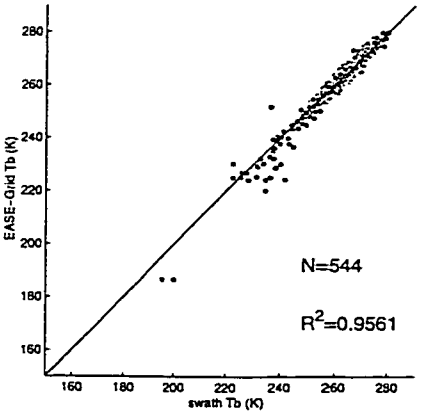

(e) 37H

Figure 4.8: F-13 swath vs. EASE-Grid brightnesses.

a	b	c	d	e	f	g	h	i
channel	satellite	N	$\overline{\Delta T_B}$ (K)	$\sigma_{\Delta T_B}$ (K)	$\overline{T_{B,eg}}$ (K)	$\overline{T_{B,sw}}$ (K)	$\sigma_{T_{B,eg}}$ (K)	$\sigma_{T_{B,sw}}$ (K)
19V	F-11	95	0.41	1.44	251.78	251.37	13.40	13.33
19V	F-13	45	0.09	1.29	269.93	269.84	6.00	5.68
19H	F-11	95	-0.65	3.23	237.63	238.28	18.57	17.86
19H	F-13	45	0.18	1.51	265.03	264.84	7.42	7.02
22V	F-11	275	0.26	1.47	246.88	246.62	17.03	17.17
22V	F-13	131	0.29	1.43	269.13	268.84	6.07	5.70
37V	F-11	1225	0.14	3.23	222.46	222.33	34.43	34.36
37V	F-13	544	0.13	2.16	266.38	266.25	9.86	8.98
37H	F-11	1225	-0.25	4.14	211.88	212.12	37.57	37.53
37H	F-13	544	0.06	2.50	261.66	261.60	11.32	10.30

Table 4.4: Swath vs. EASE-Grid brightness comparison.

The mean of the swath brightnesses alone is

$$\overline{T_{B,sw}} = \overline{T_B(\theta,\phi,t)} = \frac{1}{N}\sum_{t=t_1}^{t_N} T_B(\theta,\phi,t). \tag{4.7}$$

And, the standard deviation of the swath brightnesses alone is

$$\sigma_{T_{B,sw}} = \left[\frac{1}{N-1}\sum_{t=t_1}^{t_N}(T_B(\theta,\phi,t) - \overline{T_B(\theta,\phi,t)})^2\right]^{1/2}. \tag{4.8}$$

$\overline{\Delta T_B}$, $\sigma_{\Delta T_B}$, $\overline{T_{B,eg}}$, $\overline{T_{B,sw}}$, $\sigma_{T_{B,eg}}$, and $\sigma_{T_{B,sw}}$ for the cases depicted in Figs. 4.7 and 4.8 are listed in Table 4.4 for the 5 SSM/I channels processed with the custom EASE-Grid processor. The excellent match between comparable quantities (columns f & g, h & i) and the low values of $\overline{\Delta T_B}$ and $\sigma_{\Delta T_B}$ (columns d & e) are indications that the gridded data are an accurate representation of the swath data.

4.5 Satellite vs. ground observations

Now that we have established the accuracy of the EASE-Grid brightnesses, we can compare $T_{B,eg}(t)$, the combined EASE-Grid brightnesses for F-11 and F-13 for the REBEX-3 cell (280,312) at time t, to the TMRS2 tower brightness observations at time t', $T_{B,tmrs}(t')$. This will allow us to evaluate how well SSM/I observations can be used to estimate the tundra microwave signature. Figures 4.9(a) and 4.9(b) show that $T_{B,eg}(t)$ and $T_{B,tmrs}(t')$

chan	77K	200K	300K
19V	-22.4	-6.3	6.8
19H	-39.9	-9.5	15.2
37V	-33.9	-8.1	12.8
37H	-39.9	-8.0	17.9

Table 4.5: EASE-Grid vs. TMRS2 brightnesses, no adjustments.

were generally very similar during the yearlong field experiment.

In both cases, the onset of snow accumulation is clearly marked by the divergence of the various channel brightnesses around day 250. The large fluctuations around days 475-510 reflect the melting and refreezing of snow during snowmelt. These features are consistent with snowpack signatures reported in the literature [78, 92].

Again, in this dissertation, I am interested in the snow-free period. The distinguishing signature of snow-free tundra is the nearly equal brightnesses observed for all channels.

Scatter diagrams of $T_{B,tmrs}(t')$ vs. $T_{B,eg}(t)$ corresponding to the four paired channels shown in Figures 4.9(a) and 4.9(b) are shown in Figure 4.10. The dotted lines are the best-fit lines in the least-squares sense. The difference in $T_{B,tmrs}$ (y-axis difference) between the best-fit line and the 1:1 line for $T_{B,eg}$ (x-axis) values of 77, 200, and 300 K for each channel is listed in Table 4.5. The high R^2 values indicate strong linear relationships and the closeness of the absolute match (closeness to the 1:1 line) before accounting for calibration errors or atmospheric or topographic effects. The outliers ($T_{B,tmrs} \gg T_{B,eg}$), most visible in Figures 4.10(c) and 4.10(d) represent times during snowmelt when the snow at the REBEX-3 site had melted several days before the snow across the whole EASE-Grid pixel. This early melt is typical for areas within a few hundred meters of the pipeline road due to windblown road dust.

The implications of such a strong linear relationship between the TMRS2 and SSM/I observations deserve some consideration.

The four-order-of-magnitude difference in footprint sizes between TMRS2 and SSM/I makes the degree of matching remarkable. I know of no other examples of either a compari-

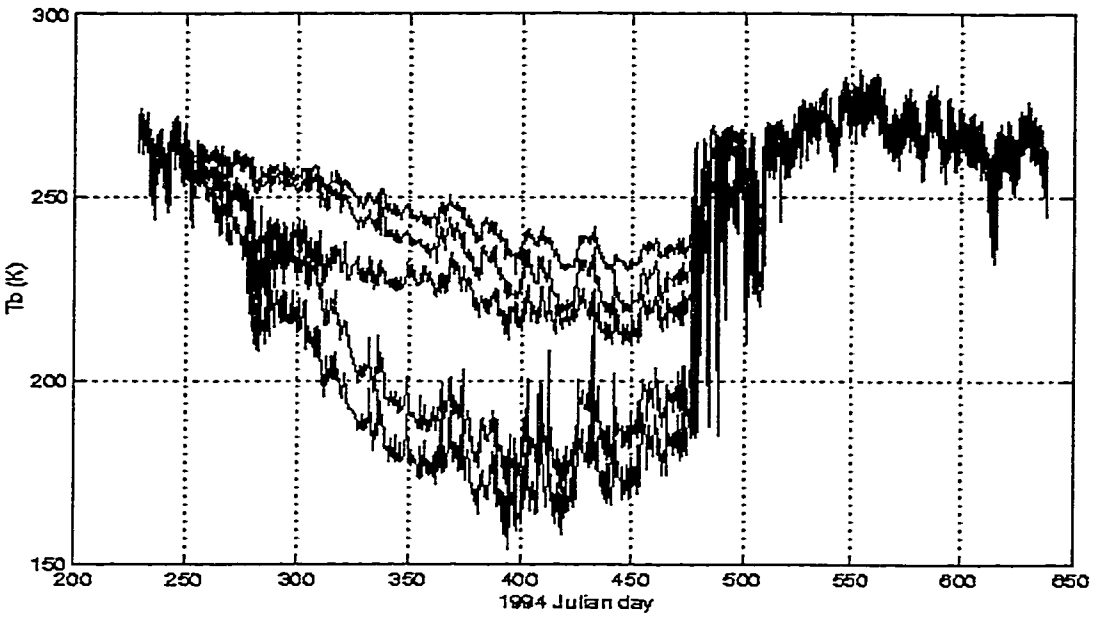

(a) EASE-Grid

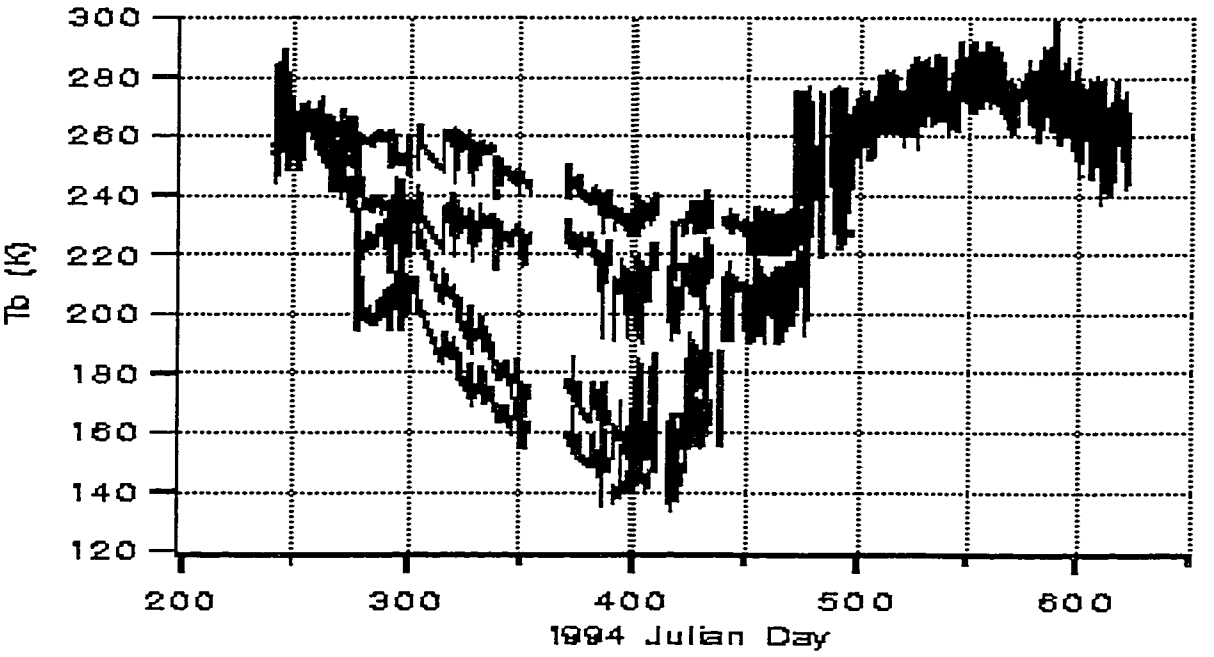

(b) TMRS2

Figure 4.9: REBEX-3 SSM/I (EASE-Grid) and TMRS2 brightnesses, no adjustments, 9/94–9/95. (upper panel) EASE-Grid: top to bottom, channels are 19V, 22V, 19H, 37V, 37H. (lower panel) TMRS2: top to bottom, channels are 19V, 19H, 37V, 37H.

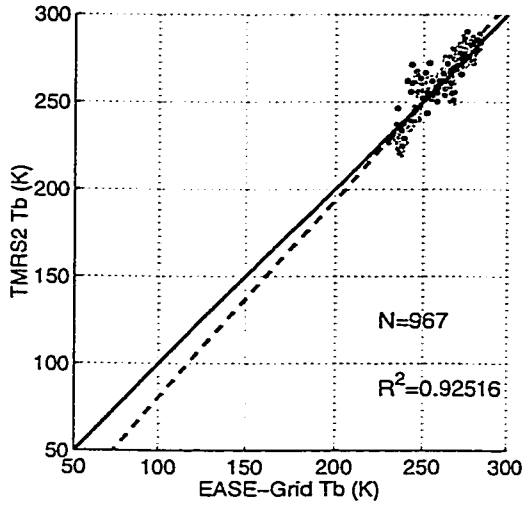

(a) 19V

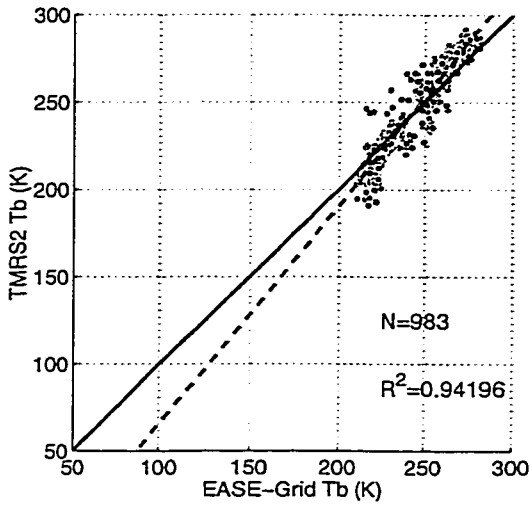

(b) 19H

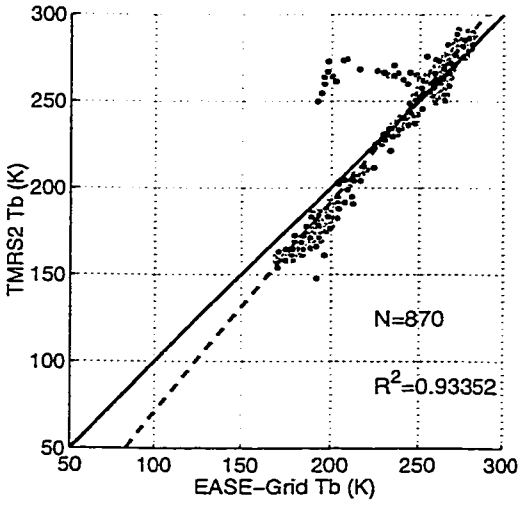

(c) 37V

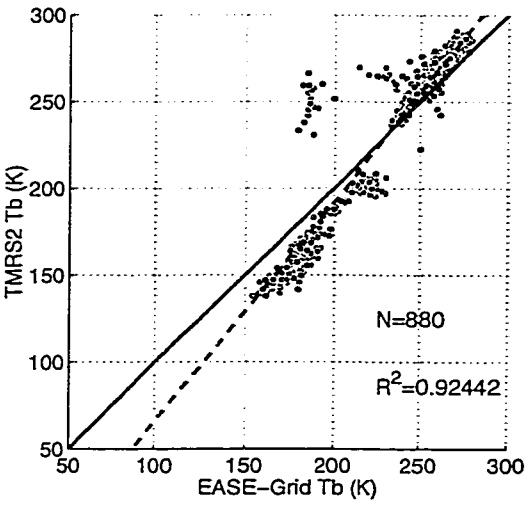

(d) 37H

Figure 4.10: EASE-Grid vs. TMRS2 brightnesses, no adjustments. Solid lines are 1:1 lines, dotted lines are best linear fits to scatter points.

son or such a regular and consistent match between surface (or aircraft) and satellite passive microwave observations of the Earth's surface over such a length of time (380 days). I know of only one example which comes close, namely a 190-day comparison from REBEX-1 [26] for wintertime prairie. It is worth noting that there was no *a priori* expectation that the scatter plots would display "perfect" 1:1 relationships, or even linear relationships, for that matter. As explained in the discussion of the instrumentation-related aspects of this match in Chapter 2, TMRS2 cold calibration errors can account for the difference between the slope of the best-fit line and the 1:1 line.

The most important implication of the strong linear $T_{B,tmrs}$-$T_{B,eg}$ relationship is that passive microwave satellite observations may be effective for monitoring surface conditions in arctic tundra areas despite the relatively coarse spatial resolution.

Known causes of the differences between $T_{B,tmrs}$ and $T_{B,eg}$ include differences in the exact times of the respective observations, the effect of mountains within the REBEX-3 EASE-Grid footprint, errors in the cold calibration of the TMRS2 radiometers, and atmospheric effects. These mechanisms are addressed one by one in the following sections.

4.6 Time-of-Observation Differences

However good the linear correlation, it is not *perfect.* There is a "spread" about the best-fit line. If the atmosphere were removed, and if the region were horizontally uniform, we would expect $\Delta T_B = T_{B,eg}(t) - T_{B,tmrs}(t')$ assuming all instruments were accurately calibrated and $\Delta t = t - t'$ was small enough that the true target brightness had not changed. Since TMRS2 observations were made every 30 minutes, $\Delta t \leq 15$ minutes. Most observed values of $dT_{B,tmrs}(t')/dt'$ were $< \pm 4$ K/hr but some ranged up to ± 12 K/hr, so up to ± 4 K of any ΔT_B value could be a result of time offsets.

The SSM/I overflights occurred during REBEX-3 local morning and late afternoon times (see Fig. 4.11) when the ground brightnesses were often changing the fastest.

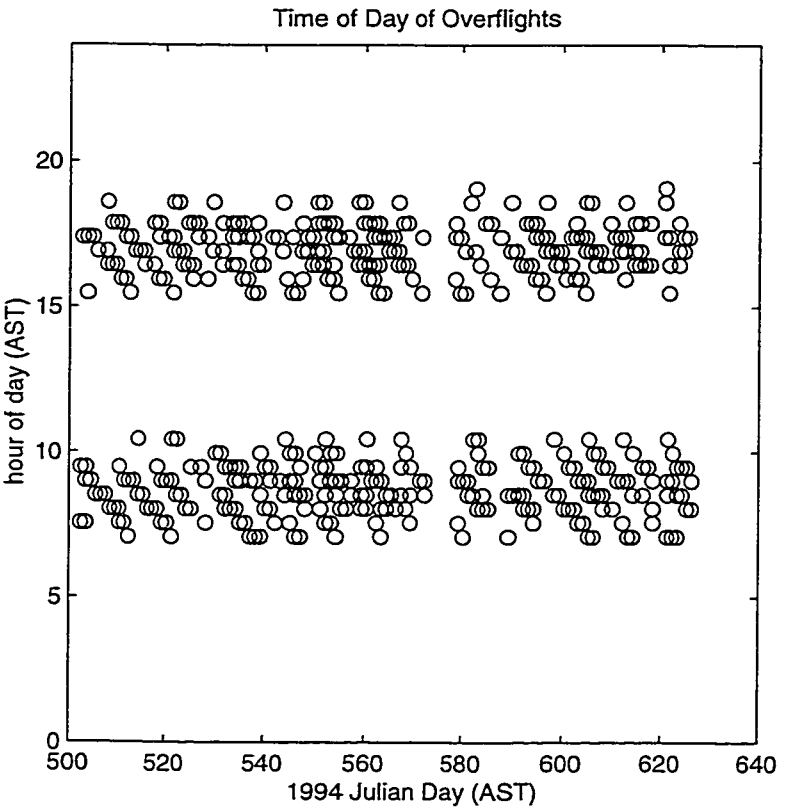

Figure 4.11: Typical SSM/I overflight times (F-11 and F-13). Abscissa spans the snow-free period.

4.7 Topographic effects

On the North Slope in the vicinity of the REBEX-3 site, the Brooks Range mountains and the tundra of the Slope itself lie on either side of a fairly well-delineated boundary which runs approximately northeast-southwest for a distance spanning many EASE-Grid cells (Figure 4.12).

Recall that the footprint size of an EASE-Grid pixel is the same as that of the 19V-channel footprint, 69 km × 43 km. The REBEX-3 site was within about 20 km of the northern edge of the Brooks Range mountains, so the footprint of the REBEX-3 EASE-Grid pixel included a portion of the mountains.

The effect of mountains being included within the footprint of the REBEX-3 EASE-Grid pixel can be quantified in the following manner. I compared the signature of the REBEX-3 pixel (280,312) to that from two nearby pixels: the nearest one whose footprint contained only mountains (279,310) and the nearest one whose footprint contained only tundra (280,313). I will refer to these as the "all-mountain" and "all-tundra" pixels, respectively. Note that the footprints of the all-tundra and REBEX-3 pixels have considerable overlap.

The annual signatures of the 19 and 37 GHz channels are similar for all three pixels. The primary difference is that the all-mountain brightnesses are warmer during the winter and colder during the summer than the REBEX-3 pixel. Conversely, the all-tundra brightnesses are colder during the winter and warmer during the summer compared to the REBEX-3 pixel. We would expect the all-tundra brightnesses to match the TMRS2 brightnesses more closely than the all-mountain brightnesses, and they do.

If scatter plots for the 19 and 37 GHz channels are constructed as depicted in Fig. 4.13, the R^2 values and the slopes and y-intercepts of the respective best-fit lines are as given in Table 4.6. The high R^2 values indicate strong linear relationships between corresponding brightnesses from the all-mountain and all-tundra footprints and the REBEX-3 footprint.

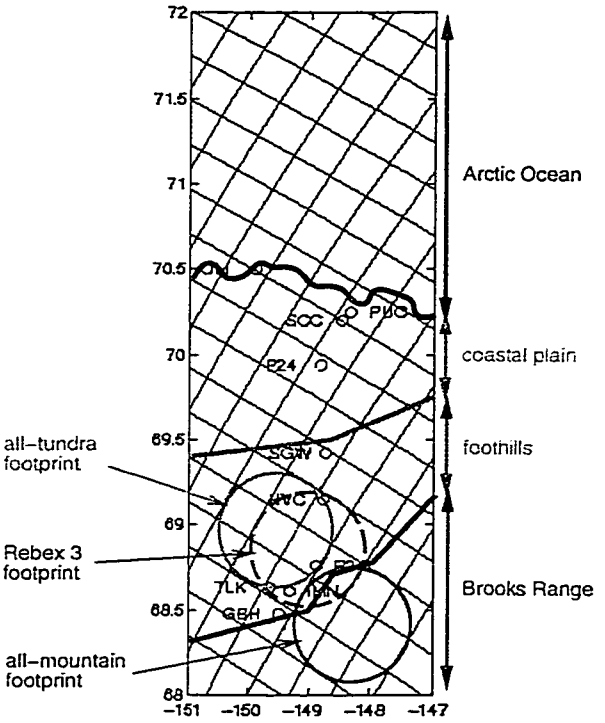

Figure 4.12: North Slope map with 25-km EASE-Grid overlay. Large circles represent EASE-Grid footprints. North is up. R3=REBEX-3 site; TLK=Toolik; IMN=Imnaviat; HVC=Happy Valley camp; GBH=Galbraith Lake; SGW=Sagwon Bluff; P24=Pipeline Mile 24; SCC=Deadhorse; PUO=Prudhoe Bay; OLI=Oliktok Point

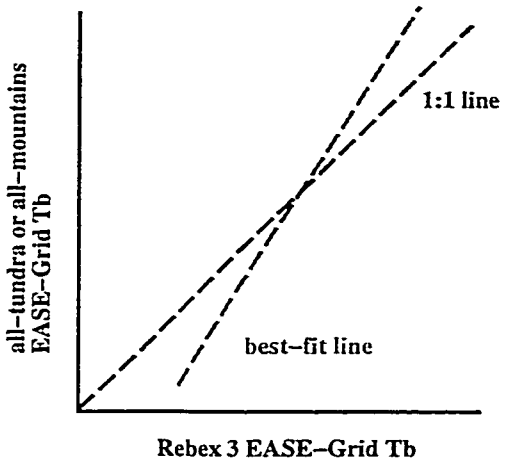

Figure 4.13: Scatter plot template for comparing all-tundra and all-mountain EASE-Grid pixels vs. REBEX-3 EASE-Grid pixel.

chan	R^2	slope	y-intcp (K)
all-tundra			
19V	0.9887	1.0140	-3.1
19H	0.9840	1.0507	-13.3
37V	0.9954	1.0183	-4.5
37H	0.9946	1.0305	-7.8
all-mountains			
19V	0.9504	0.9214	16.5
19H	0.9458	0.7438	64.2
37V	0.9802	0.7856	52.7
37H	0.9782	0.7517	61.7

Table 4.6: R^2 values and best-fit lines.

Furthermore, a very close absolute match with the all-tundra brightnesses is demonstrated, while significant differences are seen with respect to the all-mountain absolute brightnesses.

The effect of the mountains contaminating the REBEX-3 pixel was to introduce a warm bias into the cold EASE-Grid brightnesses and a cold bias into the hot EASE-Grid brightnesses. Thus in Fig. 4.10, points at cold EASE-Grid brightness values should be adjusted to the left (toward colder values) while points at hot EASE-Grid brightness values should be adjusted to the right (toward hotter values) to more accurately reflect the tundra conditions at the REBEX-3 site. Based on the information presented in Table 4.6, the adjustment can take the form of a linear adjustment for each channel. If the same adjustment were made

chan	77K	200K	300K
19V	-2.0	-0.3	1.1
19H	-9.4	-3.2	1.9
37V	-3.1	-0.8	1.0
37H	-5.5	-1.7	1.3

Table 4.7: Horizontal adjustments to Fig. 4.10 best-fit lines for contamination by mountains.

in a scatter plot of the all-tundra brightnesses vs. REBEX-3 EASE-Grid brightnesses (not the same as Fig. 4.10), the effect would be to make the best-fit lines match their respective 1:1 lines.

I emphasize that this is an adjustment of the REBEX-3 satellite data (EASE-Grid) values, not the TMRS2 ground data values. The net effect for each channel in Fig. 4.10 is a best-fit line which is closer to the 1:1 line. The adjustment amounts for REBEX-3 EASE-Grid brightnesses of 77, 200, and 300 K are listed in Table 4.7. These amounts are small over the respective ranges of observed T_B values. One reason is that the contamination occurred at the edge of the footprint, where the synthetic antenna pattern gain was low.

4.8 Atmospheric effects

The effect of the atmosphere must be considered when comparing ground-based and satellite brightness observations at the SSM/I frequencies. This would be the case even if SSM/I and TMRS2 observed the *exact* same footprint on the ground, so it is not a spatial scaling problem *per se*. The atmosphere is a non-negligible absorber and emitter of microwave radiation at 19 and 37 GHz.

In this section, I will calculate the amount of absorption and emission, and use the information to generate atmospherically-adjusted EASE-Grid brightnesses—i.e., what SSM/I would have measured if it had made its observation from the surface.

4.8.1 Radiative transfer

The total brightness seen by the SSM/I, $T_{SSMI}(f,p)$ at frequency f and polarization p, has three components:

$$T_{SSMI}(f,p) = \frac{T_{SURF}(\theta,f,p)}{L(\theta,f)} + T_{UP}(\theta,f) + \frac{T_{SKY}(\theta,f)}{L(\theta,f)} R_{SURF}(\theta,f,p), \qquad (4.9)$$

where T_{SSMI} can be either an EASE-Gridded or a pre-EASE-Grid (swath) brightness temperature. θ is the viewing angle relative to zenith at the spot where the instrument boresight vector intersects the earth's surface. Nominally, $\theta = 53.1°$ for SSM/I. I will refer to this as the "incidence angle" for convenience. $T_{SURF}(\theta,f,p)$ would be the actual brightness of the surface scene within the field of view of the instrument when viewed at the incidence angle if there were no atmosphere. $L(\theta,f)$ is the atmospheric loss factor. $1/L(\theta,f)$ is the atmospheric transmission. $T_{UP}(\theta,f)$ is the upwelling brightness of the atmosphere itself, and $T_{SKY}(\theta,f)$ is the downwelling brightness seen from the earth's surface looking up at the incidence angle. $R_{SURF}(\theta,f,p)$ is the surface reflectivity.

The first term in Equation 4.9 accounts for the actual brightness of the scene attenuated by atmospheric absorption. The second term accounts for the upwelling brightness of the atmosphere seen at the top of the atmosphere (TOA). And, the last term accounts for the downwelling atmospheric brightness (seen from the surface) reflected back up from the surface and attenuated by the time it reaches the TOA.

A TMRS2 brightness $T_{B,tmrs}$, comprises two parts: actual surface emission and reflected sky brightness. We do not need to consider any effects of the atmosphere on T_{SURF} since the observations were made from a height of 10 meters.

$$T_{B,tmrs}(f,p) = T_{SURF}(\theta,f,p) + T_{SKY}(\theta,f) R_{SURF}(\theta,f,p). \qquad (4.10)$$

R_{SURF} is the same as in Eq. 4.9. In general, $R_{SURF}(\theta,f,p)$ is a function of the bistatic scattering coefficient σ^o_{pq}. Modeling σ^o_{pq} for the tundra surface is beyond the scope of this work. But, by comparing REBEX-3 thermal infrared brightnesses and microwave

brightnesses, we know that the snow-free R_{SURF} is small and nearly unpolarized with a low value around 0.04. Furthermore, since $T_{SKY}(\theta, f)$ is small relative to $T_{SURF}(\theta, f, p)$, and since $L(\theta, f)$ is always greater than one, deviations from the true value of $R_{SURF}(\theta, f, p)$ would not significantly affect the accuracy of T_{SSMI} or $T_{B,tmrs}$ estimates.

I define the atmospherically-adjusted EASE-Grid brightness as

$$T^{*}_{B,eg}(f,p) = (T_{B,eg}(f,p) - T_{UP}(\theta,f))L(\theta,f), \tag{4.11}$$

where $T_{B,eg}$ are from Fig. 4.9(a). $T^{*}_{B,eg}$ comprises ground emission and reflected sky emission terms as in Eq. 4.10, facilitating comparison. Note that knowledge of R_{SURF} is not explicitly required.

The downwelling brightness seen from the earth's surface looking up at the incidence angle is given by Equation 5.51a in [92]:

$$T_{SKY}(\theta) = T_{DN}(\theta) + T_{COS}e^{-\tau_o \sec(\theta)} \tag{4.12}$$

where T_{COS} is the isotropic cosmic background brightness of 2.7 K, and (Equation 5.49 in [92])

$$T_{DN}(\theta) = \sec\theta \int_0^{\infty} \kappa_g(z')T(z')e^{-\tau(0,z')\sec\theta}dz' \tag{4.13}$$

is the downwelling brightness of the atmosphere itself seen from the surface. The upwelling brightness of the atmosphere seen from the TOA is similar:

$$T_{UP}(\theta) = \sec\theta \int_0^{\infty} \kappa_g(z')T(z')e^{-\tau(z',\infty)\sec\theta}dz'. \tag{4.14}$$

Ulaby [92] provides expressions for many of these quantities. The optical depth of the atmosphere between two heights $z1$ and $z2$ is

$$\tau(z1,z2) = \int_{z1}^{z2} \kappa_a(z)dz. \tag{4.15}$$

So, $\tau(z',\infty)$ is the optical depth from height z' to the TOA, and $\tau(0,z')$ is the optical depth from the surface to z'.

The total zenith optical depth is

$$\tau_o = \int_0^\infty \kappa_g(z) dz, \tag{4.16}$$

and the total optical depth along the observation path is

$$\tau_\theta = \tau_o \sec(\theta). \tag{4.17}$$

The atmospheric loss factor is

$$L(\theta) = e^{\tau_o \sec(\theta)}. \tag{4.18}$$

$\kappa_g(z)$ is the atmospheric absorption coefficient, here including absorption by water vapor $\kappa'_{H_2O}(z)$ and by molecular oxygen $\kappa_{O_2}(z)$.

$$\kappa_g(z) = \kappa'_{H_2O}(z) + \kappa_{O_2}(z). \tag{4.19}$$

$\kappa'_{H_2O}(z)$ is a function of microwave frequency and the vertical profiles of atmospheric temperature, pressure, and water vapor. $\kappa_{O_2}(z)$ is a function of microwave frequency and the vertical profiles of atmospheric temperature and pressure. Expressions for $\kappa'_{H_2O}(z)$ and $\kappa_{O_2}(z)$ are given by Equations 5.22 and 5.40 from [92], respectively.

For simplicity, I will consider only the clear-sky case, accounting for absorption and emission by oxygen and water vapor, so $\kappa_a(z) = \kappa_g(z)$. Clouds would be the other potentially significant source of absorption and emission in $\kappa_a(z)$. No direct observations of cloud cover were made as part of REBEX-3, but average cloud cover for the eastern half of the North Slope is 55% [95]. If warranted, a future study could estimate cloud conditions indirectly from other measurements.

All of the preceding discussion assumes a plane-parallel atmosphere, with a slant path at a 53° zenith angle. At the SSM/I frequencies, the bulk of the radiatively significant atmosphere (water vapor) is in the troposphere, where the decrease of the true slant path angle with increasing height due to the earth's curvature is negligible.

4.8.2 Profile quantities

The only remaining quantities to specify are the vertical profiles of temperature, pressure, and water vapor density needed to compute $\kappa'_{H_2O}(z)$ and $\kappa_{O_2}(z)$. The profiles given in [92] are based on the 1962 U.S. Standard Atmosphere, which is a mid-latitude (45° N) spring/fall mean atmosphere. The U.S. Standard Atmosphere Supplements, 1966 [1] defines 13 additional atmospheres at various latitudes and various seasons. Of relevance to REBEX-3 are the atmospheres for 60° N and 75° N, which bracket the REBEX-3 latitude. These are called "sub-arctic" and "arctic" in the Supplements. I will refer to both as simply "arctic". July, warm January, and cold January mean atmospheres are defined at these latitudes. Due to a lack of sounding data, the 75° N atmospheres are defined up to only 30 km. Since the bulk of the radiatively significant atmosphere at SSM/I frequencies lies below this height, this is not a serious restriction.

4.8.2.1 Temperature profile

The arctic temperature profile has generally lower tropospheric temperatures and a lower tropopause (8–10 km vs. 11 km, varying with season) than the Standard Atmosphere, and there is a distinct surface inversion during the winter. The thickness of the roughly isothermal portion of the stratosphere also increases with latitude. Taking averages of the 60° N and 75° N July profiles, I obtained the following approximate temperature profile for the "REBEX-3 standard atmosphere" for the summer season:

$$T(z) = T_o - 6.5\,z \text{ K}, \; 0 \leq z \leq 10 \text{ km}, \tag{4.20}$$

$$T(z) = T(10\text{km}) \text{ K}, \; 10 \leq z \leq 30 \text{ km} \tag{4.21}$$

where T_o is the temperature at sea level and z is height above sea level. The elevation of the REBEX-3 site was 0.5 km, so I can replace Eq. 4.21 with $T(z) = (T_{air}) - 6.5(z - 0.5)$ where T_{air} was the surface air temperature at the REBEX-3 site. The temperature profile enters directly into the expressions for T_{UP} and T_{DN}, and thus directly into the overall brightness

seen by the SSM/I.

4.8.2.2 Pressure profile

The pressure profile, on the other hand, exerts its influence indirectly via the absorption coefficient $\kappa_g(z)$. Both the 60° N and 75° N July pressure profiles deviate from the Standard Atmosphere pressure profile by less than one percent below 10 km altitude [1]. So I simply used the following approximation (accurate to 3% below 10 km) to the U.S. Standard Atmosphere profile of pressure below 30 km, taken from [92]:

$$P(z) = P_o e^{-z/H_3} \text{ mbar} \tag{4.22}$$

where the surface pressure is $P_o = 1013.25$ mbar and the pressure scale height is $H_3 = 7.7$ km.

4.8.2.3 Water vapor density profile

The water vapor density profile was approximated with the exponential expression

$$\rho(z) = \rho_o e^{-z/H_4} \text{ g/m}^3 \tag{4.23}$$

from [92], where the scale height H_4 was taken to be 2 km. The surface water vapor density, ρ_o was computed using values of surface air temperature and relative humidity from REBEX-3 field data.

4.8.3 Atmospherically-adjusted SSM/I observations

Figures 4.14, 4.15, and 4.16 show the computed T_{UP}, T_{SKY}, and L, respectively, during the snow-free period of interest from mid-May through mid-September, 1995.

While atmospheric absorption and emission are as large as 25 K, the amounts are nearly equal so that the net effect (difference) is near zero over the 200–300 K range of summertime brightnesses. The difference between the atmospherically-adjusted "surface" brightnesses, $T^*_{B,eg}$, and the original satellite values $T_{B,eg}$ are shown in Fig. 4.17. The plots show the

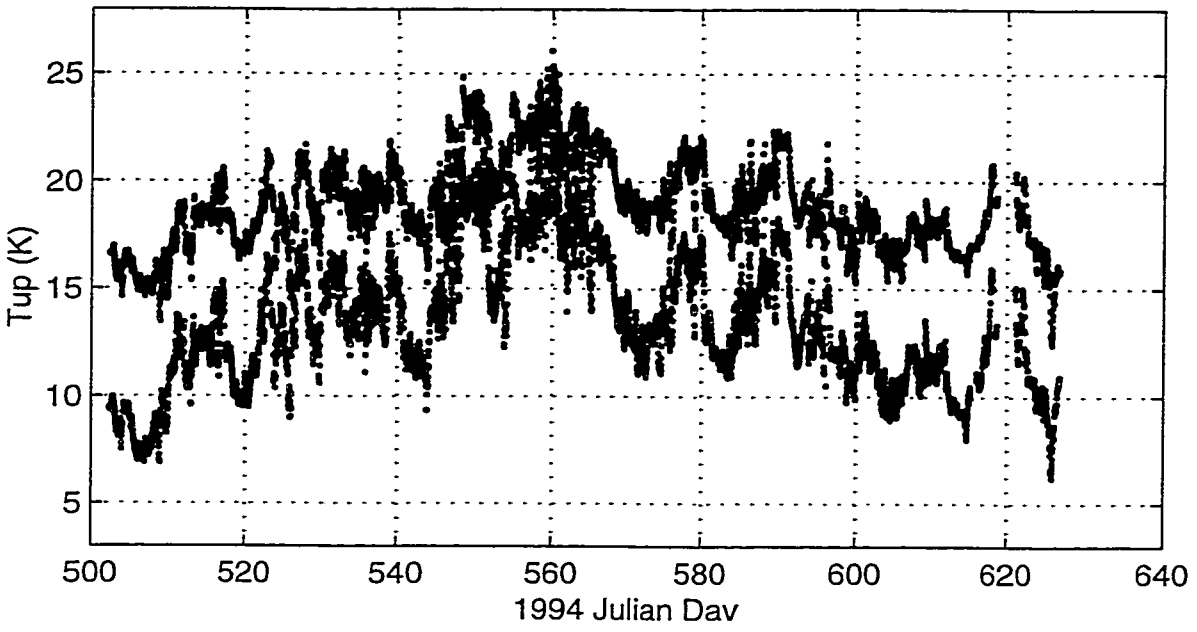

Figure 4.14: Estimated upwelling atmospheric brightness, T_{UP}, at 53° seen from the TOA. Lower curve: 19 GHz channels, upper curve: 37 GHz channels.

amount to subtract from $T_{B,eg}$ to arrive at an adjusted brightness. Figure 4.17 indicates satellite brightnesses slightly greater than adjusted "surface" brightnesses, with a maximum adjustment of about 3 K. If the surface had been warmer and the air temperatures cooler, the reverse result might have been obtained.

Atmospheric adjustment amounts for REBEX-3 EASE-Grid brightnesses of 77, 200, and 300 K are listed in Table 4.8.

So, the effects of a clear atmosphere are small under the combination of surface bright-

chan	77K	200K	300K
19V	6.8	1.6	-2.6
19H	5.5	0.9	-2.8
37V	1.1	-0.4	-1.7
37H	-0.2	-1.1	-1.8

Table 4.8: Horizontal adjustments to Fig. 4.10 best-fit lines for atmospheric effects.

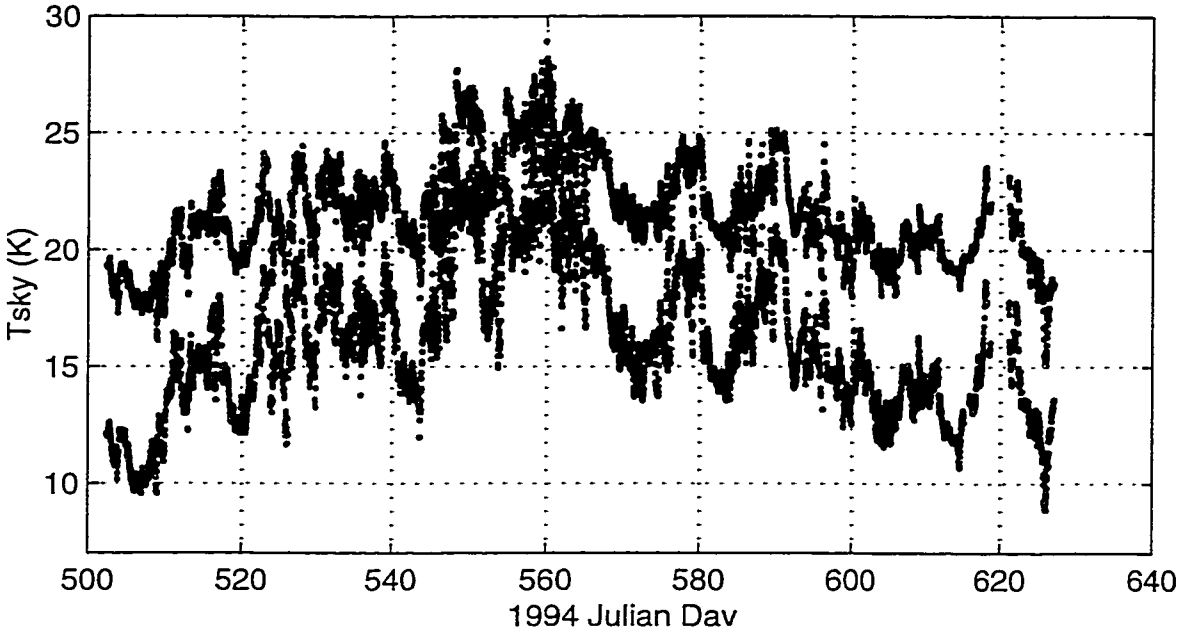

Figure 4.15: Estimated downwelling brightness, T_{SKY}, at 53° seen from the surface. Lower curve: 19 GHz channels, upper curve: 37 GHz channels.

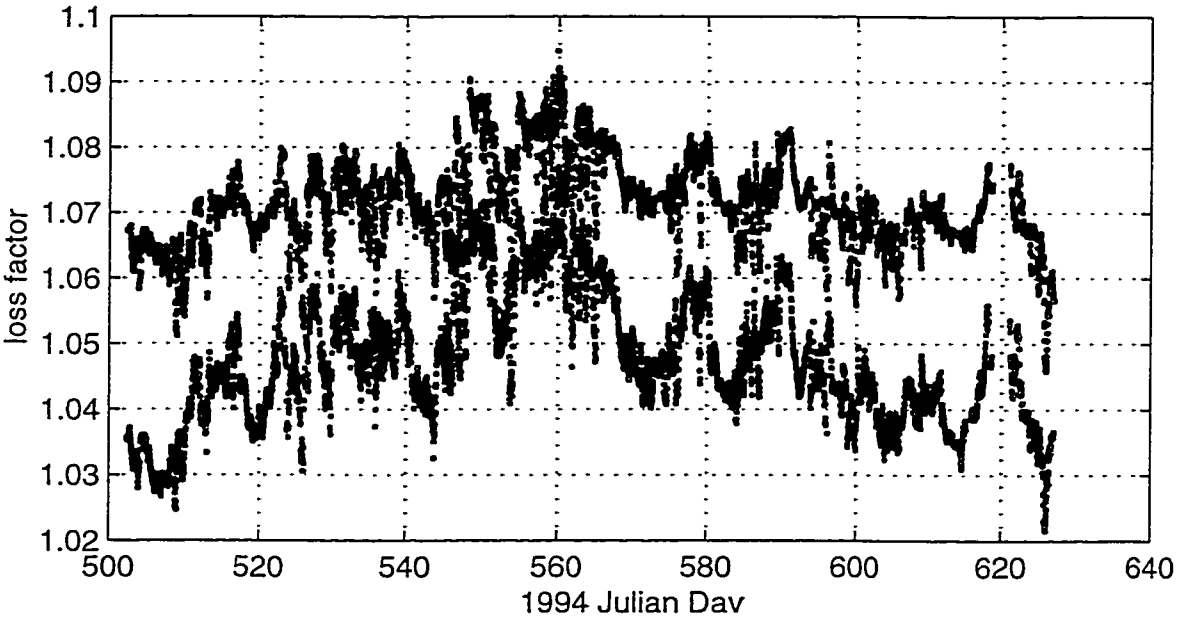

Figure 4.16: Estimated atmospheric loss factor, $L(\theta, f)$, at 53°. Lower curve: 19 GHz channels, upper curve: 37 GHz channels.

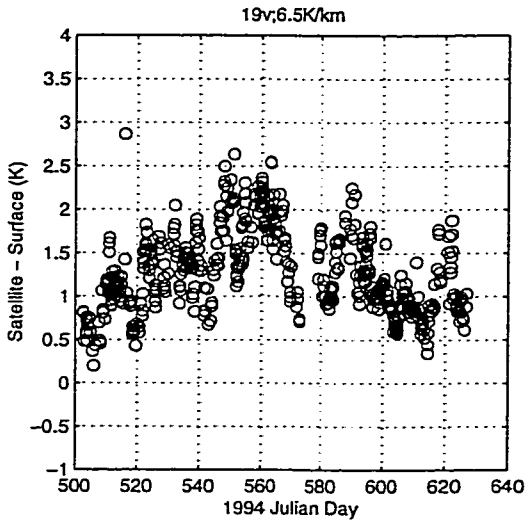

(a) 19V

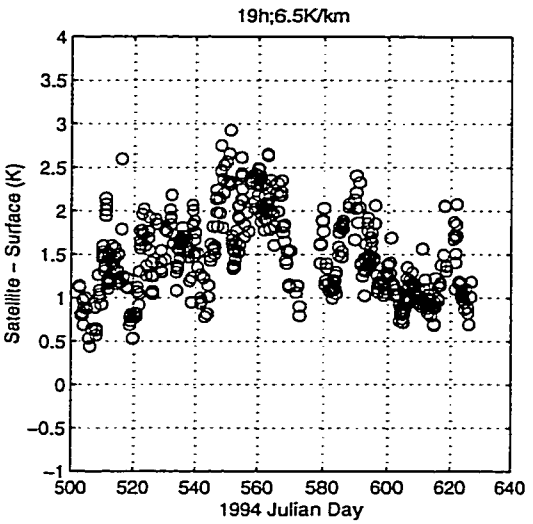

(b) 19H

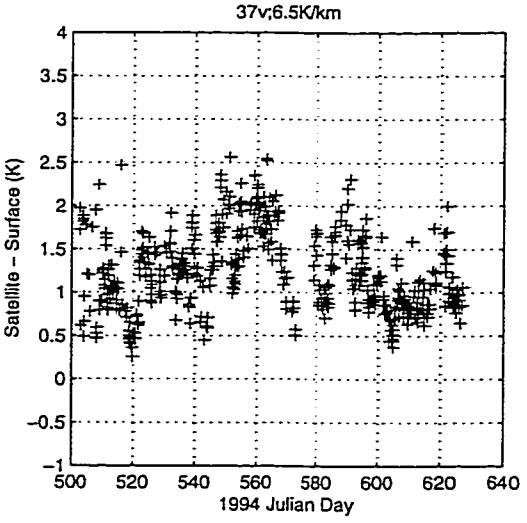

(c) 37V

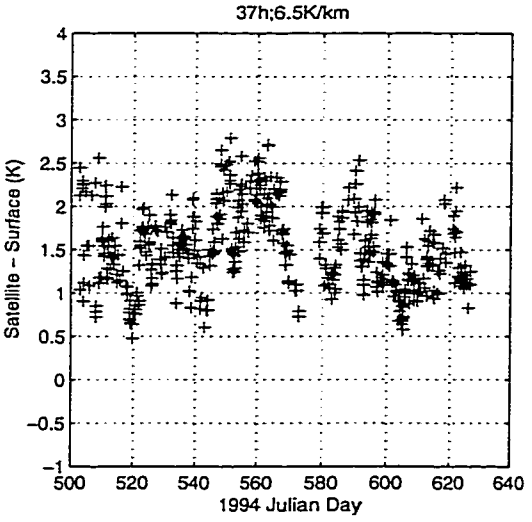

(d) 37H

Figure 4.17: Atmospheric adjustments to EASE-Grid observations.

nesses and atmospheric conditions considered. Thus, SSM/I can be an excellent observational tool under such conditions without requiring complex atmospheric corrections at 19 and 37 GHz. This is fortuitous for a region where meteorological observations are very sparse.

4.9 Cold Calibration Errors

As described in Chapter 2, the TMRS2 radiometer cold calibrations contained a warm bias due to physical warming of the cold target, and the target not completely filling the field-of-view of the radiometers. The hot calibrations did not suffer from a corresponding bias. Thus, the effect was to rotate the best-fit line counter-clockwise about the point on the line equal to the hot calibration point (typical value: 270 K). The exact amount of rotation is not known. However, based on laboratory tests, the error in the TMRS2 brightness at an EASE-Grid brightness of 77 K could be as much as 35–40 K. In other words, up to 35–40 K of the difference between the 1:1 line and the best-fit line at an abscissa value (EASE-Grid brightness) of 77 K could be due to cold calibration errors. The high R^2 values found in the comparisons and the encouraging implications are based on relative relationships, so they are unaffected by these calibration problems.

4.10 Implications for lower-frequency observations

The comparisons presented in this chapter were conducted at the 19 and 37 GHz SSM/I frequencies and polarizations because those were the only passive microwave satellite observations available for REBEX-3. Lower-frequency observations with their greater ability to sense through snow and vegetation and into the soil are likely to be more useful, once such satellite observations become available. However, the results of the REBEX-3 comparison can still be of use.

Lower-frequency satellite sensors are likely to have a spatial resolution no better than SSM/I. The gridded REBEX-3 SSM/I dataset can give an indication of horizontal homo-

geneity at the SSM/I sensing depths under various conditions. And, this could help in assessing the effects of sub-pixel variability at the typically deeper sensing depths of the lower frequencies.

Atmospheric absorption and self-emission are less significant at lower microwave frequencies than at the SSM/I frequencies. Scattering by cloud liquid water droplets and ice crystals would also be less significant. So, to the extent that atmospheric effects were a small problem at the frequencies considered in this chapter, they would be even less of a factor at lower frequencies.

Attenuation and scattering by vegetation would also be less significant at lower microwave frequencies, while at the same time, effective emission depths would be greater. So, there would be greater sensitivity to soil conditions (and at deeper depths) at lower frequencies. Atmospheric considerations aside, observations at lower and higher microwave frequencies would provide complementary information about conditions within a soil-vegetation column, simply based on the different effective emission depths and different sensitivities to vegetation.

Lower and higher microwave frequencies would also be complementary with respect to sensing conditions within (dry) snowpacks and soil-snowpack columns—a significant consideration for areas covered with snow 8–9 months of every year.

4.11 Summary

In this chapter, I compared TMRS2 ground-based brightness observations with co-located, contemporaneous SSM/I observations at 19 and 37 GHz. EASE-Grid spatially interpolated brightnesses were generated from a EASE-Grid software processor, custom-designed for this dissertation. The processor uses the exact same Backus-Gilbert interpolation routines as the NSIDC standard processor. This processor also extracted pixels from all overflights of the REBEX-3 site, including pixels which would have been discarded by the standard processor due to swath overlap. The accuracy of the EASE-Gridded data was

verified against the original swath data for both the F-11 and F-13 SSM/I sensors.

Very strong linear correlations ($R^2 > 0.92$) between SSM/I EASE-Grid and ground-based brightness observations were found for the 19 and 37 GHz SSM/I channels over the 380-day REBEX-3 period, before adjusting for any atmospheric, topographic, or calibration-related effects. With respect to the scatter plots of Fig. 4.10, the spread of the points about the best-fit line is consistent with differences in the exact satellite and ground-based observation times. The best-fit lines differ from the 1:1 lines by -22 to -40 K at $T_{B,eg} = 77$ K and by 6.8–17.9 K at $T_{B,eg} = 300$ K. Topographic effects were shown to shift $T_{B,eg}$ by up to -9.4 K at 77 K and up to 1.9 K at 300 K. Atmospheric effects were shown to shift $T_{B,eg}$ by 6.8 K at 77 K and by up to -2.8 K at 300 K. Cold calibration errors can account for up to 40 K of the remaining differences at 77 K.

Without information on cloud parameters during REBEX-3, the actual effect of cloudy conditions could not be addressed.

CHAPTER 5

Conclusions and Contributions

5.1 Conclusions

The applicability of LSP/R modeling was examined for the tundra case. In general, predicted soil and vegetation temperatures and moistures appear reasonable. The canopy temperatures compare favorably with REBEX-3 measurements, although subsurface temperatures were overpredicted in the thawed portion of the active layer. This was most likely due to incorrect thermal conductivities and/or the underestimation of heat loss by air convection and heat radiation from subsurface layers to the atmosphere.

The response to precipitation—namely, evaporation from the canopy, wetting and drying of the surface soil layer, and infiltration into deeper soil layers—all appear realistic. Modeled infiltration into the highly porous peat layers is extremely rapid, as in real peat.

Ice formation and thawing at the surface and at the freezing front appear realistic, with moisture being drawn to the front from above and below as long as the ice does not persist long enough for over-concentration to occur. Over-concentration only occurs when a freezing front persists. Surface ice formation is consistent with observed weather conditions at the site.

Model 19 and 37 GHz brightnesses clearly have the right basic shape and signature compared to REBEX-3 observations. But the model overpredicts both the mean level and the amplitude of the diurnal variations. The majority of the predicted total brightness is the upwelling canopy brightness contribution. The model overpredictions of soil and canopy

temperatures account for some of the differences, but the bulk of the difference must be due to unconsidered factors such cooler inter-tussock valleys and tussock faces within the field-of-view of the radiometers or scatter darkening.

Very strong linear correlations ($R^2 > 0.92$) between SSM/I EASE-Grid and ground-based brightness observations were found for the 19 and 37 GHz V- and H-polarized channels over the 380-day REBEX-3 period, before adjusting for any atmospheric, topographic, or calibration-related effects. The spread of the points about the best-fit line in scatter plots (Fig. 4.10) is consistent with differences in the exact satellite and ground-based observation times during times of day when the microwave brightness changes rapidly. The main source of the differences was attributable to problems with the cold calibration technique used with the TMRS2 radiometers. Topographic and atmospheric effects were shown to be small in comparison.

These strong correlations indicate that the nature of the tundra and the conditions at the REBEX-3 site were very representative of the tundra and conditions within the EASE-Grid footprint containing the site, despite the four-order-of-magnitude difference in footprint diameters. The high degree of matching provides great encouragement that this might be the case in general across large portions of the North Slope. Should this prove to be the case for the North Slope, or for other tundra regions, then passive microwave satellite observations (at least at 19 and 37 GHz) would have great utility as a monitoring tool for or in retrievals of land surface conditions in these areas.

5.2 Contributions

The REBEX-3 dataset of long-term ground-based microwave brightness observations from the North Slope of Alaska is the only such dataset for tundra. It is also the only such dataset for tundra with coincident micro-meteorological observations. The 381 days of brightness observations and 371 days of micro-meteorological observations represent the longest such collocated dataset that I am aware of even for non-tundra areas. The micro-

meteorological data are publicly available and are being used by other arctic researchers.

The TMRS2 instrument system, originally developed for the research described in this dissertation, is one of only two such instrument systems for collecting collocated microwave, IR, and micro-meteorological observations. The radiometers are one of only 3 or 4 such SSM/I simulators hardened for extended ground-based deployment, and one of only two capable of long-duration remote operation without frequent absolute calibration. The system robustness has been demonstrated during REBEXs 3, 4, and 5, a total of over 500 deployed days.

The experience gained with respect to operating ground-based microwave radiometers under arctic conditions is already being put to use in planning ground-based observations at the ARM North Slope site in Barrow, Alaska. Experience with respect to the calibration pitfalls and design of TMRS2 are being used to improve the design of two next-generation systems.

The tundra version of the LSP/R model is a biophysically-based column model of heat and moisture fluxes within tundra vegetation and soil and between the tundra and the atmosphere coupled to a microwave emission model. It is an upgraded version of the original prairie LSP/R model, featuring true multi-layer soil capability, an adaptive time step with memory, corrected precipitation handling, and corrected handling of vegetation moisture in the microwave emission module.

This represents the first use of the LSP/R model to model tundra, the first testing of the freezing and thawing portion of the model with observed forcings and vs. field observations. It was also the first test with highly organic (peat) soils.

A dataset containing gridded SSM/I satellite brightness observations covering the state of Alaska for the REBEX-3 period has been generated for comparison against REBEX-3 ground-based observations and for evaluation of the utility of such satellite observations in land surface applications. The 380-day comparison of the ground-based and satellite brightness signatures is the longest such continuous comparison for a fixed site that I am

aware of.

A custom EASE-Grid software processor, now publicly available, was assembled to perform the gridding. The processor uses the exact same Backus-Gilbert interpolation routines as the NSIDC standard processor. This processor also extracted pixels from all overflights of the REBEX-3 site, including pixels which would have been discarded by the standard processor due to swath overlap. The accuracy of the EASE-Gridded data was verified against the original swath data for both the F-11 and F-13 SSM/I sensors.

5.3 Future Work

The tundra LSP/R modeling presented in Chapter 3 identified areas in which a number of model improvements can be made. These include solving the problem of moisture over-concentration at a freezing front, and including additional heat and moisture transfer processes to handle high-porosity cases. Incorporating details more specific to peat or organic soils, such as measured water retention characteristics, would also be worth investigating.

A 3-dimensional model or an aggregate of one-dimensional models might be necessary to account for the various micro-environments (inter-tussock valleys, non-sunlit faces of tussocks) within the field-of-view of the radiometers.

The radiobrightness model requires significant modifications for the tundra case, including replacing the smooth mineral soil boundary with a more realistic one, and a closer examination of canopy moisture content. Volume scattering within the vegetation layers is also worth examining for both tundra and prairie cases.

As is usually the case after a modeling exercise, additional field data are desirable.

After improvements, the tundra LSP/R model could be driven with forcing data from other North Slope sites, and the radiobrightness predictions compared vs. SSM/I observations. Is the match as good for other sites? How uniform is North Slope, radiometrically?

Microwave brightness appears to be an excellent indicator of tundra surface tempera-

ture. Can satellite observations be used to provide surface temperature data to operational climate models over tundra regions where other data sources (e.g., ground stations) are sparse or non-existent? Are other inversions or retrievals practical using existing SSM/I observations?

APPENDICES

APPENDIX A

REBEX-3 Calendar and Data Plots

A.1 Calendar

First official day of experiment = 253.

Last official day of experiment = 624.

Periods when experiment personnel were on-site:

trip	calendar dates	1994 Julian days
Deployment:	15 Aug 94–19 Sep 94	227–262
1st site visit:	19 Oct 94–20 Oct 94	292–293
2nd site visit:	17 Jan 95–18 Jan 95	382–383
3rd site visit:	27 Apr 95–20 May 95	482–505
Retrieval:	7 Sep 95–20 Sep 95	615–628

Table A.1: Site visit dates.

day of mo	Aug-94	Sep-94	Oct-94	Nov-94	Dec-94	Jan-95	Feb-95	Mar-95	Apr-95	May-95	Jun-95	Jul-95	Aug-95	Sep-95
1	213	244	274	305	335	366	397	425	456	486	517	547	578	609
2	214	245	275	306	336	367	398	426	457	487	518	548	579	610
3	215	246	276	307	337	368	399	427	458	488	519	549	580	611
4	216	247	277	308	338	369	400	428	459	489	520	550	581	612
5	217	248	278	309	339	370	401	429	460	490	521	551	582	613
6	218	249	279	310	340	371	402	430	461	491	522	552	583	614
7	219	250	280	311	341	372	403	431	462	492	523	553	584	615
8	220	251	281	312	342	373	404	432	463	493	524	554	585	616
9	221	252	282	313	343	374	405	433	464	494	525	555	586	617
10	222	253	283	314	344	375	406	434	465	495	526	556	587	618
11	223	254	284	315	345	376	407	435	466	496	527	557	588	619
12	224	255	285	316	346	377	408	436	467	497	528	558	589	620
13	225	256	286	317	347	378	409	437	468	498	529	559	590	621
14	226	257	287	318	348	379	410	438	469	499	530	560	591	622
15	227	258	288	319	349	380	411	439	470	500	531	561	592	623
16	228	259	289	320	350	381	412	440	471	501	532	562	593	624
17	229	260	290	321	351	382	413	441	472	502	533	563	594	625
18	230	261	291	322	352	383	414	442	473	503	534	564	595	626
19	231	262	292	323	353	384	415	443	474	504	535	565	596	627
20	232	263	293	324	354	385	416	444	475	505	536	566	597	628
21	233	264	294	325	355	386	417	445	476	506	537	567	598	629
22	234	265	295	326	356	387	418	446	477	507	538	568	599	630
23	235	266	296	327	357	388	419	447	478	508	539	569	600	631
24	236	267	297	328	358	389	420	448	479	509	540	570	601	632
25	237	268	298	329	359	390	421	449	480	510	541	571	602	633
26	238	269	299	330	360	391	422	450	481	511	542	572	603	634
27	239	270	300	331	361	392	423	451	482	512	543	573	604	635
28	240	271	301	332	362	393	424	452	483	513	544	574	605	636
29	241	272	302	333	363	394		453	484	514	545	575	606	637
30	242	273	303	334	364	395		454	485	515	546	576	607	638
31	243		304		365	396		455		516		577	608	

Table A.2: REBEX-3 Julian day to calendar date conversion chart.

A.2 Summary Annual Data Graphs

Summary graphs of the patched and interpolated field data are presented in this section. Additional monthly graphs can be found in the REBEX-3 field data report [48].

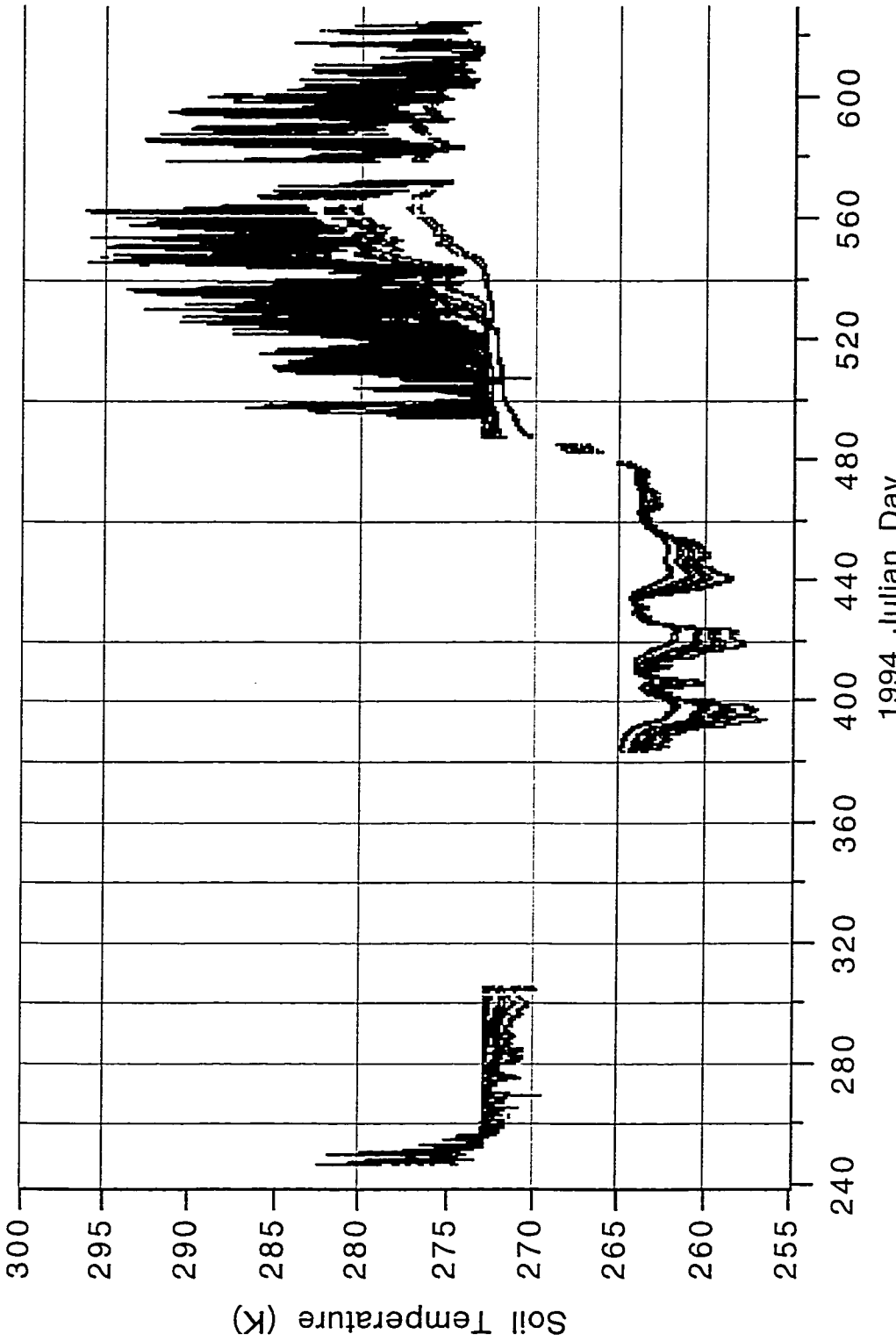

Figure A.1: Soil temperatures.

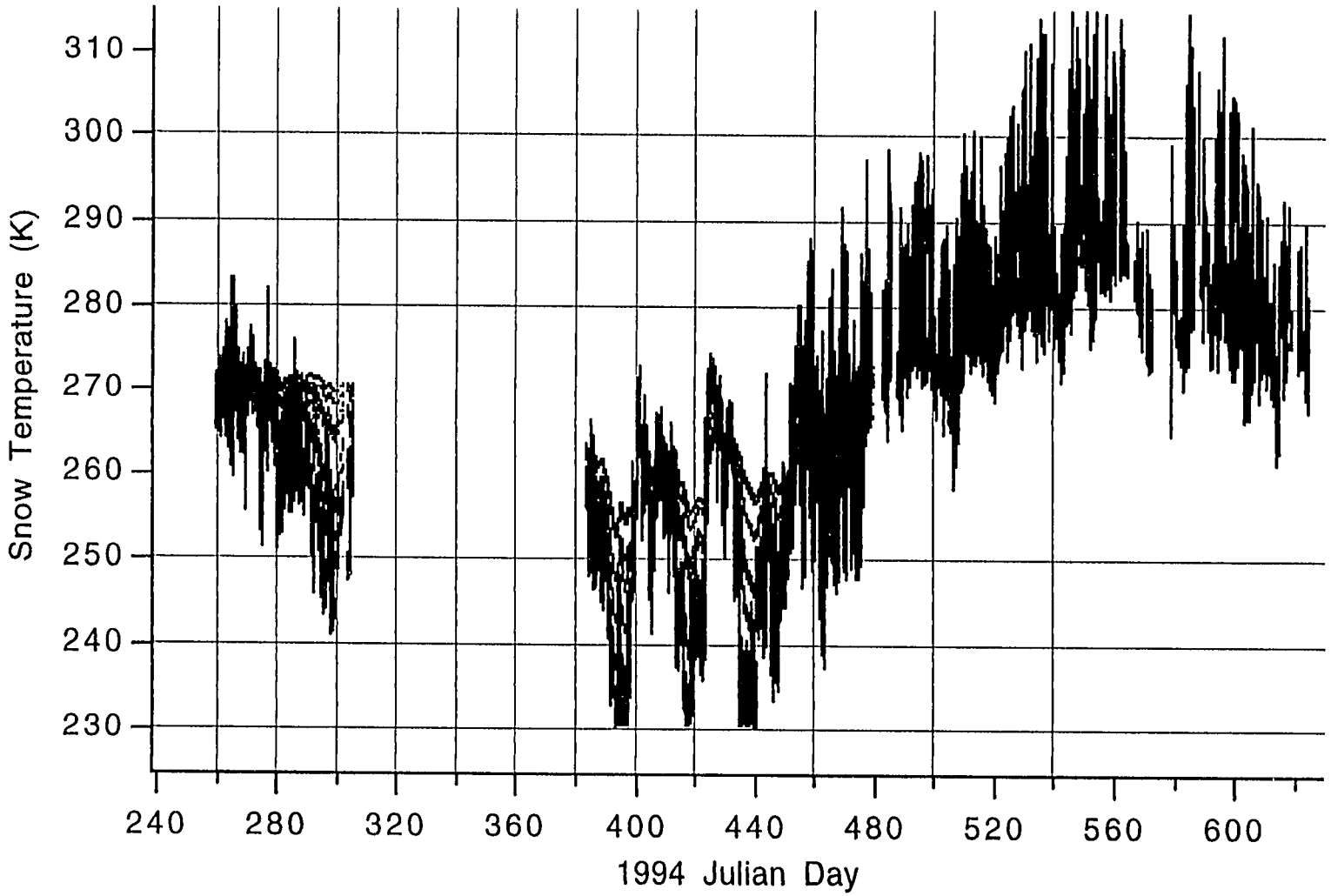

Figure A.2: Snow temperatures. Data after approximately day 500 are not valid since snow was not present.

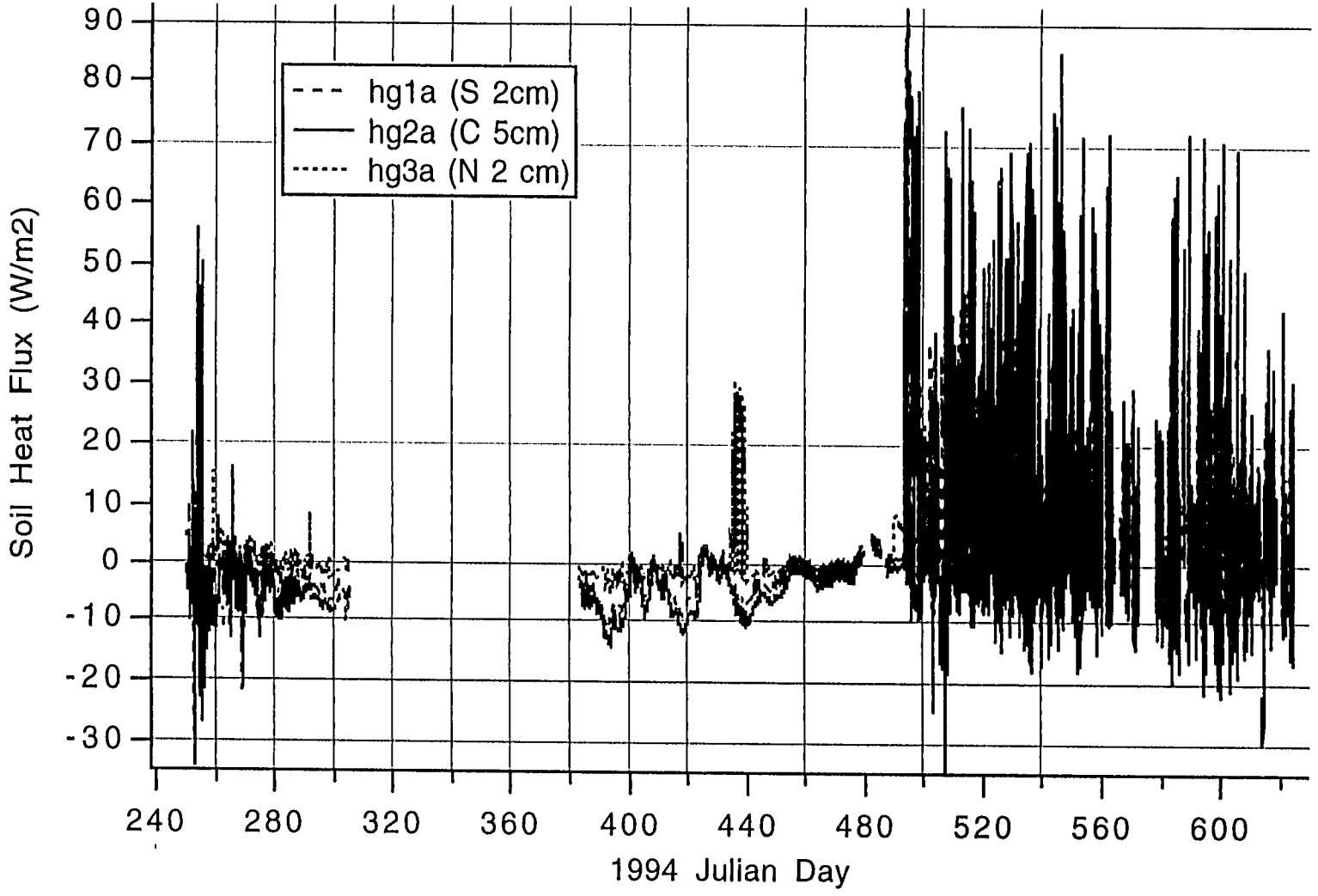

Figure A.3: Soil heat fluxes. 'C'= center third of tussock; 'S' = south third of tussock; 'N' = north third of tussock.

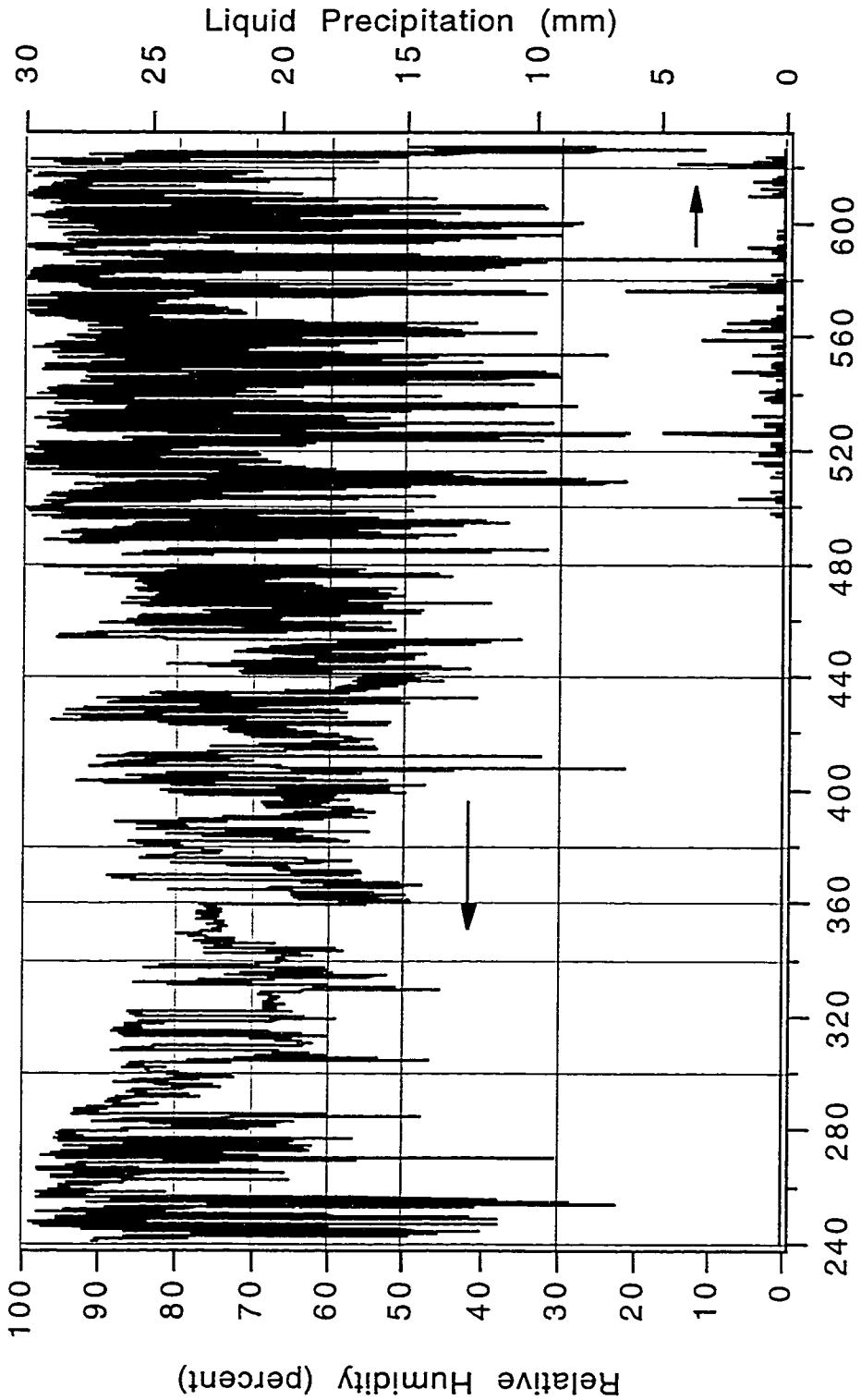

Figure A.4: Relative humidity (top trace) and precipitation (bottom trace).

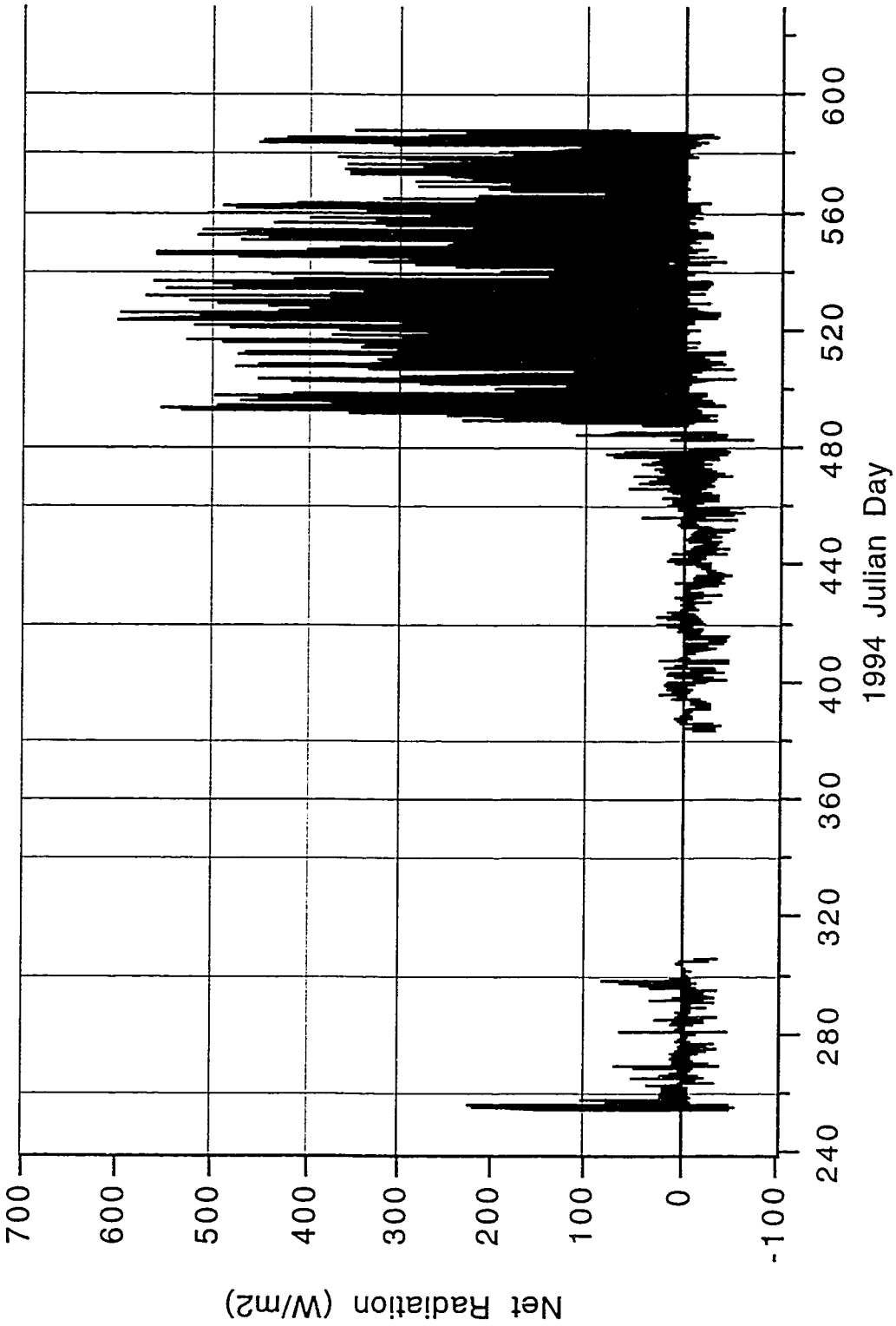

Figure A.5: Net radiation.

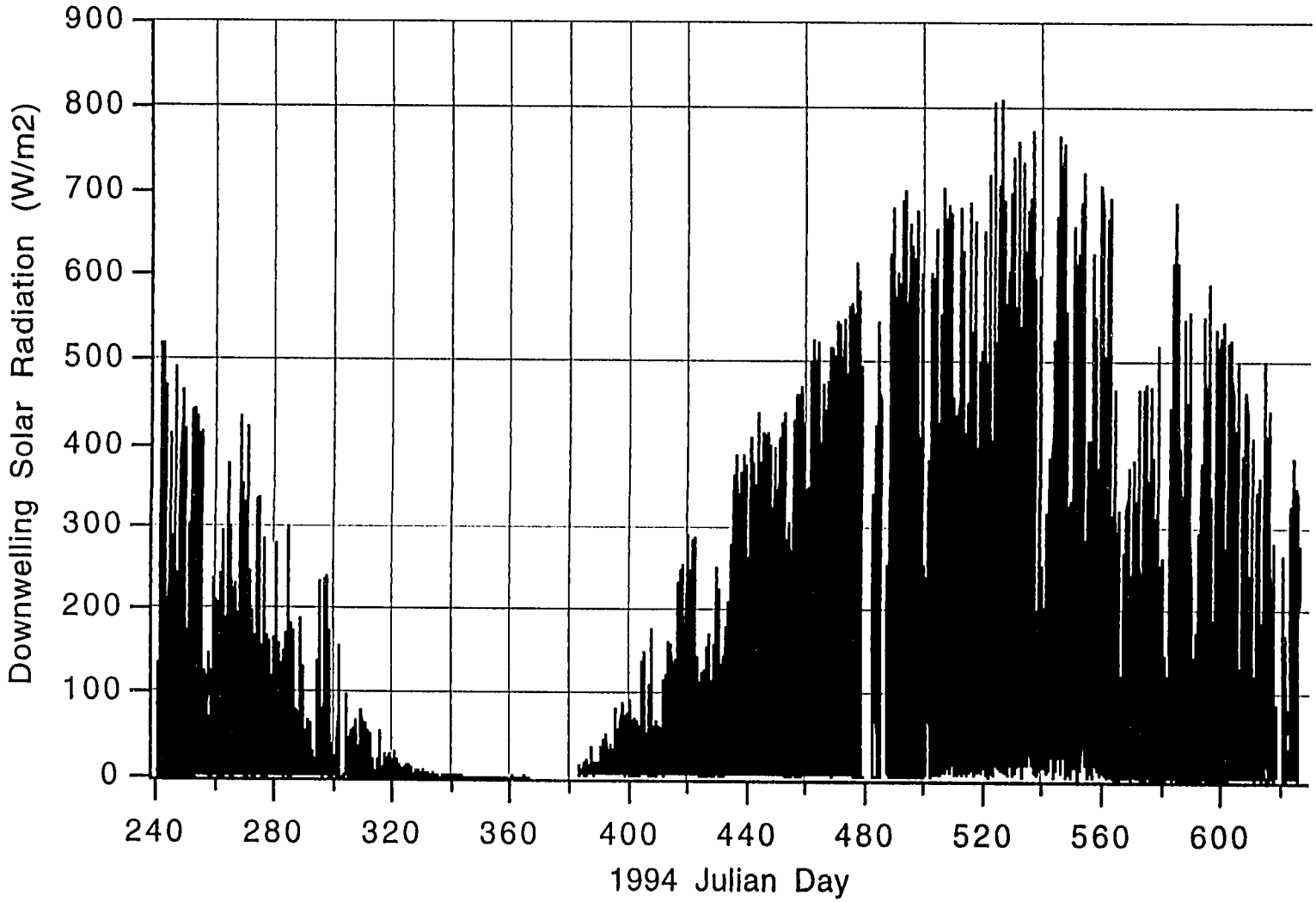

Figure A.6: Downwelling shortwave radiation.

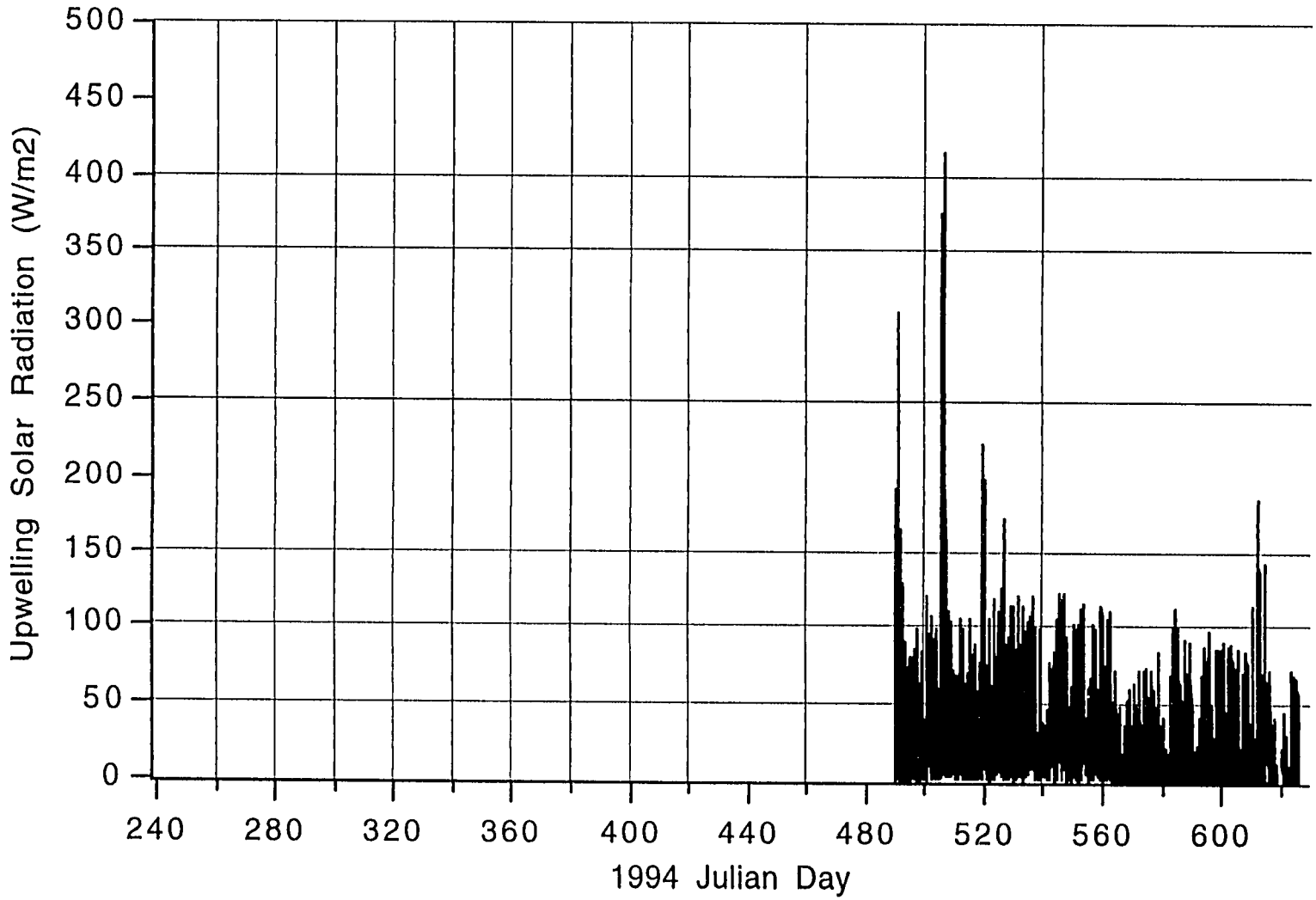

Figure A.7: Upwelling shortwave radiation. This instrument was added at the beginning of the snow-free season.

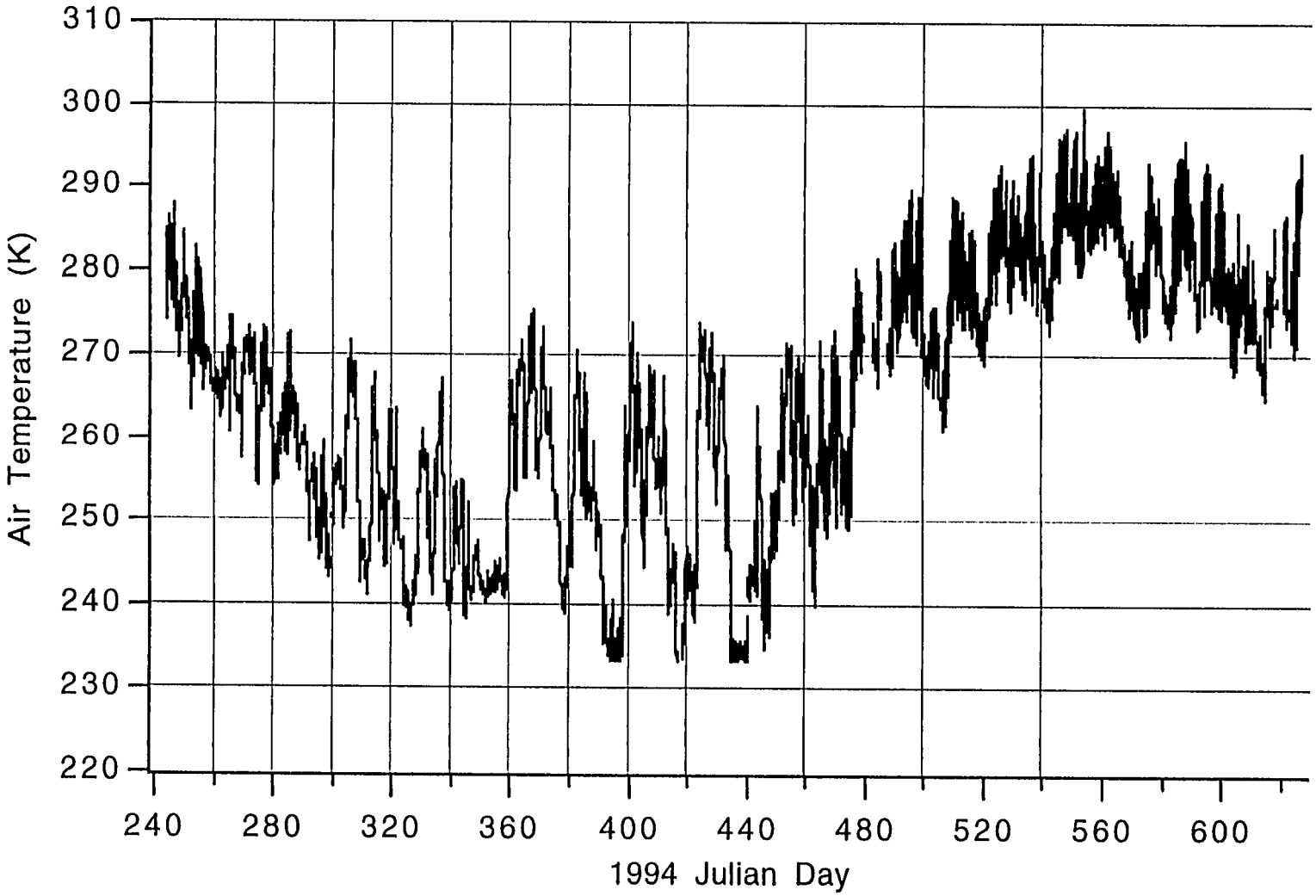

Figure A.8: Air temperature.

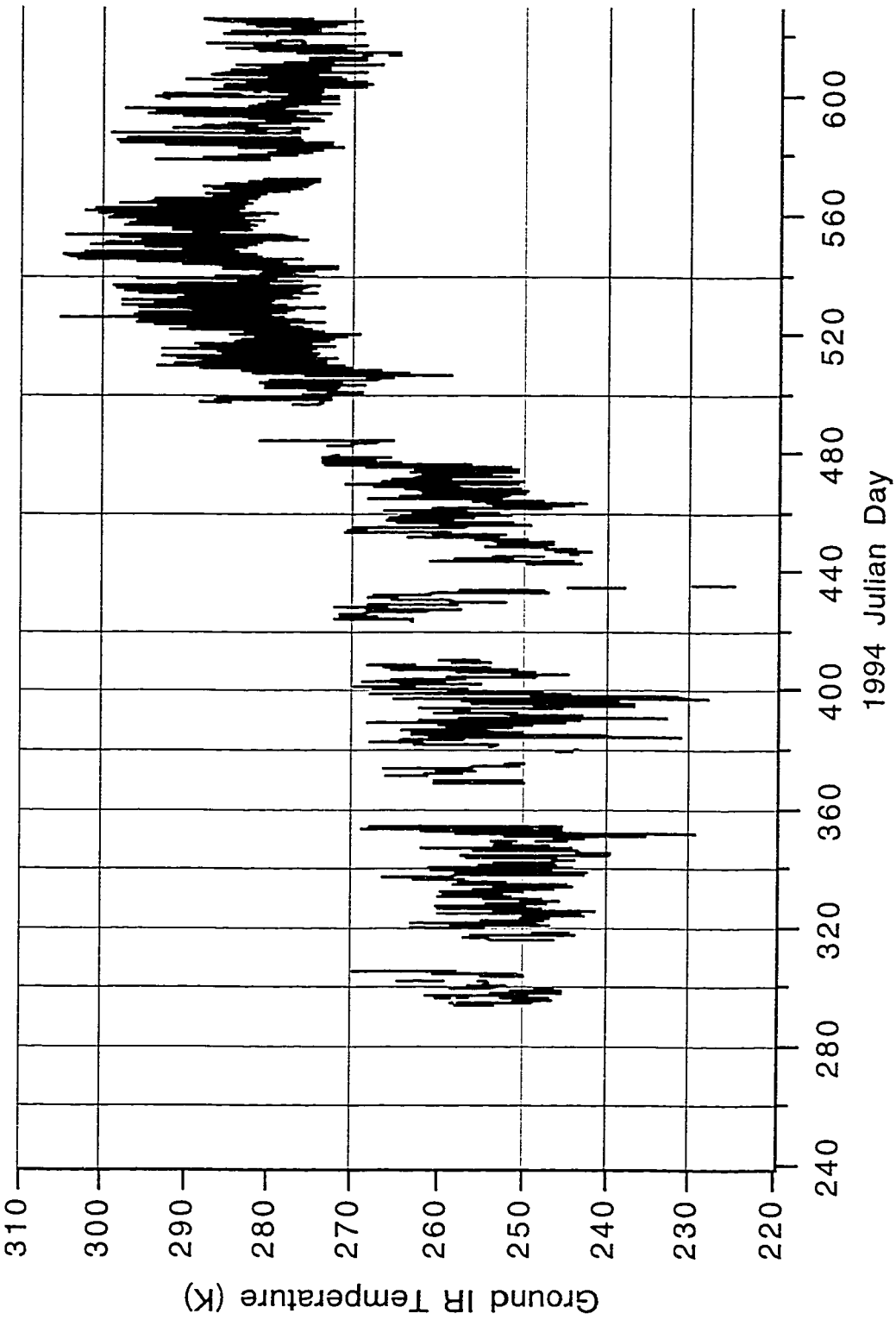

Figure A.9: Thermal IR skin temperature.

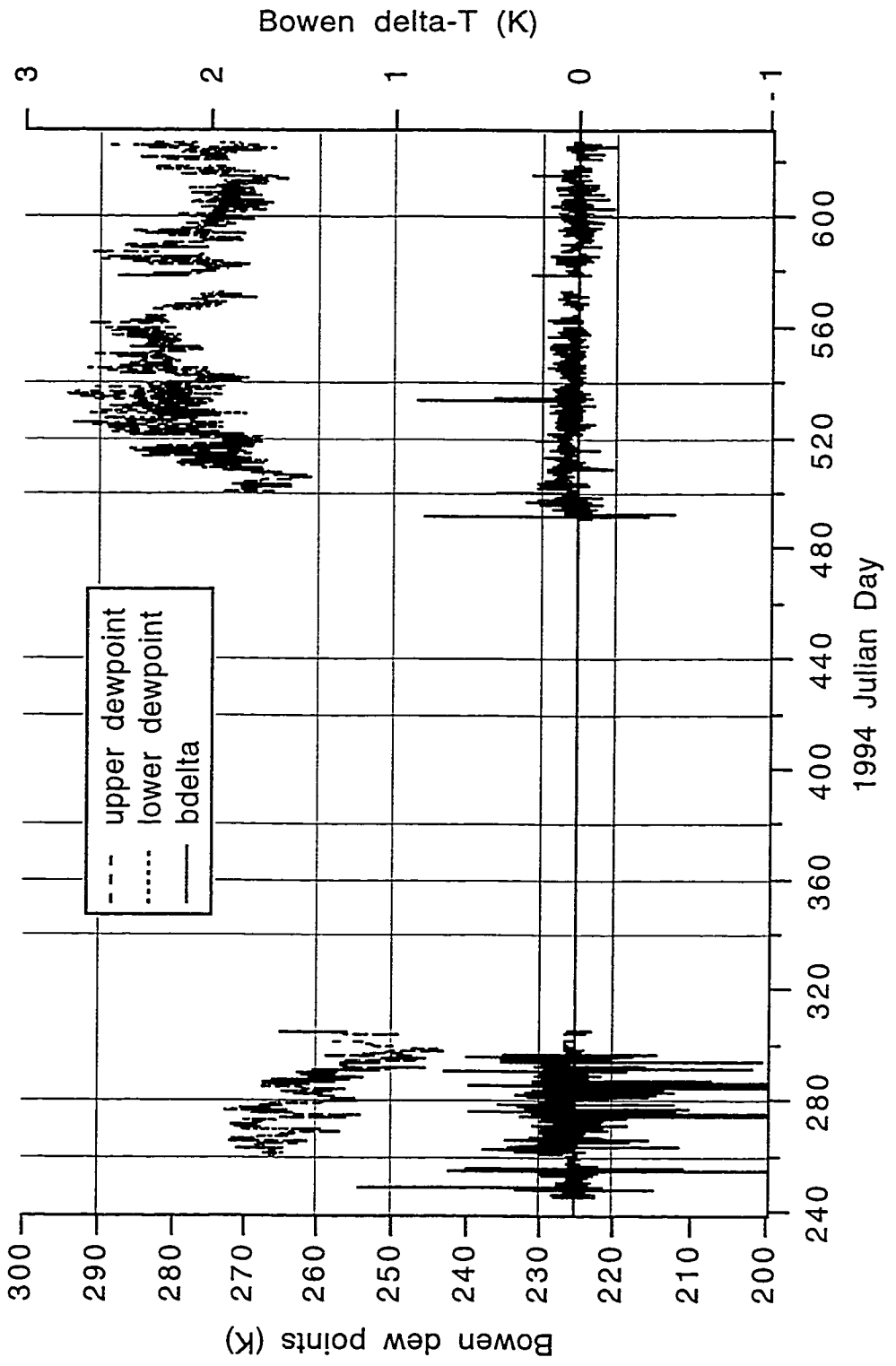

Figure A.10: Bowen dewpoints (upper traces) and temperature difference (lower traces). The Bowen instrument was turned off during the winter, and suffered a leak early in the summer. The data are suspect.

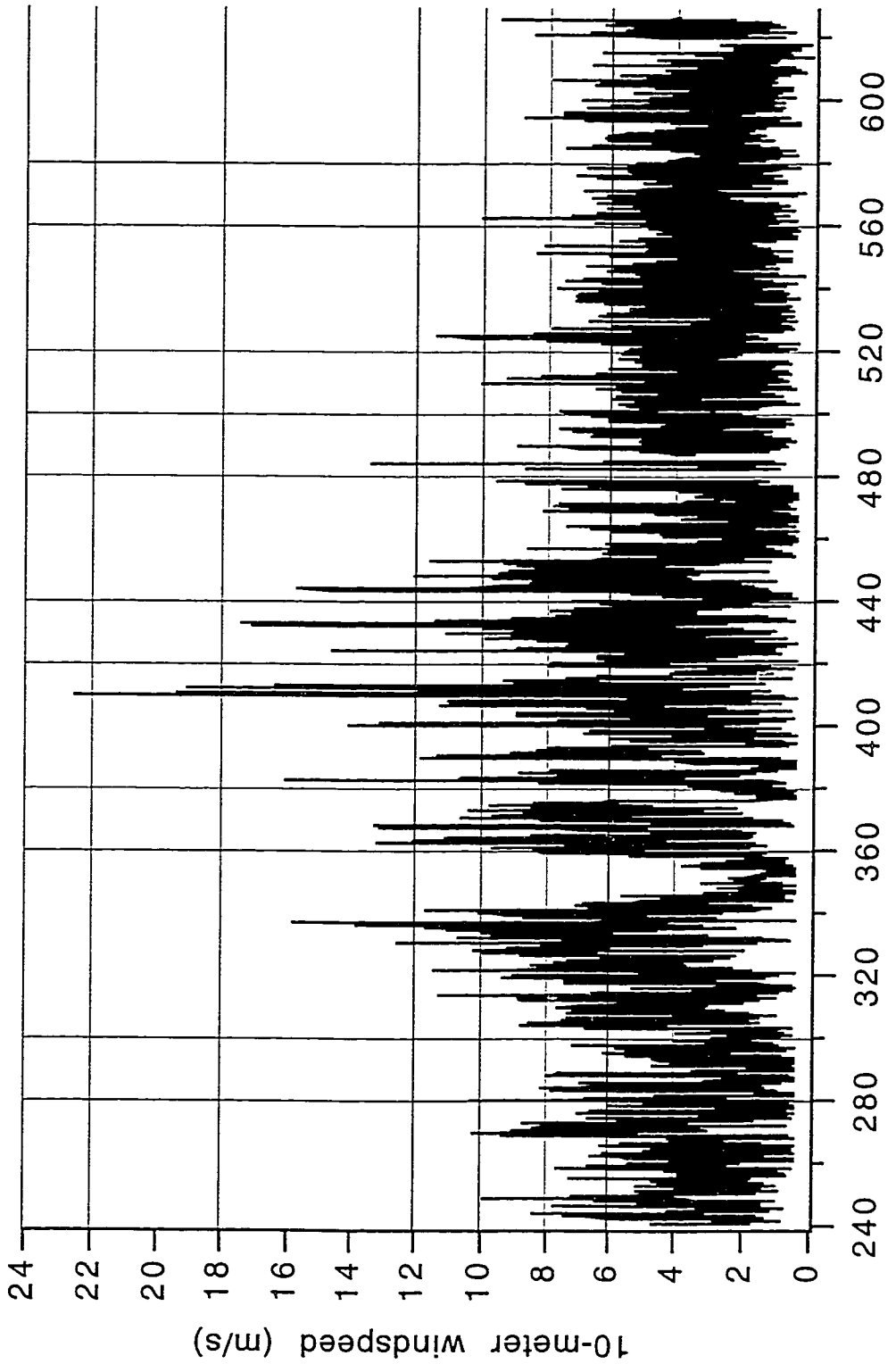

Figure A.11: 10-meter windspeed.

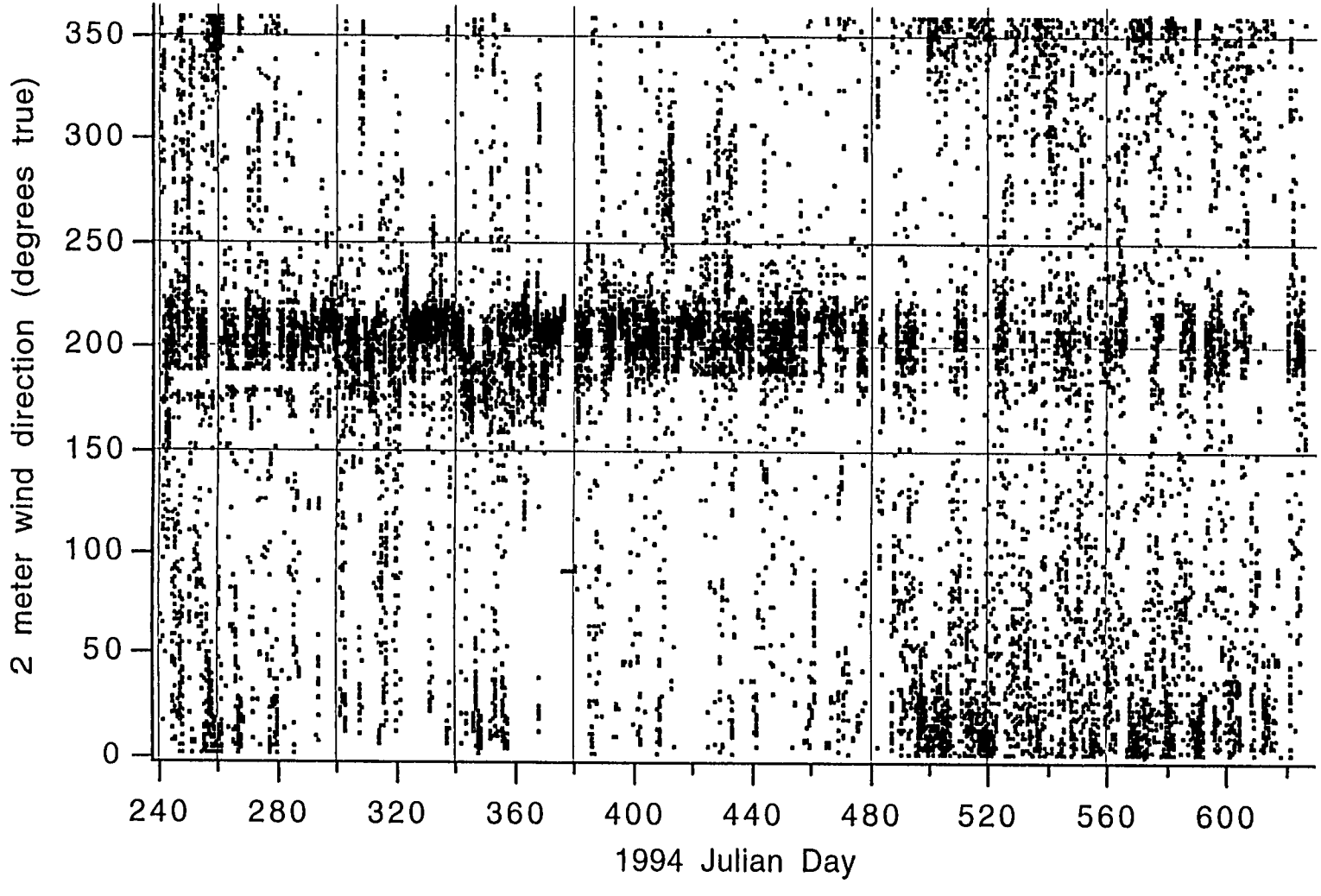

Figure A.12: 2-meter wind direction. North = 0, East = 90, etc. Note the north-south bimodal distribution.

BIBLIOGRAPHY

BIBLIOGRAPHY

[1] *U.S. Standard Atmosphere Supplements*, 1966.

[2] *Arctic System Science: Ocean-Atmosphere-Ice Interactions*, March 1990. workshop at UCLA.

[3] *MFSC World Wide Web SSM/I information.* available at URL http://wwwdaac.msfc.nasa.gov/userservices/datasetcatalog.html, 1998.

[4] R. Armstrong and M. Brodzik, "An Earth-gridded SSM/I data set for cryospheric studies and global change monitoring," *Advances in Space Research*, vol. 16, no. 10, pp. 155–163, April 1995.

[5] G. Backus and F. Gilbert, "Uniqueness in the inversion of inaccurate gross Earth data," *Phil. Trans. Roy. Soc. London*, vol. A 226, pp. 123–129, 1970.

[6] R. G. Barry, "The cryosphere and climate change," Technical Report DoE/ER-0235, U. S. Department of Energy, 1985.

[7] G. Bonan, "A Land Surface Model (LSM version 1.0) for ecological, hydrological, and atmospheric studies: Technical description and users guide," NCAR Technical Note TN-417+STR, National Center for Atmospheric Research, January 1996.

[8] M. Brodzik, 1997. personal communication.

[9] M. Brodzik, "The NSIDC EASE-Grid map projection parameters and grid definitions," Unpublished report, 1997.

[10] J. Brown and G. West, "Tundra biome research in Alaska," Tundra Biome Report 70-1, U.S. IBP, 1970.

[11] R. Bryson, "Preliminary estimates of the surface heat budget, summer, clear days at Point Barrrow," Technical report, Dept. of Meteorology, Univ. of Wisconsin, Madison, WI, 1956.

[12] R. D. Cess et al., "Interpretation of snow-climate feedback as produced by 17 general circulation models," *Science*, vol. 253, pp. 888–892, 1991.

[13] F. Chapin and G. Shaver, "Individualistic growth response of tundra plant species to environmental manipulations in the field," *Ecology*, vol. 66, no. 2, pp. 564–576, 1985.

[14] W. L. Chapman and J. E. Walsh, "Recent variations of sea ice and air temperature in high latitudes," *Bull. Am. Meteorol. Soc.*, vol. 74, pp. 33–47, 1993.

[15] P. Dahl, J. Judge, and J. Gallo, "Vertical distribution of biomass and moisture in a prairie grass canopy," Report RL-902, Univ. of Michigan Radiation Lab., November 1993.

[16] F. Dalton, W. Herkelrath, D. Rawlins, and J. Rhoades, "Time-domain reflectometry: simultaneous measurement of soil water content and electrical conductivity with a single probe," *Science*, vol. 224, pp. 989–990, 1984.

[17] J. Davies, G. Topp, and A. Annan, "Measuring soil water content in situ using time-domain reflectometry techniques," Report of Activities 77-1B, Geol. Surv. Can., 1977.

[18] M. C. Dobson, F. T. Ulaby, M. T. Hallikainen, and M. A. El-Rayes, "Microwave dielectric behavior of wet soil—Part II: Dielectric mixing models," *IEEE Trans. Geosci. Rem. Sens.*, vol. 23, pp. 35–46, January 1985.

[19] P. Dubois, J. van Zyl, and T. Engman, "Measuring soil moisture with imaging radars," *IEEE Trans. on Geosci. and Rem. Sens.*, pp. 915–926, July 1995.

[20] Emerson and Cuming. Eccosorb data sheets, 1986.

[21] A. W. England, J. F. Galantowicz, and B. W. Zuerndorfer, "A volume scattering explanation for the negative spectral gradient of frozen soil," in *Proc. of IGARSS91*, Espoo, Finland, June 1991.

[22] A. England and J. Galantowicz, "The Tower Mounted Radiometer System (TMRS)," in *Proc. of the ISTS Workshop on Ground Based Microwave Radiometry for Snow Cover and Soil Moisture*, North York, Ontario, June 1993, Univ. of Toronto Institute for Aerospace Studies.

[23] A. England and J. Galantowicz, "Moisture in a grass canopy from SSM/I radiobrightness," in *Proc. 2nd Topical Symposium on Combined Optical-Microwave Earth and Atmos. Sensing*, pp. 12–14, Atlanta, GA, April 1995.

[24] O. T. Farouki, "Thermal properties of soils," CRREL Monograph 81-1, U. S. Army Cold Regions Research and Engineering Lab., Hanover, NH, 1981.

[25] M. Fischman, "Investigation of the Tower Mounted Radiometer System and proposed improvements," Report RL-949, Univ. of Michigan Radiation Lab., March 1997.

[26] J. Galantowicz, *Microwave Radiometry of Snow-Covered Grasslands for the Estimation of Land-Atmosphere Energy and Moisture Fluxes*, PhD thesis, Univ. of Michigan, Ann Arbor, MI, 1995. Electrical Engineering and Atmospheric, Oceanic, and Space Sciences.

[27] J. Galantowicz and A. W. England, "Field data report for the first Radiobrightness Energy Balance Experiment (REBEX-1), October 1992–April 1993, Sioux Falls, South Dakota," Report RL-904, Univ. of Michigan Radiation Lab., December 1993.

[28] J. Galantowicz and A. England, "The Michigan Earth Grid: Description, registration method for SSM/I data and derivative map projections," Report 027396-2-T, Univ. of Michigan Radiation Lab., 1991.

[29] J. Hansen and S. Lebedeff, "Global trends of measured surface air temperature," *J. Geophys. Res.*, vol. 92, pp. 13,345–13,372, 1987.

[30] Y. Harazono, M. Yoshimoto, G. Vourlitis, et al., "Heat, water and greenhouse gas fluxes over the arctic tundra ecosystems at North Slope in Alaska," in *Proc. IGBP/BAHC-LUCC 4–7*, pp. 170–173, Kyoto, Japan, November 1996.

[31] A. Henderson-Sellers, "Land surface process models discussed in interdisciplinary forum," *EOS*, vol. 19, pp. 369, 379, September 1995.

[32] L. D. Hinzman and D. L. Kane, "Potential response of an arctic watershed during a period of global warming," *J. Geophys. Res.*, vol. 97, no. D3, pp. 2811–2820, 1992.

[33] L. D. Hinzman, D. Kane, C. Benson, and K. Everett, "Energy balance and hydrological processes in an arctic watershed," in *Ecological Studies*, J. Reynolds and J. Tenhunen, editors, volume 120, chapter 6, Springer-Verlag, Berlin, 1996.

[34] L. Hinzman, 1996. personal communication.

[35] L. Hinzman, D. Kane, R. Gieck, and K. Everett, "Hydrologic and thermal properties of the active layer in the Alaskan arctic," *Cold Regions Sci. and Tech.*, vol. 19, pp. 95–110, 1991.

[36] J. Hollinger, R. Lo, G. Poe, R. Savage, and J. Pierce, *Special Sensor Microwave/Imager User's Guide*, Naval Research Lab., Washington, DC, 1987.

[37] J. Hollinger et al., *DMSP Special Sensor Microwave/Imager Calibration/Validation Final Report*, Naval Research Lab., Wash.,D.C., 1989.

[38] J. Hollinger, J. Pierce, and G. Poe, "SSM/I instrument evaluation," *IEEE Trans. on Geosci. and Rem. Sens.*, vol. 28, no. 5, pp. 781–790, 1990.

[39] J. T. Houghton, B. A. Callander, and S. K. Varney, editors, *Climate Change 1992: The Supplementary Report to the IPCC Scientific Assessment*, Cambridge Univ. Press, Cambridge, 1992. (Intergovernmental Panel on Climate Change).

[40] J. T. Houghton, B. A. Callander, and S. K. Varney, editors, *Climate Change 1995—the science of climate change*, Cambridge Univ. Press, Cambridge, 1996. (Intergovernmental Panel on Climate Change).

[41] A. Hsu, 1998. personal communication.

[42] T. Jackson, D. LeVine, A. Griffis, D. Goodrich, T. Schmugge, C. Swift, and P. O'Neill, "Soil moisture and rainfall estimation over a semiarid environment with the ESTAR microwave radiometer," *IEEE Trans. on Geosci. and Rem. Sens.*, vol. 31, no. 4, , 1993.

[43] D. Kane, R. Gieck, and L. Hinzman, "Evapotranspiration from a small Alaskan arctic watershed," *Nordic Hydrology*, vol. 21, no. 4/5, pp. 253–272, 1990.

[44] T. Karl, J. Tarpley, R. Quayle, H.F.Diaz, D. Robinson, and R. Bradley, "The recent climate record: what it can and cannot tell us," *Rev. of Geophys.*, vol. 27, no. 3, pp. 405–430, August 1989.

[45] E. Kim and A. England, "Radiobrightness thermal inertia sensing of soil and canopy moistures for grassland areas," in *Proc. 2nd Topical Symposium on Combined Optical-Microwave Earth and Atmos. Sensing*, pp. 39–41, Atlanta, April 1995.

[46] E. Kim and A. England, "Field data report for Radiobrightness Energy Balance Experiment 0 (REBEX-0), 8/92–9/92, UM Matthaei Botanical Gardens," Report RL-916, Univ. of Michigan Radiation Lab., 1996.

[47] E. Kim and A. England, "Passive microwave freeze/thaw classification for wet tundra regions," in *Proc. Int'l Geosci. and Rem. Sens. Symp.*, Linclon, NE, May 1996.

[48] E. Kim and A. England, "Field data report for Radiobrightness Energy Balance Experiment 3 (REBEX-3), 9/94–9/95, Alaskan North Slope," Report RL-918, Univ. of Michigan Radiation Lab., 1998.

[49] E. Kim et al., "A custom EASE-Grid SSM/I processing system," in *Int'l Geoscience and Remote Sensing Symposium Proc.*, volume 2, Seattle, WA, July 1998.

[50] K. Knowles, *Points, pixels, grids, and cells—a mapping and gridding primer*, National Snow and Ice Data Center, Boulder, CO, 1993. Unpublished report.

[51] A. H. Lachenbruch and B. V. Marshall, "Changing climate: Geothermal evidence from permafrost in the Alaskan arctic," *Science*, vol. 234, pp. 689–696, 1986.

[52] Y.-A. Liou, *Land surface process/radiobrightness models for northern prairie*, PhD thesis, Univ. of Michigan, Ann Arbor, MI, 1996. Electrical Engineering and Atmospheric, Oceanic, and Space Sciences.

[53] Y.-A. Liou and A. W. England, "Annual temperature and radiobrightness signatures for bare soils," *IEEE Trans. Geosci. Remote Sensing*, vol. 34, pp. 981–990, July 1995.

[54] A. Lynch et al., "Development of a regional climate model of the western arctic," *J. Climate*, vol. 8, pp. 1555–1570, June 1995.

[55] A. Lynch, F. Chapin, III, L. Hinzman, W. Wu, E. Lilly, G. Vourlitis, and E. Kim, "Surface energy balance on the arctic tundra: Measurements and models," *in review J.Climate*, July 1998.

[56] S. Manabe, R. Stouffer, M. Spelman, and K. Bryan, "Transient responses of a coupled ocean-atmosphere model to gradual changes of atmospheric CO2: Part I: Annual mean response," *J. Climate*, vol. 4, pp. 785–818, 1991.

[57] J. Mather and C. Thornthwaite, "Microclimatic investigations at Point Barrrow, Alaska, 1956," *Climatology*, vol. 9, no. 1, pp. 51, 1956. Lab. of Climatology, Drexel Institute of Tech. Centerton, NJ.

[58] J. Mather and C. Thornthwaite, "Microclimatic investigations at Point Barrrow, Alaska, 1957–1958," *Climatology*, vol. 11, no. 1, pp. 239, 1958. Lab. of Climatology, Drexel Institute of Tech., Centerton, NJ.

[59] L. L. McCauley and M. Meier, editors, *Arctic System Science: Land/Atmosphere/Ice Interactions— A Plan for Action*, Fairbanks, AK, 1991. ARCUS (Arctic Research Consortium of the U.S.).

[60] J. McFadden, 1996. personal communication.

[61] G. Michaelson, C. Ping, and J. Kimble, "Carbon storage and distribution in tundra soils of arctic Alaska, USA," *Arctic and Alpine Res.*, vol. 28, pp. 414–424, 1996.

[62] D. Moss. *programs ssmitdrlatlon, ssmitdrta, ssmitdrtb.* distributed by NASA/MSFC DAAC.

[63] Y. Nakano and J. Brown, "Mathematical modeling and validation of the thermal regimes in tundra soils, Barrrow, Alaska," *Arctic and Alpine Res.*, vol. 4, no. 1, pp. 19–38, 1972.

[64] *DMSP Platform Document*, NASA/MSFC, 1995.

[65] *User's Guide to Special Sensor Microwave/Imager Data (NESDIS Level 1b Format)*, NASA/MSFC DAAC, 1993.

[66] *DMSP SSM/I Brightness Temperature Grids for the Polar Regions on CD-ROM—User's Guide*, National Snow and Ice Data Center, 1990.

[67] *NOAA/NASA Pathfinder Program EASE-Grid DMSP SSM/I Brightness Temperatures on CD-ROM*, National Snow and Ice Data Center, 1994–1998.

[68] J. Noilhan and S. Planton, "A simple parameterization of land surface processes for meteorological models," *Monthly Weather Rev.*, vol. 117, pp. 536–549, 1989.

[69] W. C. Oechel. presentation at the NSF Arctic System Science Program/Land Atmos. Ice Interactions Science Meeting, Seattle, WA, February 1996.

[70] W. C. Oechel, S. J. Hastings, G. Vourlitis, M. Jenkins, G. Riechers, and N. Grulke, "Recent change of arctic tundra ecosystems from a net carbon dioxide sink to a source," *Nature*, vol. 361, pp. 520–523, 1993.

[71] A. Ohmura, "A historical review of studies on the energy balance of arctic tundra," *J. Climatology*, vol. 2, pp. 185–195, 1982.

[72] C. O'Kray, "TDR to EASE-Grid conversion process documentation," Report RL-960, Univ. of Michigan Radiation Lab., 1998.

[73] T. Osterkamp. presentation at the ARCSS/LAII Science Meeting, Seattle, WA, February 1996.

[74] C. Ping. presentation at the ARCSS/LAII Science Meeting, Seattle, WA, February 1996.

[75] G. Poe, "Optimum interpolation of imaging microwave radiometer data," *IEEE Trans. on Geosci. Remote Sensing*, vol. 28, no. 5, pp. 800–810, 1990.

[76] *REBS Q*6.71 Net radiometer manual, Rev. 3*, Radiation Energy Balance Systems, 1995.

[77] R. Rovansek, L. Hinzman, and D. Kane, "Hydrology of a tundra wetland complex on the Alaskan arctic coastal plain, U.S.A.," *Arctic and Alpine Res.*, vol. 28, no. 3, pp. 311–317, 1996.

[78] E. Schanda, C. Matzler, and K. Kunzi, "Microwave remote sensing of snow cover," *Int. J. of Remote Sensing*, vol. 4, pp. 149–158, 1983.

[79] W. Schlesinger, *Biogeochemistry: an analyssis of global change*, Academic Press, 1991.

[80] T. J. Schmugge and J.-C. Andre, *Land surface evaporation—measurement and parameterization*, Springer-Verlag, 1991.

[81] P. J. Sellers, "Biophysical models of land surface processes," in *Climate System Modeling*, K. Trenberth, editor, pp. 451–490, Cambridge Univ. Press, Cambridge, 1992.

[82] A. Seth, *Land surface heterogeneity in 3-dimensional atmospheric simulations*, PhD thesis, Univ. of Michigan, Ann Arbor, MI, 1995. Dept. of Atmospheric, Oceanic, and Space Sciences.

[83] G. Shaver. *Integrated Ecosystem Research in Northern Alaska, 1947–1990*, 1991.

[84] J. Stein and D. Kane, "Monitoring the unfrozen water content of soil and snow using time-domain reflectometry," *Water Resources Research*, vol. 19, no. 6, pp. 1573–1584, 1983.

[85] A. Stogryn, "Estimates of brightness temperatures from scanning radiometer data," *IEEE Trans. Antennas and Propagation*, vol. 26, pp. 720–726, 1978.

[86] M. Sturm, April 1995. personal communication.

[87] G. Taylor and J. Luthin, "A model for coupled heat and moisture tranfer during soil freezing," *Can. Geotech. J.*, vol. 15, pp. 548–555, 1978.

[88] J. Tilley, January 1996. personal communication.

[89] G. Topp, J. Davis, and A. Annan, "Electromagnetic determination of soil water content: measurements in coaxial transmission lines," *Water Resources Research*, vol. 16, no. 3, pp. 574–582, 1980.

[90] K. Trenberth, editor, *Climate System Modeling*, chapter 5,14, Cambridge Univ. Press, Cambridge, 1992.

[91] F. T. Ulaby and M. El-Reyes, "Microwave dielectric spectrum of vegetation—Part II: dual-dispersion model," *IEEE Trans. on Geosci. Remote Sensing*, vol. 25, no. 5, pp. 550–557, 1987.

[92] F. Ulaby, R. Moore, and A. Fung, *Microwave remote sensing—active and passive*, Artech House, 1986. 3 vols.

[93] D. Verseghy, N. McFarlane, and M. Lazare, "CLASS—A Canadian Land Surface Scheme for GCMs. II. Vegetation Model and Coupled Runs," *Int. J. Climatology*, vol. 13, pp. 347–370, 1993.

[94] J. Walsh. presentation at NSF Arctic System Science Program/Land Atmos. Ice Interactions Science Meeting, Seattle, WA, February 1996.

[95] S. Warren, C. Hahn, J. London, R. Chervin, and R. Jenne, "Global distribution of total cloud cover and cloud type amounts over land," NCAR Technical Note TN-273+STR, National Center for Atmospheric Research, October 1986.

[96] A. L. Washburn and G. Weller, "Arctic research in the national interest," *Science*, vol. 233, pp. 633–639, 1986.

[97] G. Weller and C. Benson, "The structure and function of the tundra ecosystem," Progress Report 6, U.S. Tundra Biome Program, Tundra Biome Center, College, Alaska, 1971.

[98] G. Weller, S. Cubley, S. Parker, D. Trabant, , and C. Benson, "The tundra microclimate during snow melt at Barrrow, Alaska," *Arctic*, vol. 25, pp. 291, 1972.

[99] G. Weller and B. Holmgren, "The microclimates of the artic tundra," *J. Appl. Meteor.*, vol. 13, pp. 854–862, 1974.

[100] G. Wendler, "The heat balance at the snow surface during the melting period (March, April 1966) near Fairbanks, Alaska," *Gerlands Beiträge zur Geophysik*, vol. 76, pp. 453, 1967.

[101] F. J. Wentz, "User's manual SSM/I antenna temperature tapes (revision 1)," RSS Technical Report 120191, Remote Sensing Systems, Santa Rosa, CA, December 1991.

[102] P. J. Williams and M. W. Smith, *The Frozen Earth: Fundamentals of Geocryology*, Cambridge University Press, Cambridge, 1989.

[103] C. Willmott, S. Robeson, and J. Feddema, "Influence of spatially variable instrument networks on climatic averages," *Geophys. Res. Let.*, vol. 18, no. 12, pp. 2249–2251, December 1991.

[104] M. Yoshimoto, Y. Harazono, A. Miyata, and W. Oechel, "Micrometeorology and heat budget over the arctic tundra at Barrrow, Alaska in the summer of 1993," *J. Agric. Meteorol.*, vol. 52, pp. 11–20, 1996.

[105] B. Zuerndorfer, A. W. England, and G. H. Wakefield, "The radiobrightness of freezing terrain," in *Proc. of IGARSS89*, Vancouver, Canada, July 1989.

[106] B. W. Zuerndorfer, A. W. England, C. M. Dobson, and F. T. Ulaby, "Mapping freeze/thaw boundaries with SMMR data," *J. Agriculture and Forest Meteorology*, vol. 52, pp. 199–225, 1990.

IMAGE EVALUATION
TEST TARGET (QA-3)

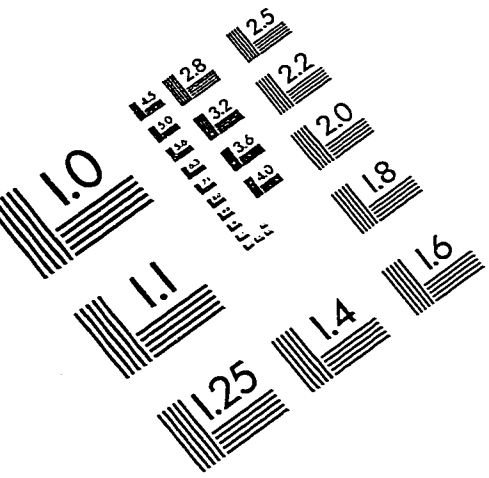

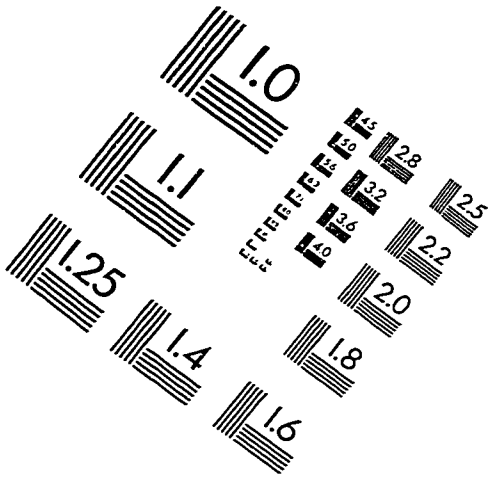

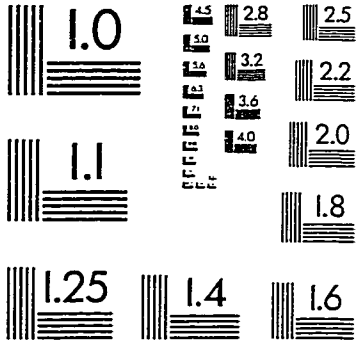

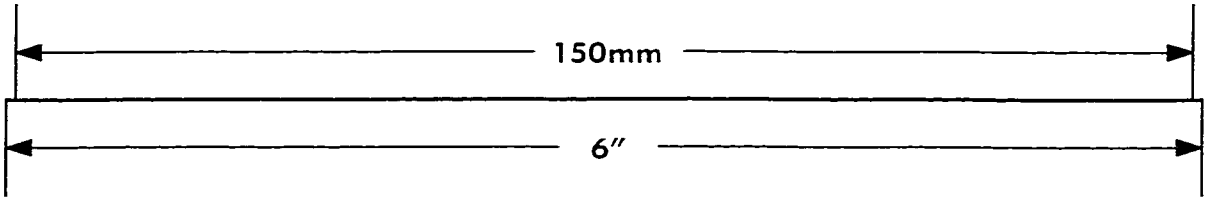

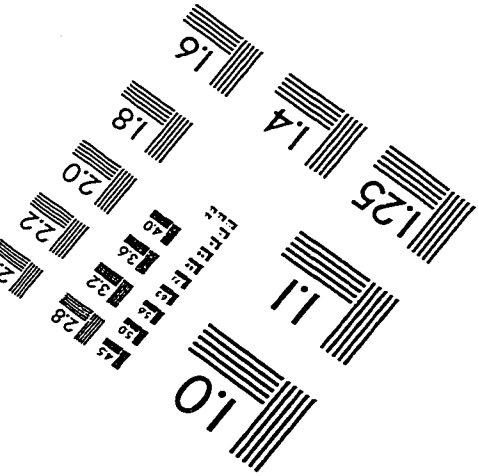

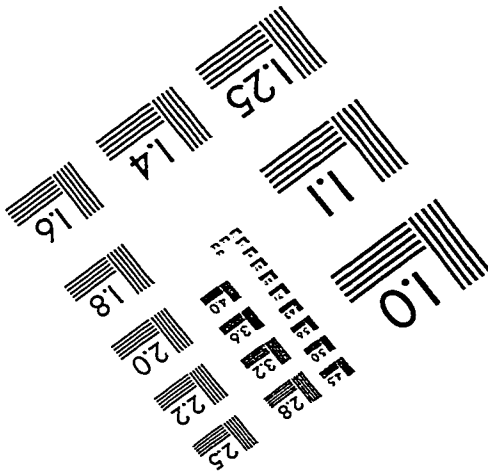

APPLIED IMAGE, Inc
1653 East Main Street
Rochester, NY 14609 USA
Phone: 716/482-0300
Fax: 716/288-5989